

DRAFT: OCTOBER 21, 2016 AT 3:49 PM

The Pennsylvania State University

The Graduate School

College of Earth and Mineral Sciences

MECHANISMS OF SLOW AND FAST EARTHQUAKES

A Thesis in

Geosciences

by

John R. Leeman

© 2017 John R. Leeman

Submitted in Partial Fulfillment
of the Requirements
for the Degree of

Doctor of Philosophy

April 2017

The dissertation of John R. Leeman was reviewed and approved* by the following:

Chris Marone
Professor of Geosciences
Thesis Adviser
Chair of Committee

Demian Saffer
Thesis Adviser
Professor of Geosciences

Sridhar Anandakrishnan
Professor of Geosciences

Richard Alley
Professor of Geosciences

Derek Elsworth
Professor of Energy and Mineral Engineering

*Signatures on file in the Graduate School.

Abstract

Here is where the text of the Abstract goes.

Table of Contents

List of Tables	ix
List of Figures	x
Acknowledgments	xxiv
Introduction	1
Chapter 1. Stiffness evolution of granular layers and the origin of repetitive, slow, stick-slip frictional sliding	2
1.1 Abstract	2
1.2 Introduction	3
1.3 Methods	6
1.3.1 Experimental Configuration	6
1.3.2 Data Analysis	8
1.4 Algorithm Description	9
1.5 Results	11
1.6 Discussion	13
1.7 Conclusions	16
Chapter 2. Laboratory observations of slow earthquakes and the spectrum of tec- tonic fault slip modes	32
2.1 Abstract	32

2.2	Introduction	33
2.3	Results	35
2.3.1	Mechanical Behavior	35
2.3.2	Stick-Slip Events	36
2.4	Discussion	37
2.5	Methods	40
2.5.1	Experimental Apparatus	40
2.5.2	Testing Procedure	41
Chapter 3. Characterization of Laboratory Slow Earthquakes		51
3.1	Abstract	51
Chapter 4. Mechanical and hydrologic properties of Whillans ice stream till: Im- plications for basal strength and stick-slip failure		52
4.1	Abstract	52
4.2	Introduction	53
4.2.1	Geologic Setting	56
4.3	Materials and Methods	57
4.3.1	Sample Preparation	57
4.3.2	Tri-axial Loading	58
4.3.3	Permeability and Compressibility	59
4.3.4	Acoustic Velocity	60
4.4	Results	61
4.4.1	Consolidation and Compressibility	62

4.4.2	Permeability	63
4.4.3	Acoustic Velocity	64
4.4.4	Hydrologic Model	64
4.5	Discussion	67
4.5.1	Till physical properties and relevance to sticky spot development	67
4.5.2	Shearing Processes	69
4.5.3	Effective Stiffness Feedback Mechanism	70
4.6	Conclusions	71
4.7	Effective Medium Model Formulation	73

Chapter 5.	On the origin and evolution of electrical signals during frictional stick	
	slip in sheared granular material	86
5.1	Abstract	86
5.2	Introduction	87
5.3	Previous Work	88
5.3.1	Natural Occurrences	88
5.3.2	Previous Experimental Work	89
5.4	Methods	92
5.4.1	Apparatus	93
5.4.2	Sample Material & Preparation	94
5.4.3	Potential Measurement	95
5.4.4	Experimental Procedure	96
5.4.5	Calibration and Control Tests	97

5.4.6	Data Analysis	98
5.5	Results	99
5.5.1	Mechanical Data	99
5.5.2	Electrical Data	101
5.6	Discussion	102
5.6.1	Electro-Mechanical Model	104
5.7	Conclusions	106
5.8	ESVM Calibration	108
Appendix A.	List of Biaxial Experiments	120
Appendix B.	List of Triaxial Experiments	133
Appendix C.	Sample Preparation Procedures	135
Appendix D.	Load Cell Theoretical Response	137
D.1	Introduction	137
D.2	Load Cell Design	137
D.2.1	Material properties	138
D.2.2	Mechanical design	138
D.2.3	Electrical design	139
D.3	Predicted response	141
Appendix E.	Load Cell Calibration Procedure	143
E.1	Introduction	143
E.2	Calibration procedure	143

E.3 Typical measured response	147
Appendix F. DCDT Calibration Procedure	
F.1 Introduction	148
F.2 Calibration procedure	149
F.3 Typical measured response	150
Appendix G. Look File Format Description and Biaxtools	
G.1 Purpose	152
G.2 Description	152
G.2.1 ASCII Files	152
G.2.2 Binary Files	153
G.3 Cautions	154
G.4 Usage	154
G.4.1 Return Formats	154
G.4.2 ASCII Files	154
G.4.3 Binary Files	155
G.5 Acknowledgements	155
G.6 Code	156
Bibliography	166

List of Tables

1.1	Two state variable parameters obtained from friction data inversion with all steel forcing blocks (p4113).	30
1.2	Load up stiffnesses during run-in for different forcing block configurations. Note that the steel/acrylic combination is much closer to the stiffness of all steel blocks than that of all acrylic blocks.	31
4.1	Physical parameters used to construct the effective medium model of compressional and shear wave velocities. Values are based on Dvorkin [1999] and Wang [2001].	73
5.1	List of Experiments	119
5.2	Composition of glass beads.	119

List of Figures

1.1	Experimental data showing examples of tests used to measure rate-and-state frictional parameters. (A) velocity step test in which loading velocity is changed from $150 \mu\text{m/s}$ to $500 \mu\text{m/s}$. Note transient evolution of friction followed by attainment of a new steady-state. (B) results for four slide-hold-slide tests in which shearing velocity is set to zero for a period (the hold) before re-shearing, showing holds of 30, 100, 300, and 1000 seconds. Frictional healing (μ) increases with the logarithm of hold time.	18
1.2	The biaxial press with supporting and forcing blocks in place. Double-direct shear samples consist of three blocks: two side blocks and a center block. Gouge layers are between the forcing blocks and confined with side-shields and a rubber membrane. (After Leeman et al. [2014])	19
1.3	A scanning electron micrograph of undeformed baking flour. Grain sizes are observed to vary in the $10\text{-}200 \mu\text{m}$ range. The material has a platy appearance reminiscent of clay and other phyllosilicate minerals.	20
1.4	Slow-slip and stick-slip events can be characterized by their slip duration, recurrence time, stress drop, and elastic loading stiffness. These quantities can be used to quantify the effective system stiffness and frictional properties including the rate of restrengthening (healing).	21

1.5 Data for three experiments with different forcing blocks and effective system stiffnesses. The acrylic only and steel-acrylic experiments exhibited slow stick-slip behavior, while steel forcing blocks produced only stable sliding.	22
1.6 (A) Friction data during slide-hold-slide tests over an entire experiment with steel forcing blocks. Note initial load-up: there is a region of peak strength followed by weakening and the attainment of steady-state strength after shear of ~ 10 mm. This test included three sets of holds lasting from 3 to 1000 seconds. (B) Friction parameter $\Delta\mu$ vs. the log of hold time for the slide-hold-slide tests shown in panel A. Healing exhibits log-linear behavior, independent of net shear displacement.	23
1.7 (A) Friction data for experiment p4113 with steel loading blocks, and (B) healing determined from slide-hold-slide tests. The sample exhibited limited stick-slip/slow-slip behavior, but only at a load point velocity of 5 $\mu m/s$. Frictional instability appears as a wide band of noise at the scale shown, around 10 and 40 mm load point displacement. Holds ranged from 3 to 1000 seconds and velocity steps from 5 to 1500 $\mu m/s$	24
1.8 Velocity steps in an all steel forcing block configuration can only be fit by a two state variable model. A) 15 - 50 $\mu m/s$ B) 50 - 150 $\mu m/s$ C) 150 - 500 $\mu m/s$	25

1.9 (A) Stiffness and (B) Stress drop and slip duration for events in experiments with all acrylic forcing blocks. Stiffness increases on the rise to steady state by a factor of nearly two and remains remarkably constant. Stress drops rapidly increase by a factor of two over the first twenty events before reaching a steady state. Slip duration begins at nearly twenty-five seconds, then rapidly decreases to around five seconds.	26
1.10 (A) Stiffness and (B) Stress drop and slip duration for events in the steel/acrylic forcing block system. Stiffness follows a similar trend to the all-acrylic experiment, but exhibits a smaller increase with strain. Stress drop increases rapidly, but then returns and maintains its initial level until a second family of events occurs around events 80-120. Slip duration begins faster than for the all-acrylic blocks and stays lower with more scatter.	27
1.11 Two groups of stick-slip events are evident after sufficient shearing in the steel/acrylic system. At the expected shear failure point there are several small failures, but the layer recovers and continues to load to a higher stress before failure.	28
1.12 Response of the system with various effective stiffnesses. The stability boundary is crossed between the steel and steel/acrylic system. Stiffnesses shown are the initial load up stiffnesses of the sample. All data are from the same displacement range, but have been offset in shear stress for clarity.	29

2.4 Stiffness during an experiment. Friction data for one complete experiment (run p4316) with shear load-unload cycles. Slow slip events emerge spontaneously at a displacement of 8.5 mm. (Inset) Stiffness measured from unload-reload cycles in the range =0.3-0.4 (large grey circles) and from the slope of the elastic loading segments of individual stick-slip events (small black circles). Both measurements indicate an initial increase in stiffness, caused by shear enhanced compaction. In this experiment we explored multiple shearing rates during slow slip (e.g., for events in the range 27-29 mm and 31-33 mm), which had a clear effect on stick-slip amplitude and stiffness.	46
2.5 Rate and State Parameters. Data and modeling procedure for obtaining rate-and-state friction parameters and their variation with shear displacement. A) Data from experiment p4309 (grey data points) and model (solid line) for a velocity step test from 10 to 1 m s ⁻¹ , with illustration of the friction direct effect a, evolution effect b, and critical slip distance D _c . B) Evolution of (b-a) with shear displacement (see also Figure 3A). Note the transition from rate strengthening to rate weakening at 8 mm displacement, after which a steady-state behavior is reached. C) The critical slip distance decreases with shear displacement as frictional steady-state is reached. D) Evolution of the critical stiffness (k _c) with slip.	47

4.1 Samples for this study were obtained from borehole 89-1-4 near the junction of the B1 and B2 branches of Whillans Ice Stream. Ice velocities of 600 m/yr are typical in the region [Rignot et al., 2011; Mouginot et al., 2014]. The grounding line is marked in solid black.	74
4.2 A) The completed sample assembly ready to be loaded into the pressure vessel. B) Schematic diagram of the tri-axial loading cell. Heat shrink tubing was used as a thin, low-strength jacketing material. A hydraulic syringe pump provided isotropic confining and axial loading stresses. A linearly variable displacement transformer (LVDT) measured sample stain. Two high-precision water syringe pumps imposed a hydraulic head to determine sample permeability. Piezoelectric transducers in the loading platens measured the elastic wave travel time through the core (inset).	75
4.3 To determine permeability, flow rates from the upstream (blue) and downstream (green) pumps are fit with a least squares fit (red) when the steady-state flow condition is achieved (shaded area). The procedure is repeated at multiple hydraulic heads for repeated permeability measurement.	76
4.4 An example acoustic waveform collected during the step-loading test. Inset shows changes in travel time with step loading to 1 MPa effective stress. First arrivals are picked with a cross-correlation technique for consistency.	77

4.7	(A) Predicted compressional and shear wave velocities from the effective medium model as a function of effective stress, (B) an expanded view showing field velocity measurements from seismic experiments, and porosity (C). The model is supported by experimental compressional wave velocity measurements, but no shear wave measurements could be obtained in the laboratory due to the very low effective pressures of the experiment. Black circles represent direct measurements from the laboratory, gray bars are velocity estimates by Luthra et al. [2016] and black triangles are estimates by Blankenship et al. [1987].	80
4.8	A) Flow chart showing the sequence used when computing the 1-D hydrologic model. B) A cartoon version of the system with ice unloading the till beneath it on a tidal timescale. Upward drainage as a result of lower effective stress at the ice-till interface will quickly result in the formation of a hard layer that slows further drainage and limits the hard layer depth to tens of centimeters. C) Loading from the ice will inject water back into the till as the basal hydraulic pressure is increased. . .	81
4.9	Model results for a coupled diffusion/compaction model of the till layer with an imposed 50 kPa effective stress perturbation at the top boundary. The perturbation can affect the till over several tens of centimeters in a 12 hour tidal time scale. Over a longer perturbation, such as moving over a rough area on the bed, the till can come close to equilibrium in a month.	82

4.10 XRD analysis shows very high clay content in the till samples with significant amounts of quartz as well. Some non-uniqueness exists in the type of clays present, but an effort was made to minimize the misfit with reasonable geological constraints.	83
4.11 A) Evolution of volumetric strain during repeated tidal load cycling. B) Strain was accumulated during all cycle sets, similar to the axial strain trends, but with some slight anomalies likely induced by thermal effects on pump volume measurements as volume changes are very small.	84
4.12 Experimental data and fits used in loading portions of the simple hydrologic model. Porosity-permeability (A) was fit with an exponential, while effective stress - porosity (B) and effective stress - compressibility (C) were fit with logarithmic relationships.	85
5.1 Experimental setup. A) The biaxial hydraulic press: sample assemblies are supported by steel blocks in the sample area. B) Double direct shear geometry consists of two layers of gouge confined between three forcing blocks. Side shields and a plastic membrane are used to contain gouge material as the sample is sheared. C) Placement of the electrostatic voltmeter (yellow cylinder) in the side and top view positions. A window was cut into the side shield for the side view geometry.	109
5.2 Scanning electron microscope micrographs of the starting glass beads for all experiments. A) 100-150 μm B) 420-500 μm	110

5.3 Experiments performed on glass beads (100-150 μ m diameter) under ambient humidity, 100% humidity, and submerged conditions exhibit similar mechanical behavior. Increased stress drops are observed with increased humidity and in the submerged case. Inset: Anatomy of a stick-slip event. The recurrence time is the time between peaks in shear stress. Initially the shear stress increases linear-elsastically. Deviation from line-elastic behavior marks the onset of elasto-plastic deformation and pre-seismic slip. When the ultimate strength of the layer is reached shear stress drops rapidly and the cycle begins again.	111
5.4 A) Samples exhibit a log-log linear relation between recurrence time and velocity. Faster loading rates result in shorter recurrence times. B) Friction drop increases with the recurrence time as there is more time for the layer to heal before the next stick-slip event.	112
5.5 During shearing two trends are observed: 1) A long-term charging/discharging trend in the electrical potential and 2) Potential change related to individual stick-slip events. The entire system initially charges, approximately until mechanical steady-state is reached. During this phase co-seismic potential changes are dominantly positive (top left inset). After attainment of mechanical steady-state, the system begins to maintain or discharge potential. During this phase the co-seismic potential changes are dominantly negative (top right inset).	113

5.6 Stick-slip events and associated ESVM measurements for three-different load point velocities of 1, 30, and 100 $\mu\text{m}/\text{s}$. A) At slow loading velocities the electrical signal clearly mirrors the stress curve in most cases B) For intermediate velocities, the relation is still present. C) At high velocities, the electrical signal is a sharp pulse an order of magnitude higher than those observed at low velocities, and we observe small inter-seismic charging.	114
5.7 Each order of magnitude driving velocity change produces a $\sim 5\times$ increase in the electrical signal observed. All experiments shown are with the side-view sensor geometry.	114
5.8 A schematic representation of the stages of electrical behavior during an experiment: A) During the initial run-in there is massive grain rearrangement as force chain networks begin to form. This sliding motion tribo-electrically charges the system. B) After the force chain network forms there is minimal grain-boundary sliding. Shear loads are supported in the granular layer by highly stressed force chains (dark colors). Electron holes migrate away from highly stressed beads into the matrix creating an electrical potential gradient. C) When the layer fails and all grains are at roughly the same low stress, a return current redistributes the electrical gradient and the cycle begins again.	115

5.9 Calibration of the ESVM from a function generator source (bottom panel). A series of steps through the ESVM ‘response’ setting from 1-9 shows that the input square wave applied to the aluminium surface under test is well-recorded on each setting (top panel). The upward trend in ESVM data is a product of a DC offset that occurs each time the response setting is changed on the instrument.	116
5.10 A detailed comparison of a single waveform shows that at lower response settings (lighter colors) the waveform is smoothed slightly, with the nearly instantaneous voltage change distributed over up to 0.1 seconds on both the rise and fall. At higher resolutions (darker colors) the sharp transition is clearly seen, but at the price of a higher noise level during the flat hold states.	117
5.11 At all response settings the beginning of ESVM signal change corresponds well in the time domain with the leading and falling edge of the input signal. Smoothing due to longer integration times is observed at low response settings.	118
D.1 Mechanical drawings of the two styles of load cells used in the lab. Dimensions are in mm. Oblique view not to scale.	139
D.2 Electrical schematic of the 8-gauge load cell design. Orientation 1 and 2 are marked for identification convenience.	140
D.3 Physical construction of the load cell and arrangement of strain gauges. gauge sets are set apart by 90°. Electrical points marked * are connected. 140	

E.1 A proper setup of the load cell, steel puck, proving ring stack. Notice the careful alignment of all members.	145
E.2 An example of a proving ring dial under no load that needs adjustment. Simply loosen the dial face set-screw to move the gauge legend.	146
E.3 An example calibration obtained from the 44mm solid load cell.	147
F.1 An example calibration obtained from a DCDT.	151

Acknowledgments

I am forever indebted to my parents, Russell and Dianne Leeman for encouraging my curiosity and instilling in me an set of hard-work ethics. Both were essential to helping me get to where I am now. Thank you to my wife, Lendi, for helping me through the struggles and for being more supportive and understanding that I ever knew was possible. Finally, I would like to thank those on my committee and my colleagues in the department. Without your guidance, help, and advice this work would have been impossible.

Somewhere, something incredible is waiting to be known.

—Carl Sagan

Out of the cradle onto the dry land here it is standing . . .

atoms with consciousness . . . matter with curiosity.

Stands at the sea . . . wonders at wondering . . . I . . . a
universe of atoms . . . an atom in the universe.

—Richard P. Feynman

Introduction

sdfsdfs

Chapter 1

Stiffness evolution of granular layers and the origin of repetitive, slow, stick-slip frictional sliding

1.1 Abstract

We demonstrate the frictional behaviors of steady state sliding, stick-slip, and repetitive, slow stick-slip sliding through a carefully-designed suite of laboratory experiments focused on exploring the role of loading system stiffness in controlling the frictional response to shear. We performed tests on sheared layers of baking flour, with three configurations of loading blocks made of steel and cast acrylic to achieve different stiffnesses. Slide-hold-slide and velocity step tests were conducted and analyzed in a rate-and-state friction framework. With compliant loading blocks, the material exhibits unstable stick-slip behavior with slow-slip events of duration up to twenty seconds. Slow-slip has been difficult to achieve in the lab and has only been observed for a narrow variety of boundary conditions and materials. Our results suggest that this behavior is strongly controlled by the stiffness of the system, the strain history of the sample, and shear fabric evolution. We describe a new suite of automated tools that greatly improve friction analysis and provide insight to the underlying mechanisms of slow stick-slip. We demonstrate that layer stiffness evolves with shear strain and modifies the mechanical behavior of stick-slip sliding. Our work suggests that slow earthquakes in tectonic fault zones may be linked to

shear fabric development and associated changes in local stiffness, likely in combination with variations in frictional constitutive properties and effective stress.

1.2 Introduction

Although stick-slip is generally considered an analog for earthquakes Brace and Byerlee [1969]; Johnson et al. [2013] in the framework of stable or unstable sliding, it has recently become evident that there is a spectrum of fault slip behaviors Peng and Gomberg [2010]. The discovery of slow earthquakes and non-volcanic tremor Ikari et al. [2013]; Beroza and Ide [2011]; Obara [2002]; Ide et al. [2007] has raised questions about the link between fault zone frictional properties, in situ conditions, and the underlying mechanisms of slow-slip Kaproth and Marone [2013].

The rate and state frictional model provides a convenient framework in which to examine the frictional response of materials and characterize their second order frictional characteristics that are thought to control the stability of sliding Brace and Byerlee [1966, 1969]; Gu et al. [1984]; Marone [1998]. The rate and state equation (eq.1.1) describes friction (μ) in terms of a direct effect (a), an evolution effect (b), a state variable (θ), and the velocity of both the slider (V) and load point or reference velocity (V_0). The evolution of the state variable can be described by various relations Marone [1998]. Here, we consider the Dieterich (slowness) relation (eq.1.2) as it provides a scheme to interpret time dependent healing of materials, although we note that recent works favor the Ruina (slip) state evolution law Marone and Saffer [ress]; Bayart et al. [2006]. To describe more complex frictional behavior, a third term is often appended to equation 1.1 adding terms b_2 , D_{c2} , and θ_2 .

$$\mu = a \ln \left(\frac{V}{V_0} \right) + b \ln \left(\frac{V_0 \theta}{D_c} \right) + b_2 \ln \left(\frac{V_0 \theta_2}{D_{c2}} \right) \quad (1.1)$$

$$\frac{d\theta}{dt} = 1 - \frac{V\theta}{D_c} \quad (1.2)$$

Materials may slide in a stable manner or fail in a stick-slip fashion. The transition between stable sliding and stick-slip is generally viewed as a Hopf bifurcation that can be thought of as occurring at a critical stiffness (k_c), defined in Equation 1.3 for quasi-static motion Rice and Gu [1983]; Gu et al. [1984]. For values of stiffness greater than k_c , the system is stable. When k approaches and falls below k_c , the system undergoes damped oscillations and then enters an unstable regime that corresponds to stick-slip behavior. From Equation 1.3, it is clear that velocity strengthening materials ($a - b > 0$) should slide stably, because the critical stiffness becomes negative. They therefore: 1) are unlikely to nucleate large earthquakes; and 2) should arrest rupture that propagates into them. Velocity weakening materials ($a - b < 0$) may undergo stable sliding or stick-slip based on the stiffness of the system in relation to the effective normal stress and friction parameters, expressed by a critical stiffness. The idea of there being two modes of frictional failure (stable sliding and stick-slip) is a generalization of the spectrum of slip behaviors that occurs in the transition between the two Rice and Gu [1983].

$$k_c = \frac{b - a}{D_c} \quad (1.3)$$

For materials that exhibit stable sliding behavior, we can interrogate frictional parameters by imposing velocity steps or conducting slide-hold-slide tests (Fig.1.1). During velocity step tests, the load point velocity is instantaneously changed from one velocity to another and the frictional response of the material recorded. During slide-hold-slide tests, the sample is sheared until friction reaches steady-state (μ_{ss}), then shearing is stopped for a prescribed amount of time. After the hold time has elapsed, shearing begins again at a constant shearing rate and the frictional healing ($\Delta\mu$) is measured as the difference between the peak re-load friction (μ_{peak}) and the initial steady-state value Marone [1998]. Healing can be summarized by the term β , describing a line fit to hold-time (t_h) and frictional healing($\Delta\mu$) data on a natural log-linear axis (eq.1.4).

$$\beta = \frac{\Delta\mu}{\ln(t_h)} + c \quad (1.4)$$

The purpose of this paper is to describe work on a novel friction system designed to improve understanding of slow, stick-slip frictional failure. We measure the frictional behavior of sheared layers of baking flour and characterize slip events in terms of stress drop, slip duration, and the loading stiffness in order to explore the relationship between macroscopically observed slip behavior, stiffness, and frictional properties. We vary the stiffness of the loading system and observe changes in frictional failure behavior.

As in most shearing experiments, there are likely deformation and fracture processes occurring at the grain-scale, but these processes do not detract from the goal of showing failure mode behavior with stiffness changes. While flour is a very compliant material, certainly more compliant than the loading system, energy can be stored by

the loading system while the fault zone is ‘locked’ and elastic strain energy accumulated in the loading blocks and load frame. Any air trapped in the granular layer is inconsequential as the low viscosity air can quickly escape as evidenced by our initial layer consolidation. Any remaining air is sufficiently compressible to produce negligible pressurization effects.

1.3 Methods

1.3.1 Experimental Configuration

In our experiments, we sheared gouge layers in a double direct shear configuration using a biaxial deformation apparatus with a servo-hydraulic control system Karner and Marone [2000]; Frye and Marone [2002]. In this configuration, two granular layers are sheared between three roughened forcing blocks (Fig.1.7). All experiments were conducted with Gold Medal brand all-purpose flour, enriched, bleached, and pre-sifted. The baking flour is highly compressible and is poly-disperse with grains ranging from about 10-200 μm in diameter (length) with a platy appearance (Fig.1.3).

We measured force with strain gauge load cells placed in series with the loading rams and sample. Displacement was measured with direct current displacement transducers (DCDTs) between the ram nose and end platens of the hydraulic rams. Data were recorded using a 24-bit analog to digital converter. Data were collected at 10 kHz and averaged to the desired rate from 1 Hz to 10 kHz.

In order to achieve different loading system stiffnesses, three combinations of forcing blocks were used: 1) all acrylic blocks; 2) center acrylic with steel side blocks,

and 3) all steel blocks. The forcing blocks were cut to size and machined with grooves (1 mm deep x 2mm spacing on acrylic, 0.8 mm deep x 1 mm spacing on steel) perpendicular to the shearing direction to ensure that shear occurred within the layer and not at the layer boundary Anthony and Marone [2005]; Knuth and Marone [2007]. The nominal frictional contact area was 10 cm x 10 cm.

Layers were built by placing the side forcing blocks on a leveling jig and applying cellophane tape around the perimeter. Two layers of flour were confined in a three forcing block assembly with a rubber membrane at the bottom and side-shields on the boundaries to avoid lateral extrusion of the layer (Fig.1.7). The top of the sample was unconfined.

In all experiments, samples were placed into the loading frame and a normal stress (σ_n) of 1 MPa was applied and maintained constant in load-feedback servo-control. The layers were sheared by controlling the position of the vertical ram in displacement feedback servo-control, which was driven at a constant displacement rate. The force required to shear at this rate was measured and converted to the shear stress acting on each layer of the double-direct shear arrangement.

In all experiments, a ‘run-in’ period was necessary to reach a stable sliding friction (Fig.1.1). All tests were conducted at an initial load point velocity of 1 $\mu\text{m}/\text{s}$. In systems that exhibited unstable behavior, the run-in driving velocity was maintained for the duration of the test and the evolution of the slow-slip/stick-slip monitored. When stable sliding behavior was observed, a series of velocity steps and/or slide-hold-slide tests were performed to independently measure second-order frictional properties Marone [1998].

1.3.2 Data Analysis

For each individual stick-slip event, we report stress drop, slip duration, recurrence time, and loading stiffness (Fig.1.4). Note that for each event, a period of increasing shear load is observed initially followed by inelastic yielding and plastic strain accumulation during fully-mobilized frictional slip. The stress drop, duration, and recurrence time of each event provide information about frictional properties, including the rate of frictional healing. The linear-elastic portion of the stress-displacement curve (Fig.1.4) is a measure of the system stiffness including testing machine, forcing blocks and sheared layers. This shear stiffness is a key parameter because it is the stiffness that will drive frictional instability if the value falls below the critical friction stiffness k_c dictated by Equation 1.3.

With large numbers of slow-slip/stick-slip events it is necessary to automate the analysis procedure for both repeatability and efficiency. This is made difficult by electrical and mechanical noise as well as changes in recording rate during the course of the experiment. We address these challenges by developing an algorithm to pick the beginning and end of each slip event in a reliable and repeatable manner with as few user-defined free parameters as possible. After the picks are obtained, the mechanical quantities of interest must be extracted. Some values, such as changes in peak friction, are trivial to compute. However, loading stiffness is slightly more complicated, and requires determining where the load-displacement curve deviates from linearity. We address this problem by using a goodness-of-fit approach, detailed below.

1.4 Algorithm Description

We define stick-slip by a stress increase over some time interval and a sudden drop in stress, followed by another event. There are many techniques in the literature of ‘change point detection’ such as CUSUM Page [1954], Student’s T test techniques Buishand [1982], and wavelet methods Raimondo and Tajvidi [2004]. These techniques are generally used for step detection and are not the ideal candidates for repetitive events such as repeating frictional slip. Picking based on derivatives is a more robust technique, and therefore we employ a first-derivative based approach. When the stress is at a peak or trough, the first derivative (with time or shear displacement) is zero by definition. We examine the derivative of shear stress for a sign change or zero crossing as it is unlikely that we will exactly capture the data points for which the derivative is zero to machine precision.

Taking the derivative of noisy, digital lab data can be challenging. In general, for an analytic function or data with no noise, we would approach the problem by using a forward, central, or backward difference approximation. These simplistic techniques work for well-behaved functions with no noise, but for lab data, a running average slope works better. Our method involves a user-defined window size over which a least-squares approach is used. This resulting running average slope technique is robust for noisy data.

To determine loading stiffness of each stick-slip event, we began with the derivative of the stress-displacement curve (Fig.1.4). We then computed an array of signs for the complete data set. Sign change detection identifies the zero-crossings of the running average slope derivative. Pairs of zero crossings are evaluated for their associated stress

drop, with anything below a user defined threshold discarded. This step is necessary to further filter noise and smaller failures. Using the zero crossing generally captures the true maximum and minimum of the data, but occasionally, due to smoothing of noise, may not capture the exact maximum or minimum. After observing the algorithm on many datasets, we found that max/min errors were always small and within the noise; therefore we did not implement a local search around the zero crossing.

The objective when determining the linear-elastic stiffness of each stick-slip is to fit a line to the displacement versus shear stress data, but only to the portion before inelastic deformation and creep begins. In the past this has been done by eye and resulted in limited estimates of stiffness for each experiment as well as inconsistency between picks. To automate this process, we calculate the correlation coefficient of the data (eq.1.5) for many data windows. The algorithm begins with the minimum shear stress for an event with n data, determined by the derivative technique, and calculates the correlation of three data points (the trough and the two following points). Next, the correlation is calculated for additional data points, up to n_{\max} . We assume that the deviation from linearity begins after the correlation is maximized. After we define the linear domain, a line is fit to that data segment using a least squares method. This process is repeated for each stick-slip/slow-slip event.

$$r_{xy} = \frac{\sum_{i=1}^n x_i y_i - \sum_{i=1}^n x_i \sum_{i=1}^n y_i}{\sqrt{n \sum_{i=1}^n x_i^2 - \left(\sum_{i=1}^n x_i\right)^2} \sqrt{n \sum_{i=1}^n y_i^2 - \left(\sum_{i=1}^n y_i\right)^2}} \quad (1.5)$$

1.5 Results

We varied system stiffness by using a range of forcing blocks in the double direct shear assembly. Tests with all acrylic forcing blocks and with acrylic center/steel side block combinations produced slow slick-slip behavior, while tests with all steel blocks generally produced stable sliding behavior (Fig.1.5). For the experiments with steel forcing blocks, frictional sliding was stable. Thus, once friction reached a steady state, we imposed velocity step tests to measure rate/state friction parameters. We note that in one experiment, at $5 \mu\text{m}/\text{s}$, the steel block configuration exhibited slow-slip behavior, transitioning to stable sliding at higher velocities. During shear, extrusion and densification of the gouge material occurs Scott et al. [1994], sometimes introducing complicating strain effects.

Slide-hold-slide tests were used to measure frictional healing. Healing tests conducted with steel forcing blocks indicate healing rates (β) of 0.015-0.018. These rates are consistent with rates obtained on geological materials of several percent Dieterich [1978, 1972]; Marone [1998]; Karner et al. [1997]; Beeler et al. [1994]. We imposed three sets of slide-hold-slide tests at successively higher shear displacements and found no correlation of the healing rate with shear strain, in contrast to previous results Richardson and Marone [1999]. We note however that those studies used granular silicate minerals at higher applied stresses, and thus higher rates of granular comminution. Also, the maximum shear strain in our experiments were less than those in other studies (Fig.1.6). We conducted slide-hold-slide tests before and after velocity step tests to determine any

variation with shear strain. Even after shear displacement of nearly 5 cm, no significant change in healing rate was observed (Fig.1.7). All of our data exhibit a log-linear relationship between healing and hold time.

Velocity step tests were conducted with both up-steps and down-steps in the range: 5, 15, 50, 150, 500, 1500 $\mu\text{m}/\text{s}$ in the steel forcing block configuration. At 5 $\mu\text{m}/\text{s}$ the system was unstable, but then exhibited stable behavior at higher velocities. Model fits of selected velocity steps are shown in Figure 1.8. These data show velocity weakening frictional behavior with ($a - b$) values of ~ 0.01 and friction evolution shows a clear two state variable behavior. Best fit parameters are summarized in Table 1.1.

In most friction studies, the system stiffness is taken from a linear portion of the loading curve prior to the sample yielding and attainment of fully mobilized, steady-state frictional sliding. Moreover, this stiffness is generally thought of as the stiffness of the system for the entire experiment. The values in table 1.2 represent the load up stiffness determined via this traditional approach. Load up stiffness values are obtained by fitting a line to the load up curves during experimental run-in. Values for all-steel and steel/acrylic are relatively similar, but the all-acrylic forcing system is about one-third less stiff than the steel system.

We applied our automated picking algorithm for experiments with unstable behavior in acrylic and acrylic/steel blocks. The steel system displayed dominantly stable sliding and could not be interrogated for stiffness with this method. The experiment with all acrylic forcing blocks showed a stress drop pattern that increased to a relatively steady value of 0.014MPa (Fig.1.9). Slip durations began at ~ 20 seconds, then decreased to ~ 5 seconds. Shear loading stiffness increased with shear strain from ~ 0.001 MPa/ μm

to $\sim 0.002 \text{ MPa}/\mu\text{m}$ with shear strain until frictional steady state behavior was reached, and then remained stable for the duration of the experiment. Experiments with the steel/acrylic combination (Fig.1.10) show similar stiffness evolution, but the slip durations are much more scattered compared to the all acrylic configuration. These data show the same initial increase in the stress drop, but then decrease to almost their initial states. Finally, there is a second ‘family’ of slip events that appear around event 80 with much larger stress drops (Fig.1.11). These events exhibit the same minimum shear stress, but reach a higher stress before failure. There is also a notable partial failure observed at the nominal shear strength.

1.6 Discussion

Our data show that stiffness evolves systematically as a function of shear strain and that stick-slip friction events reflect this evolution. Load point velocity also plays an important role in the transition from stable to unstable sliding.

It has long been known that loading stiffness plays an important role in frictional sliding Jaeger [1971]; Brace and Byerlee [1966], and since its introduction in the 1980’s, rate and state friction theory has provided an approach to quantifying the interplay between elastic stiffness and friction constitutive behavior (eq.1.3) Rice [1983]. Previous works show that the critical friction distance (D_c) decreases with shear strain Marone and Kilgore [1993]. However, the evolution of fault zone stiffness with shear strain has not been similarly explored. Our results show that stiffness increases by nearly a factor of two during initial shearing, up to shear strains of ~ 3 . These changes are likely a function of densification, shear localization, and fabric development as elongated particles align

and shear begins to attain its steady state behavior. The fact that characteristics of stick-slip events, such as stress drop and slip duration, evolve over this same range, suggests that both changes in frictional properties and elastic stiffness are important in controlling the mode of slip on faults.

Rate and state friction predicts increased event durations and decreased stress drops with increased effective stiffness, as the system transitions to stable behavior Baumberger and Berthoud [1999]. Our data comparing the different stiffnesses from the three forcing block configurations used seems to verify this prediction (Fig.1.12). However, during each experiment, we observe an increase in stiffness with shear strain that coincides with increased stress drop and reduced slip event duration (Figs.1.9,1.10). This suggests a more complex interplay between the evolution of fabric development, frictional constitutive properties, and system stiffness with shear strain that produces changes in material behavior. Coupling of the stored elastic energy is also believed to influence strain accumulation and release. Because the entire center forcing block acts as a spring (i.e. stores elastic strain), a simple 1-D spring-slider model is overly simplified in the context of our experiments. Accounting for the 2-D geometry and heterogeneity of the elastic loading system that includes both forcing blocks and the gouge layer itself is more realistic. This more complicated elastic coupling would influence the nature of strain accumulation, and the rate at which it is released during failure. The stiffness of the portions of the system where elastic strain energy is stored is most important, as the unloading stiffness of those materials will dictate the rate at which energy can be released to the system during dynamic failure and therefore dictate the failure mode. While the gouge is itself storing some strain energy, we believe that most energy is being

stored in the forcing blocks while the fault zone is locked, hence why the block stiffness exhibits such a strong control on failure mode.

Our data suggest that as strain localizes within the sheared layer, the stiffness of the gouge layer increases, resulting in an overall stiffer elastic system. Strain is localized onto shear surfaces oblique to the layer, such as R1 (cross cutting shear surfaces inclined approximately 30° to the shear direction), B (boundary parallel shears near the forcing block surface), and y (shear parallel surfaces completely contained within the layer) planes Logan et al. [1992]; Marone [1998]. The transition of slip behavior from steady-state sliding to stick-slip (Fig.1.12) is apparent and follows results obtained by Baumberger and Berthoud [1999]. By using compliant blocks that have the capability to store energy where the gouge is interacting with the surface roughness (i.e. rather than steel forcing blocks with a spring in series to modulate stiffness Kaproth and Marone [2013]), we believe that our approach is most analogous to natural fault zones, in which the gouge is coupled to adjacent wall rocks that store strain energy between slip events.

Another curious aspect of these experiments is the unstable behavior observed in steel blocks, but only at low velocity in p4113 (the least stiff of the steel experiments). Even in acrylic blocks, the system would only stick slip at velocities below $100 \mu\text{m/s}$. This is consistent with previous observations of the transition from stick-slip to stable sliding Heslot et al. [1994]. In our experiments, it is possible that healing cannot occur fast enough to support repeated stick-slip behavior at higher velocities. Flour maintains its strong velocity weakening behavior at velocities up to $1500 \mu\text{m/s}$, suggesting that stiffness and/or velocity dependent rate and state parameters are necessary to explain the velocity dependent behavior.

Stiffness relations used in arguments about stick-slip and slow-slip events often cite critical rupture patch sizes by assuming an inverse relationship between effective stiffness and nucleation patch size Ikari et al. [2011]. While this argument is valid and physically required, it is likely equally important to consider that effective stiffness evolves during the transition from distributed to localized shear Marone and Saffer [ress]. This combination of factors modifying stiffness likely leads to a more complex fault zone evolution than previously believed. Local variations in stiffness could modulate shear behavior and velocity during rupture propagation or even aid in stopping fast rupture. One possible indication of the local variability of stiffness is the two families of stick-slip events observed in the steel/acrylic case. This behavior is reminiscent of period-doubling in chaotic systems near a critical point. These smaller events could represent local heterogeneities which are too small to rupture the entire layer. It is also very likely that the 1-D stiffness coupling is inadequate to fully describe the system.

1.7 Conclusions

We show that repetitive, slow, stick-slip frictional sliding can occur in a sheared layer and that the transition from stable to unstable sliding can be affected by a change in system loading stiffness. While it is not a surprising revelation that stiffness is a factor in frictional slip behavior, the evolution of stiffness with strain that we observe points to a more complicated story. We suggest that stiffness evolves as shear fabric is developed in the layer with increasing shear displacement. This indicates that fault slip style, which is partly dictated by stiffness, may not depend solely on the inverse relation of loading system stiffness to sample dimension. In our system, it is possible

that stiffness of the gouge evolves enough to cause a transition from stable sliding to slow-slip/stick-slip behavior. If our results apply to tectonic faults, they suggest that with progressively increasing net strain/offset, areas experiencing slow-slip events may evolve to an unstable slip condition with potential to host traditional seismic events. Our results were obtained for wheat flour, and it remains to be seen whether similar behavior occurs in geologic materials. We have found similar behavior in preliminary work on finely ground quartz. Further investigation is warranted to determine the range of conditions for which slow slip may occur and whether such behavior is possible for other types of elastic coupling. Work is also underway to measure strain energy stored in the system before, during, and after failure to attempt to quantify some of the possible explanations proposed in this work.

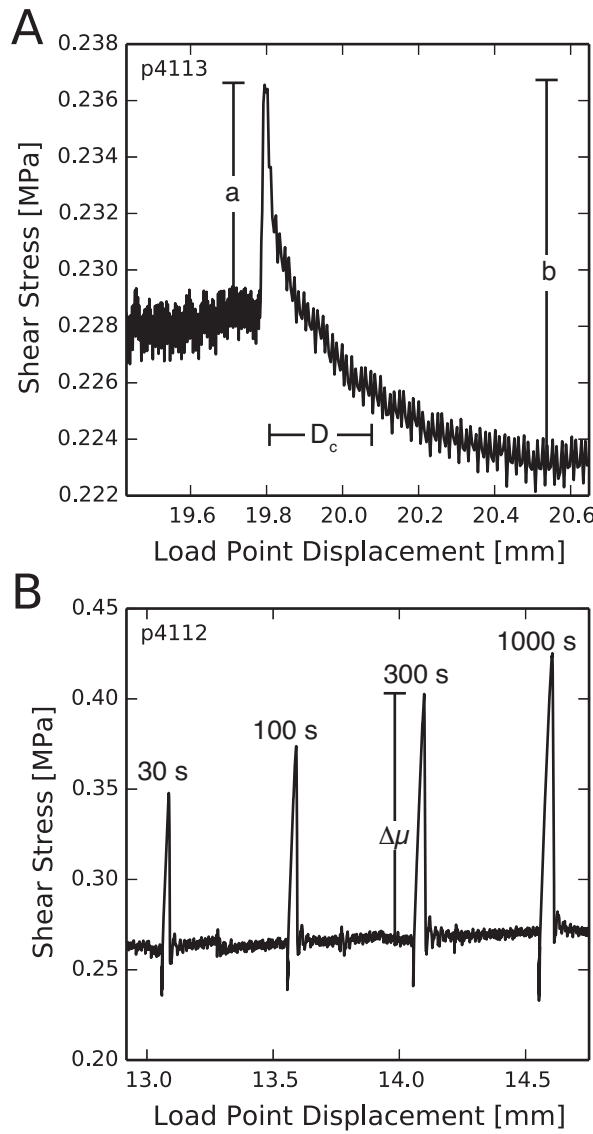


Fig. 1.1. Experimental data showing examples of tests used to measure rate-and-state frictional parameters. (A) velocity step test in which loading velocity is changed from 150 $\mu\text{m}/\text{s}$ to 500 $\mu\text{m}/\text{s}$. Note transient evolution of friction followed by attainment of a new steady-state. (B) results for four slide-hold-slide tests in which shearing velocity is set to zero for a period (the hold) before re-shearing, showing holds of 30, 100, 300, and 1000 seconds. Frictional healing (μ) increases with the logarithm of hold time.

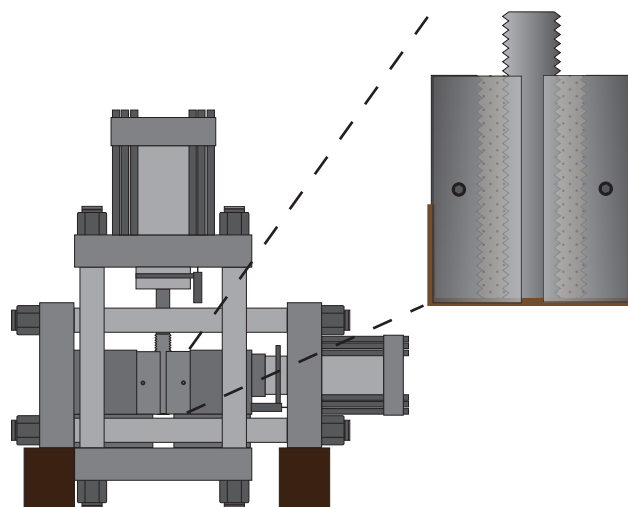


Fig. 1.2. The biaxial press with supporting and forcing blocks in place. Double-direct shear samples consist of three blocks: two side blocks and a center block. Gouge layers are between the forcing blocks and confined with side-shields and a rubber membrane. (After Leeman et al. [2014])

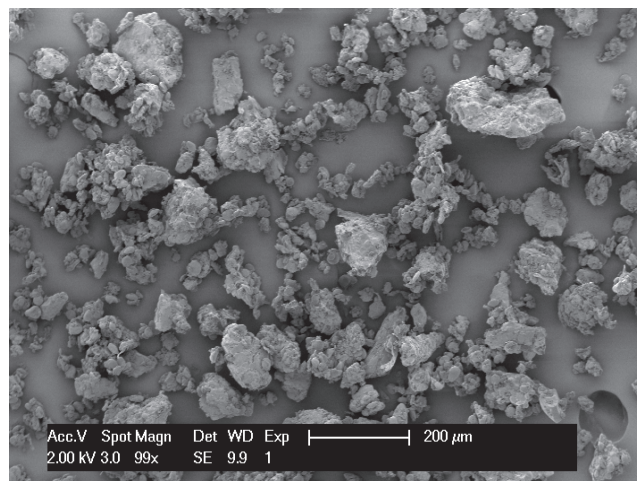


Fig. 1.3. A scanning electron micrograph of undeformed baking flour. Grain sizes are observed to vary in the $10\text{-}200 \mu\text{m}$ range. The material has a platy appearance reminiscent of clay and other phyllosilicate minerals.

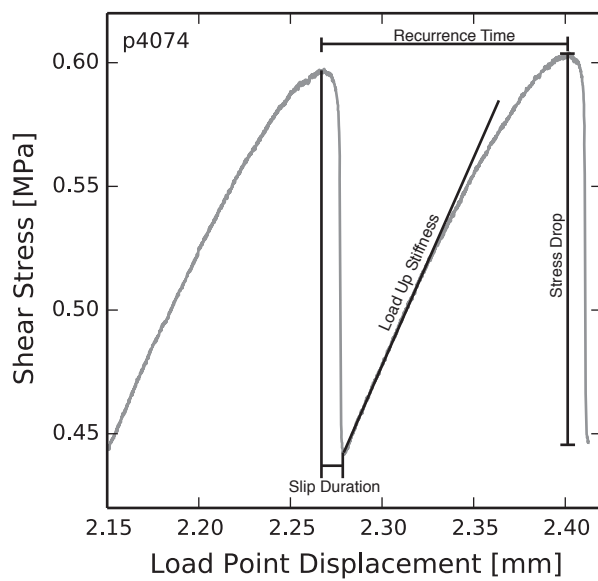


Fig. 1.4. Slow-slip and stick-slip events can be characterized by their slip duration, recurrence time, stress drop, and elastic loading stiffness. These quantities can be used to quantify the effective system stiffness and frictional properties including the rate of restrengthening (healing).

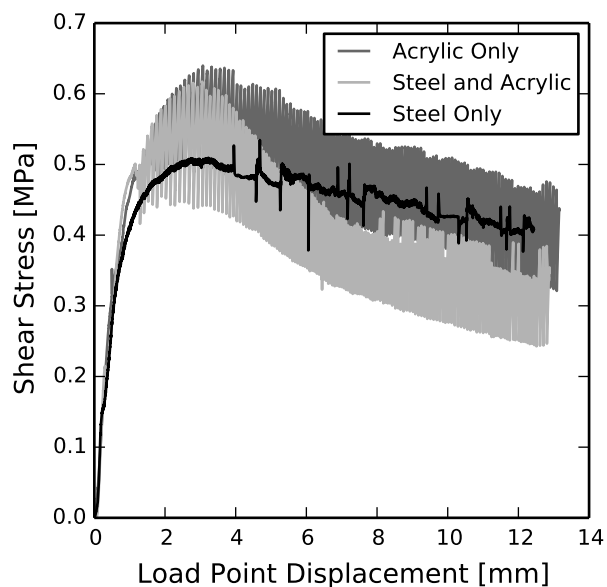


Fig. 1.5. Data for three experiments with different forcing blocks and effective system stiffnesses. The acrylic only and steel-acrylic experiments exhibited slow stick-slip behavior, while steel forcing blocks produced only stable sliding.

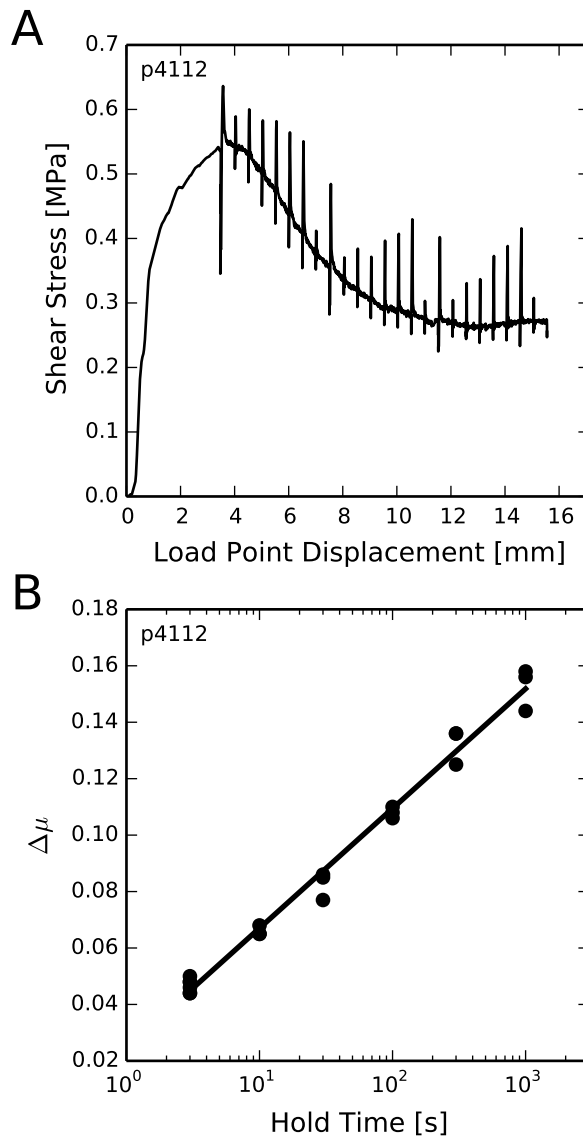


Fig. 1.6. (A) Friction data during slide-hold-slide tests over an entire experiment with steel forcing blocks. Note initial load-up: there is a region of peak strength followed by weakening and the attainment of steady-state strength after shear of ~ 10 mm. This test included three sets of holds lasting from 3 to 1000 seconds. (B) Friction parameter $\Delta\mu$ vs. the log of hold time for the slide-hold-slide tests shown in panel A. Healing exhibits log-linear behavior, independent of net shear displacement.

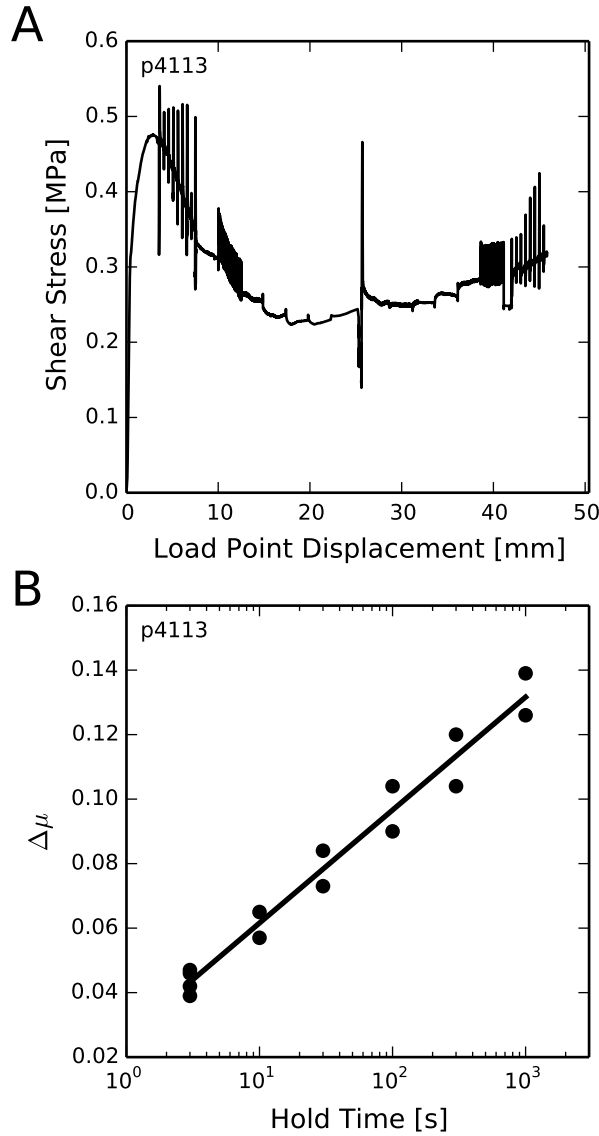


Fig. 1.7. (A) Friction data for experiment p4113 with steel loading blocks, and (B) healing determined from slide-hold-slide tests. The sample exhibited limited stick-slip/slow-slip behavior, but only at a load point velocity of $5 \mu\text{m}/\text{s}$. Frictional instability appears as a wide band of noise at the scale shown, around 10 and 40 mm load point displacement. Holds ranged from 3 to 1000 seconds and velocity steps from 5 to $1500 \mu\text{m}/\text{s}$.

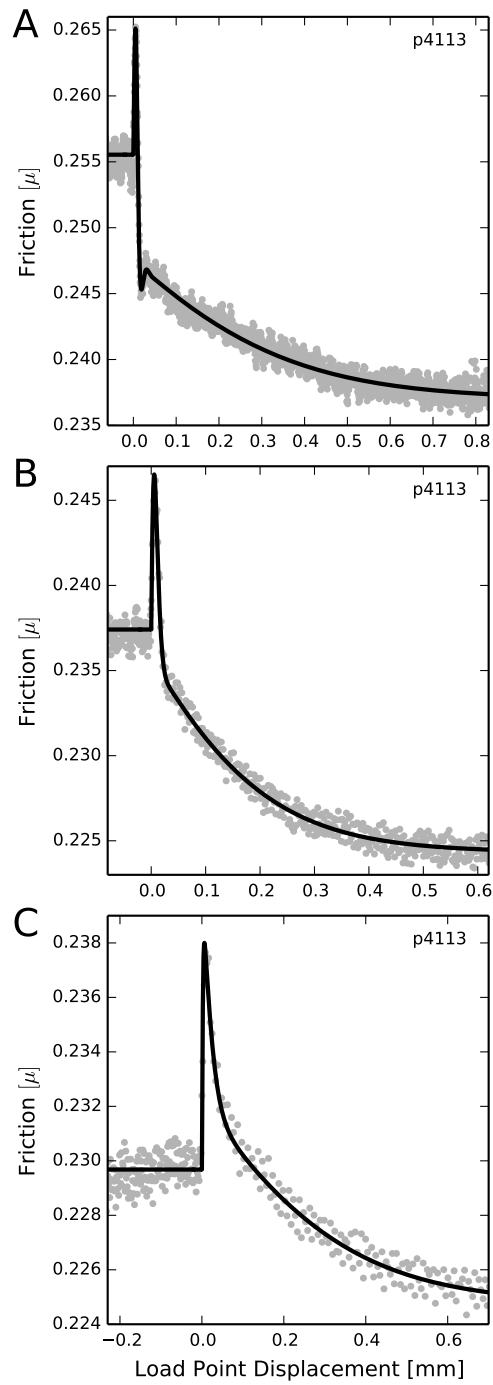


Fig. 1.8. Velocity steps in an all steel forcing block configuration can only be fit by a two state variable model. A) 15 - 50 $\mu\text{m}/\text{s}$ B) 50 - 150 $\mu\text{m}/\text{s}$ C) 150 - 500 $\mu\text{m}/\text{s}$

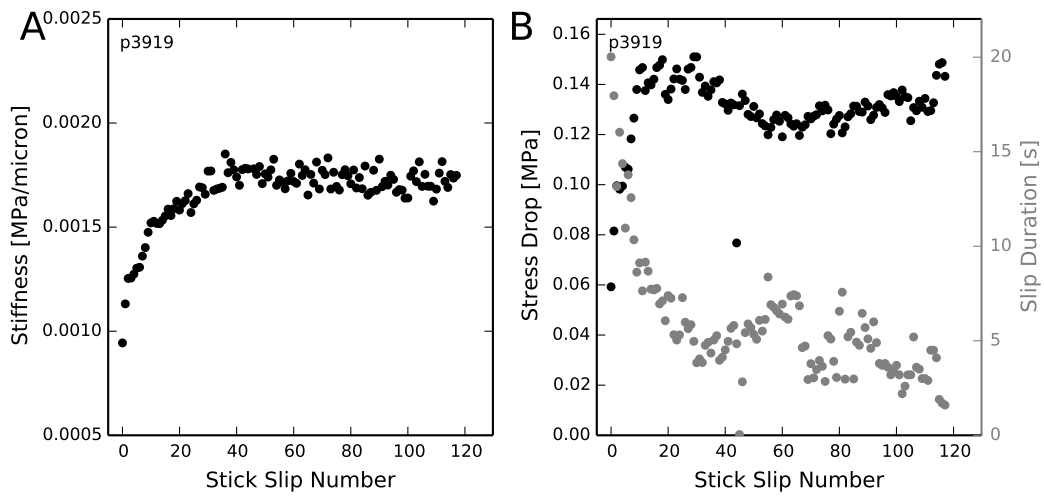


Fig. 1.9. (A) Stiffness and (B) Stress drop and slip duration for events in experiments with all acrylic forcing blocks. Stiffness increases on the rise to steady state by a factor of nearly two and remains remarkably constant. Stress drops rapidly increase by a factor of two over the first twenty events before reaching a steady state. Slip duration begins at nearly twenty-five seconds, then rapidly decreases to around five seconds.

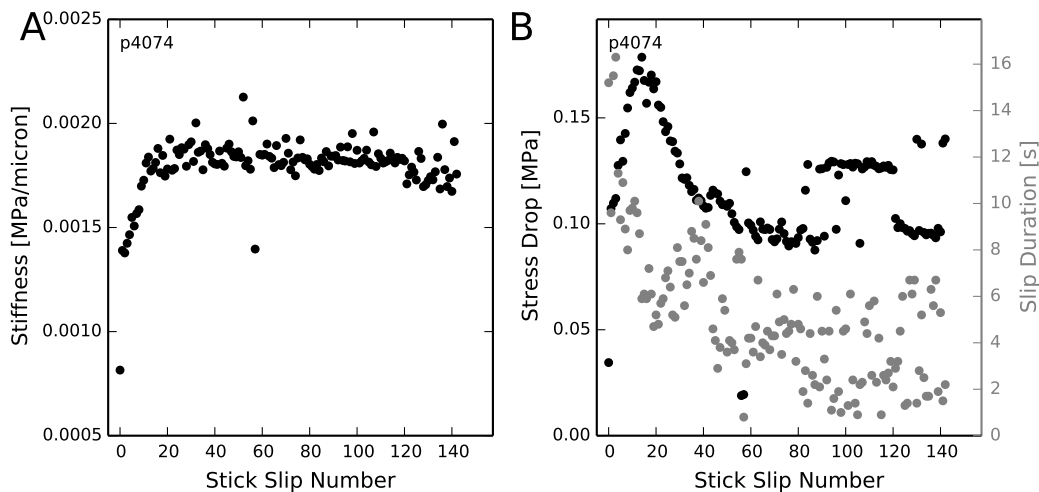


Fig. 1.10. (A) Stiffness and (B) Stress drop and slip duration for events in the steel/acrylic forcing block system. Stiffness follows a similar trend to the all-acrylic experiment, but exhibits a smaller increase with strain. Stress drop increases rapidly, but then returns and maintains its initial level until a second family of events occurs around events 80-120. Slip duration begins faster than for the all-acrylic blocks and stays lower with more scatter.

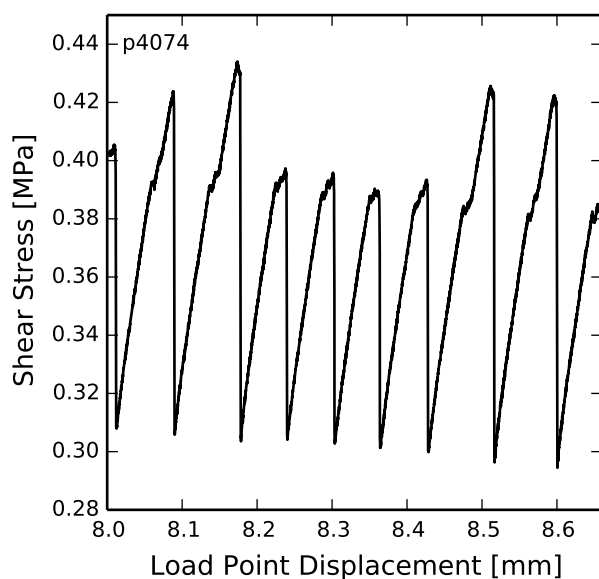


Fig. 1.11. Two groups of stick-slip events are evident after sufficient shearing in the steel/acrylic system. At the expected shear failure point there are several small failures, but the layer recovers and continues to load to a higher stress before failure.

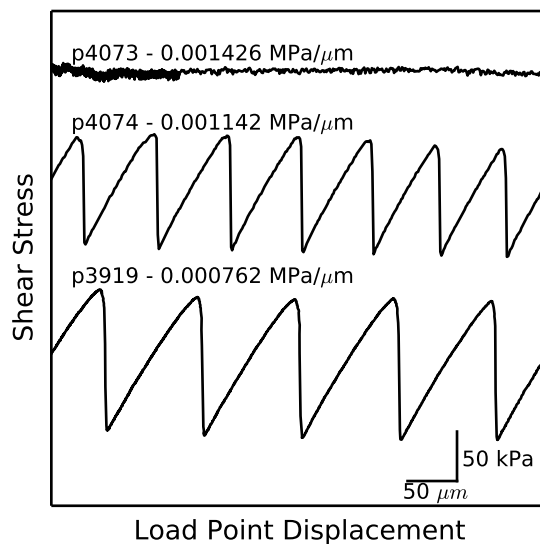


Fig. 1.12. Response of the system with various effective stiffnesses. The stability boundary is crossed between the steel and steel/acrylic system. Stiffnesses shown are the initial load up stiffnesses of the sample. All data are from the same displacement range, but have been offset in shear stress for clarity.

V_0	V	a	b_1	D_{c_1}	b_2	D_{c_2}	$a - b$
15	50	0.0120	0.0185	5.351	0.0088	207.912	-0.0154
50	150	0.0110	0.0125	7.448	0.0105	127.545	-0.0119
150	500	0.0077	0.0056	15.432	0.0061	199.407	-0.0041

Table 1.1. Two state variable parameters obtained from friction data inversion with all steel forcing blocks (p4113).

Experiment	Blocks	Layer Thickness (mm)	Temperature (C)	Relative Humidity (%)	Loading Stiffness (MPa/ μ m)
p3916	Acrylic	7	23.5	22	0.000630
p3918	Acrylic	7	23.1	22	0.000917
p3919	Acrylic	7	24.2	23.9	0.000762
p3920	Acrylic	7	24.4	25	0.000871
p3917	Steel/Acrylic	7	22	21.9	0.001002
p4074	Steel/Acrylic	8	23.1	38.8	0.001142
p4073	Steel	8	23.4	28.4	0.001426
p4112	Steel	8	24.3	55.5	0.001184
p4113	Steel	8	24.3	56.1	0.001070

Table 1.2. Load up stiffnesses during run-in for different forcing block configurations. Note that the steel/acrylic combination is much closer to the stiffness of all steel blocks than that of all acrylic blocks.

DRAFT: OCTOBER 21, 2016 AT 3:49 PM

Chapter 2

Laboratory observations of slow earthquakes and the spectrum of tectonic fault slip modes

2.1 Abstract

Slow earthquakes represent an important conundrum in earthquake physics. Whereas regular earthquakes are catastrophic events with rupture velocities governed by elastic wave speed, the processes that underlie slow fault slip phenomena, including recent discoveries of tremor, slow slip, and low frequency earthquakes, are less understood. Theoretical models and sparse laboratory observations have provided insights, but the physics of slow fault rupture remain enigmatic. Here we report on laboratory observations that illuminate the mechanics of slow slip phenomena. We show that a spectrum of slow slip behaviors arise near the threshold between stable and unstable failure, and is governed by frictional dynamics via the interplay of fault frictional properties, effective normal stress, and the elastic stiffness of the surrounding material. This generalizable frictional mechanism may act in concert with other hypothesized processes that damp dynamic ruptures, and is consistent with the broad range of geologic environments where slow earthquakes are observed.

2.2 Introduction

Slow earthquakes are a mode of self-sustained fault rupture in which slip accelerates but does not reach rates sufficient to radiate high-frequency seismic energy^{1,2}. Seismic and geodetic observations reveal that slow slip and the related phenomena of low-frequency earthquakes and non-volcanic tremor define a spectrum of slip behaviors that unfold over timescales ranging from seconds to months²⁻⁶. Slow earthquakes can be large, in some cases equivalent to M7+ earthquakes, and they may play a role in stress transfer and thus triggering of damaging regular earthquakes⁷. Slow earthquakes have also been observed as precursors to regular earthquakes and thus they may provide insight into the processes of earthquake nucleation^{8,9}. Although geophysical observations have resolved fine details of slow earthquake slip and propagation rates of tectonic fault tremor^{6,8-10}, the fundamental and controlling mechanics of these phenomena remain enigmatic. Regular earthquakes have long been understood in terms of stick-slip failure dictated by frictional and elastic properties of Earth's crust¹¹. Laboratory studies have provided key insights into the physics of fault failure and its dynamics, both for repeating earthquake-like stick-slip failure and for more complex slip behaviors. For example, previous works have reported a range of observations including transient slip, oscillatory sliding behavior, and dynamic rupture at sub-Raleigh and supershear propagation speeds¹²⁻¹⁸. Transient and oscillatory behavior have been interpreted as analogs for premonitory slip prior to earthquakes or transient aseismic slip^{12,18,19}. Despite their relevance to natural fault zones and slow earthquakes, detailed laboratory observations of repetitive slow slip transients are few and do not include systematic studies. These

behaviors have been reported in some experimental work^{12,14,15}, but have been interpreted and modeled in the context of specific fault rheologies, using so-called ?designer? friction laws. In one form of these laws, slow stick-slip is produced by an increase in frictional resistance with slip velocity, such that instability is quenched during acceleration^{14,15,19}. Other explanations for slow earthquakes have focused on processes that may arrest slip acceleration during earthquake nucleation, including dilatancy hardening^{20,21}, transitional frictional behavior as a function of slip²² or slip rate, and fault zone heterogeneity. Some numerical simulations successfully predict complex slip behavior, including oscillatory behavior and the emergence of periodic slow slip^{20,23}. Two dimensional numerical models also show promise in reproducing natural events, with fewer free parameters than multiple state variable models²⁶. To date, the origin of slow earthquakes has been explored largely via seismic or geodetic data or through numerical experiments with only sparse, isolated laboratory observations to probe the underlying mechanics. Although theoretical models can explain the emergence of slow-slip transients under certain conditions or for specific frictional rheologies^{20,21,23}, a fundamental mechanical explanation for these events remains elusive. Yet, slow modes of fault rupture are observed in a variety of tectonic and geologic settings, and with a wide range of durations, raising the question as to whether they arise from a universal mechanism^{6,24}. Although many fault zones are rich in phyllosilicate minerals, which have been shown to exhibit both rate-weakening and rate-strengthening behavior under conditions comparable to those expected *in situ* in the seismogenic crust²⁵⁻²⁷, we focus on quartz gouge to investigate the systematics of frictional failure, because it is a well-studied material that is common in natural faults, and is thought to play a key role in controlling their slip

behavior^{27,28}. Quartz gouge also exhibits frictional properties that enable us to probe the stability boundary using geophysically-relevant values of normal stress and sliding rates. This allows a detailed investigation of the frictional dynamics of slow slip, which provides a robust and generalized framework to apply to tectonic fault zones. Here we describe laboratory experiments that reproduce the full spectrum of fault slip behaviors under geophysically relevant conditions of normal stress and fault composition, and which illuminate their underlying physics. Our experiments are designed to explore the full range of slip stability, as described by the stability parameter $\gamma = k/k_c$, from $\gamma < 1$ (inherently stable slip) to dynamic stick-slip ($\gamma > 1$). Consistent with previous works^{14,18,23} near the stability boundary, $\gamma \approx 1$, we observe complex slip patterns that precede slow slip. We document a systematic and robust relationship between departure from the stability threshold, slip velocity, and duration of repetitive failure events. Our experimental results, to the best of our knowledge, are the first complete and systematic study to investigate the full spectrum of slip behaviors from slow to fast events, as observed for tectonic faults.

2.3 Results

2.3.1 Mechanical Behavior

In our experiments, gouge layers initially exhibited stable sliding, followed by the emergence of repeating slow stick-slip events (Figure 1, 2A). The slow slip events arose gradually, over an interval of up to 1.5 mm, and then increased in amplitude over as few as 10-20 slip events before reaching a mechanical steady-state, characterized by

relatively uniform recurrence intervals and friction drops, up to the maximum imposed displacements of ≈ 50 mm. For our layers, which were 3-mm thick prior to shear, this corresponds to shear strains of 30-50. Each slow-slip event began with a gradual acceleration and culminated in a slip event and stress drop (Figure 1).

2.3.2 Stick-Slip Events

Our experimental results are consistent with theory, numerical experimentation,^{20,23} and with existing lab data for stick-slip¹¹. We document a spectrum of stick-slip behaviors in experiments conducted over a range of normal stresses (Figure 2A). At low normal stress (6 MPa) and close to the stability transition described by Equation (1), slip events have systematically longer duration and smaller stress drops than their higher normal stress counterparts (Figure 2C). Details of the friction records for slow events show that slip begins gradually, well before the peak strength is reached, and then accelerates during the stress drop (Figure 2B). The maximum slip velocities for slow-slip events are in the range of 50-100 m s⁻¹, and slip speed increases systematically with increasing normal stresses, which leads to increasingly unstable behavior (Equation 1). For the lowest values of normal stress that produced repeating transient slip events, we measured peak slip velocities of only a few 10's of m s⁻¹, on the order of the driving velocity. For a normal stress of 14 MPa, we observed audible fast stick-slip events with slip velocities $\gtrsim 2$ mm s⁻¹.

2.4 Discussion

The short duration, audible high slip velocity events are manifestations of dynamic instability and represent laboratory analogs of regular, fast earthquakes¹¹. Likewise, we posit that the observed spectrum of slow to fast stick-slip events in our experiments are representative of the spectrum of slip behaviors observed on tectonic faults, including repeating slow slip events and low frequency earthquakes^{4,6}. Near the stability transition, we also document complex and chaotic behaviors including period doubling and transient variations in stick-slip amplitude with long period modulation (Figure 2A), consistent with theoretical predictions²³. To investigate the mechanics of slow stick-slip events, we carefully measured both the elastic loading stiffness k and the critical stiffness k_c in each of our experiments. We measured k directly from the loading curves of stick-slip events and from unload/reload cycles (Supplementary Figure 1). Stiffness increases with shear displacement up to 15 mm, and then reaches an approximately constant value (Figure 3; Supplementary Figure 1). The increase in stiffness with shearing is consistent with shear-enhanced compaction and granular comminution during the first few mm of slip²⁹. As noted above, we measure k_c directly from the parameters in Equation 1 using velocity step experiments (Figure 3A, Supplementary Figure 2), and also empirically using the value of k ? at the observed transition between unstable and stable slip (black line, Figure 3B). The empirically defined threshold stiffness increases with displacement and reaches a steady value of ? 7x10⁻⁴ m⁻¹ at a displacement of 16 mm, equivalent to a shear strain of 5-6 (Figure 3B). Direct measurements of k_c yield similar values (6-7x10⁻⁴ m⁻¹; Supplementary Figure 2), and also show that k_c increases dramatically

within the first 10 mm of shear displacement. This is due to the combined effects of increasingly velocity weakening friction (Figure 3A) and decreasing critical slip distance D_c with shear strain (Supplementary Figure 2). The evolution of (b-a) is consistent with inferred shear localization and with the observation that unstable slip emerges after a finite shear strain (Figure 1). The shear displacement needed for the emergence of slow-slip decreases with increasing η_n (Figure 2A), consistent with enhancement of shear localization and fabric development at higher η_n . Taken together, our direct (Figure 3A, Supplementary Figure 2) and independent (Figure 3B) measurements of k_c and k (Supplementary Figures 1, 2) show that stick-slip event velocity and duration vary systematically as a function of distance from the stability threshold. The slowest events occur for $\kappa \approx 1$, with progressively faster events for lower values of κ (Figure 3D, 3E). The peak slip velocity and stick-slip duration for all events, measured after reaching a steady-state (Figure 3C, shaded area), define a complete spectrum of slip behaviors between stable sliding and fast stick-slip (Figure 3D, 3E). For $\kappa \approx 0.7$, slip velocities of several mm s⁻¹ were associated with audible failure events (Figure 3D). For values of κ approaching 1, the duration of slow-slip is on the order of seconds (not producing any audible emissions in the range of human hearing), with lower peak slip velocities (Figure 3D, 3E). The amplitude of the stick-slip events is systematically lower for the slow events (Figure 2), consistent with seismic and geodetic observations for tectonic faults^{4,6,30}. Our data show that the full spectrum of stick-slip behaviors can occur over a relatively narrow range of conditions near the stability phase boundary, and further, that the mode and slip velocity of unstable sliding vary predictably as a function of departure from

this threshold. Although the 1-D spring-slider model is simplified relative to the geometry and rheology of natural fault systems, the predicted stability regimes are remarkably consistent with our laboratory experimental data. It is also consistent with theoretical models that incorporate more complex 2-D fault geometries and elastic interactions²⁰, suggesting that to first order, the mechanics and dynamics of these systems are captured by this relatively simple and elegant model^{15,18,23,29,31}. In total, our results illuminate the key ingredients required for slow earthquakes. Relative to areas where regular earthquakes occur, k_c must remain sufficiently small that it does not greatly exceed the local fault stiffness k . This can occur for specific frictional properties ? small ($b-a$) or large D_c ? as may be the case at the upper and lower edges of the seismogenic zone or in areas of complicated fault zone architecture²⁰. This condition would also be favored by low effective normal stress, as has been suggested in a wide range of settings^{8,9,31-34}. Additionally, we suggest that the mode of fault slip should evolve as tectonic faults accumulate shear strain, or through the earthquake cycle, due to progressive changes in fault stiffness and frictional constitutive properties^{32,34}. Finally, because fault stiffness is proportional to the ratio of shear modulus to rupture nucleation patch size, we expect that regions of large, coherent creep slip, which effectively reduce k , would favor nucleation of slow earthquakes. Our results support previous hypotheses about the role of transitional frictional behavior in driving complex fault slip behaviors^{20,23,31-33}. It is likely that transitional frictional behavior may act in concert with additional processes acting locally within a fault zone to produce the observed spectrum of slip behaviors. A wide range of key natural factors, such as compliant and evolving damage zones, low effective normal stress associated with elevated pore fluid pressure and, fault evolution

are all captured by the stability parameter $\kappa=k/kc$. Ultimately, our results suggest that slow earthquakes and transient fault slip behaviors arise from the same governing frictional dynamics as normal earthquakes, and provide a unified view of the spectrum of tectonic fault slip behaviors.

2.5 Methods

2.5.1 Experimental Apparatus

Experiments were performed in a servo-controlled biaxial shearing apparatus using the double direct shear configuration (Figure 1). Displacements on the normal and shearing axes were measured by Direct Current Displacement Transducers (DCDTs), referenced at the load frame and ram nose. The displacement of the shearing block was measured with DCDTs referenced at the end-platen and the top and bottom of the shearing block (Figure 1). Loads applied to the sample were measured with strain gauge load cells. All transducers are calibrated with instruments and methods traceable to NIST.

Sample Preparation Samples were prepared using steel or titanium side blocks and steel or acrylic (PMMA) central shearing blocks (Supplementary Table 1). The forcing blocks were grooved 0.8 mm deep at 1 mm spacing to eliminate shear at the boundary. We used Min-U-Sil 40 powdered silica (U.S. Silica Co.) to simulate granular fault gouge. The product is 99.5% SiO₂, with traces of metal oxides, and has a median grain diameter of 10.5 μ m. Samples were constructed as 3-mm thick layers, and with 10 cm x 10 cm frictional contact area. Layers were prepared and sheared under 100% relative humidity at room temperature.

2.5.2 Testing Procedure

After samples were placed in the testing machine, a constant normal stress was applied and maintained constant using force-feedback servo control. Samples were allowed to compact and accommodate grain rearrangement before shearing began. Shear was induced by imposing a displacement rate on the central forcing block (Figure 1), using a feedback servo control. The displacement rate was maintained constant at $10 \text{ } \mu\text{m s}^{-1}$ for the majority of our experiments (Supplementary Table 1), and velocity step tests were used to determine the friction rate parameters (a - b) and D_c . We used a range of shear loading stiffnesses k given by the summation, in series, of the apparatus stiffness, the stiffness of the loading blocks, and the stiffness of the layers of fault gouge. The effective loading stiffness of the testing machine $k = k/n$ was altered by using a compliant central forcing block (PMMA) and by changing the applied normal stresses (Figure 2A). We measured k in experiments using a least-squares linear fit to friction vs. shear displacement for the interval $\dot{\gamma} = 0.3 \text{ to } 0.4$ and from the elastic loading portion of stick-slip events (Supplementary Figure 1). Rate-and-state friction parameters were determined (Supplementary Figure 2) using an iterative singular value decomposition technique.

Frictional Stability In the context of frictional stability, the criterion for unstable stick-slip in a simplified 1-D system is defined by the interaction between loading system stiffness k and a rheologic critical stiffness of the fault, k_c : $k \leq k_c = (b-a)/D_c$ (1) where $(b-a)$ is the friction rate parameter and D_c is the critical slip distance²⁹. Negative rate parameters, $(b-a) < 0$, indicate velocity-strengthening behavior, which is inherently stable. Positive values of $(b-a)$ indicate velocity-weakening friction and are

a prerequisite for instability and earthquake nucleation. Within the velocity weakening regime, if the condition in Equation (1) is satisfied (i.e. stiffness of the loading system, k , is less than the critical stiffness; $k \downarrow k_c$), instability occurs because the fault weakening rate, k_c , exceeds the rate of elastic unloading, leading to a force imbalance. For stiffer systems (i.e. $k \downarrow k_c$), in which elastic unloading outpaces frictional weakening, sliding is stable. For convenience, we normalize the stiffness and critical stiffness by the normal stress, appending a prime symbol to denote this; $k' = k/\sigma_n$ and $k_c' = k_c/\sigma_n$. We selected values of k and normal stress for our experiments to span the stability boundary for our fault gouge. To achieve this, we made careful measurements of the evolution of k and k_c with shear strain (Supplementary Figure 1). For a given set of frictional properties, defined by $(b-a)$ and D_c , the ratio k/σ_n defines an effective system stiffness, k' [m⁻¹], that governs sliding stability. In our experiments, the testing machine, sample assembly, and gouge layer together determine the system stiffness. We varied k using different forcing block materials (Supplementary Table 1) and k' via the normal stress.

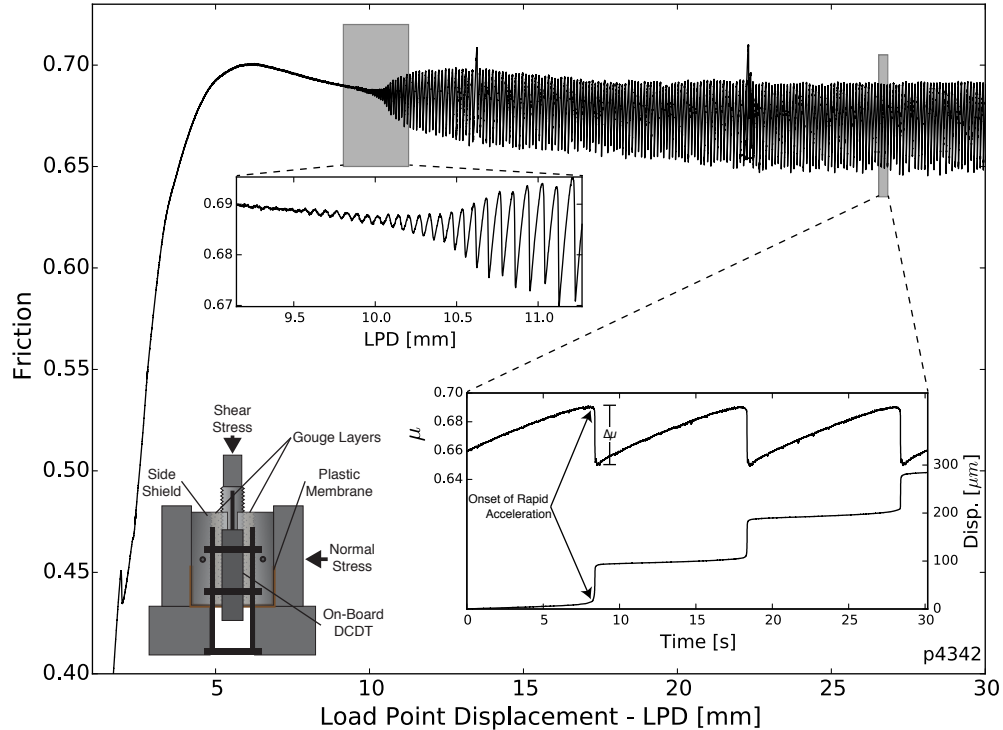


Fig. 2.1. Experimental run plot. Friction data for one experiment (p4342) at a normal stress of 12 MPa and shearing rate of 10 m s⁻¹. The upper inset shows spontaneous emergence of unstable slow slip. Stick-slip amplitude increases gradually over a few mm before reaching steady-state. The lower right inset shows details of fault slip events, note the gradual acceleration at the start of each failure event. The lower left inset shows the double direct shear configuration and locations of displacement transducers. Spikes at 13 mm and 22 mm displacement are due to brief pauses in shearing to reset displacement transducers.

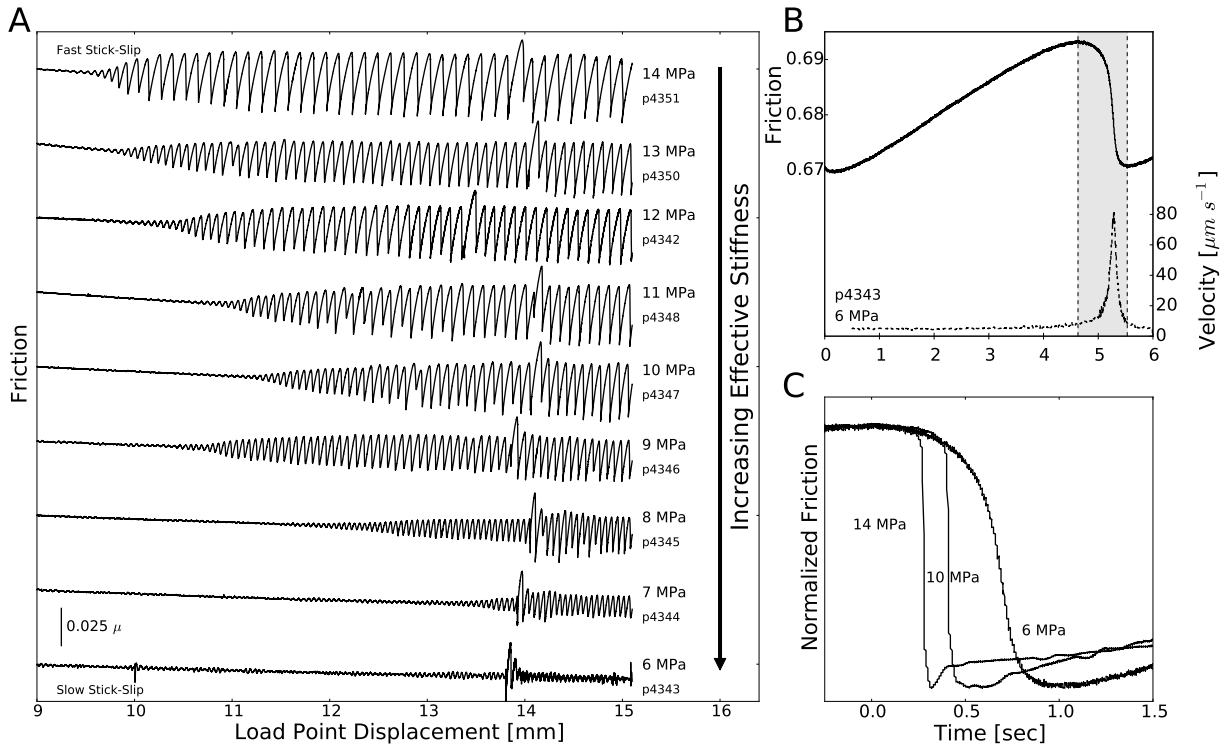


Fig. 2.2. Spectrum of Fault Slip Behavior. A) Friction data for experiments (p43XX run numbers) at different effective shear loading stiffness $k = k/n$. Friction data are offset vertically for clarity. The emergence of slow stick-slip occurs at lower shear displacement, and stick-slip amplitude increases, for higher normal stress experiments. The spikes in friction at 13–15 mm are due to frictional aging caused by brief pauses in shearing to reset displacement transducers. B) Details of friction (solid line) and velocity (dashed) during a stick-slip event with a peak slip velocity of $\sim 80 \text{ m s}^{-1}$, only a few times that of the background loading velocity of 10 m s^{-1} . C) Stick-slip events have systematically longer duration at lower normal stresses. Slip accelerates more slowly and event durations are correspondingly longer than at higher normal stress.

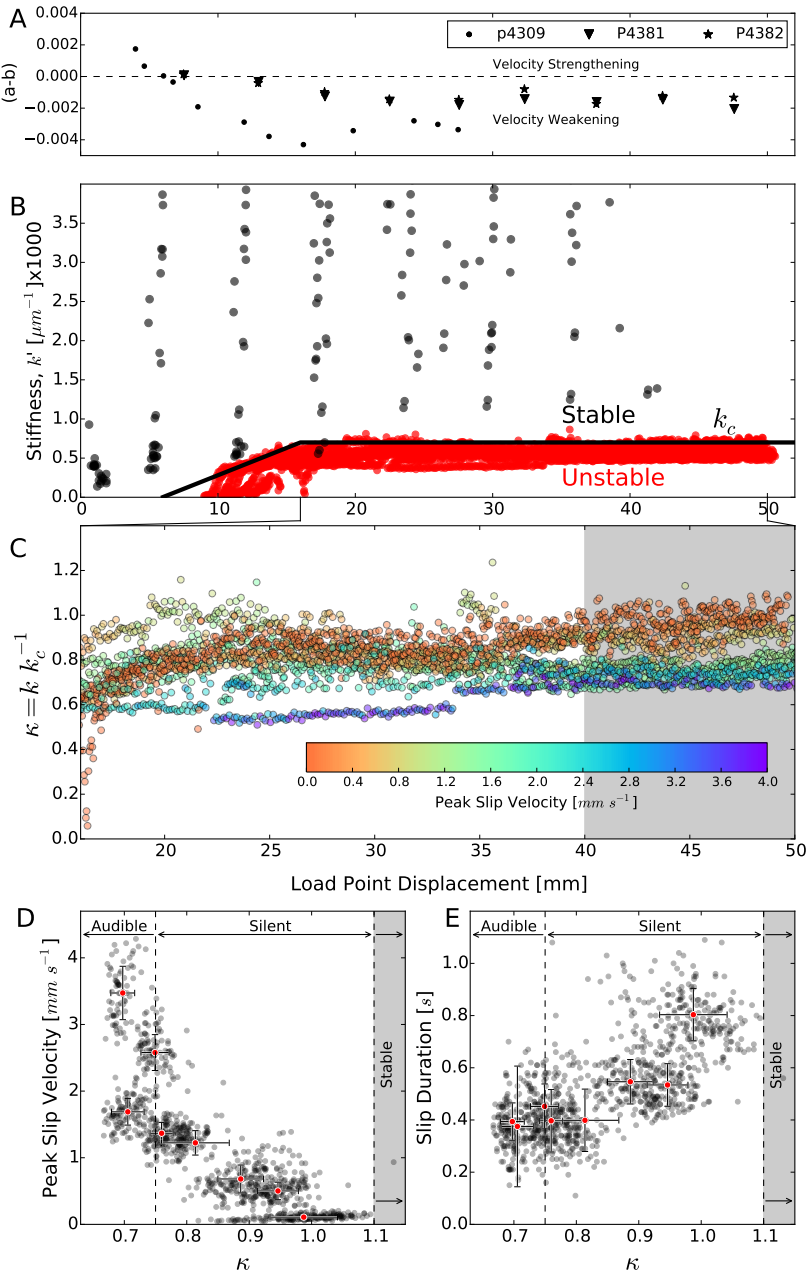


Fig. 2.3. Stick-slip event properties. A) The friction rate parameter ($b-a$) transitions from velocity strengthening to velocity weakening at 5-7 mm displacement. B) Data from 29 experiments showing effective friction stiffness $k' = k/n$ as a function of shear displacement for stable sliding (black dots) and stick-slip events (red dots). The heavy black line defines the evolution of k_c based on the distinction between stable sliding and stick-slip. C) Data for unstable slip events shown in B are color coded by peak slip velocity and shown as a function of shear displacement. Stick-slip is slowest for $\kappa < 1$. The 40-50 mm interval marked by the gray box denotes data used to compile stick-slip properties. D) Stick-slip event velocity and E) duration as a function of normalized critical stiffness $\kappa = k/k_c$. Black dots show data from events in the displacement interval 40-50 mm for 8 experiments; red dots show mean values 1 standard deviation for each experiment.

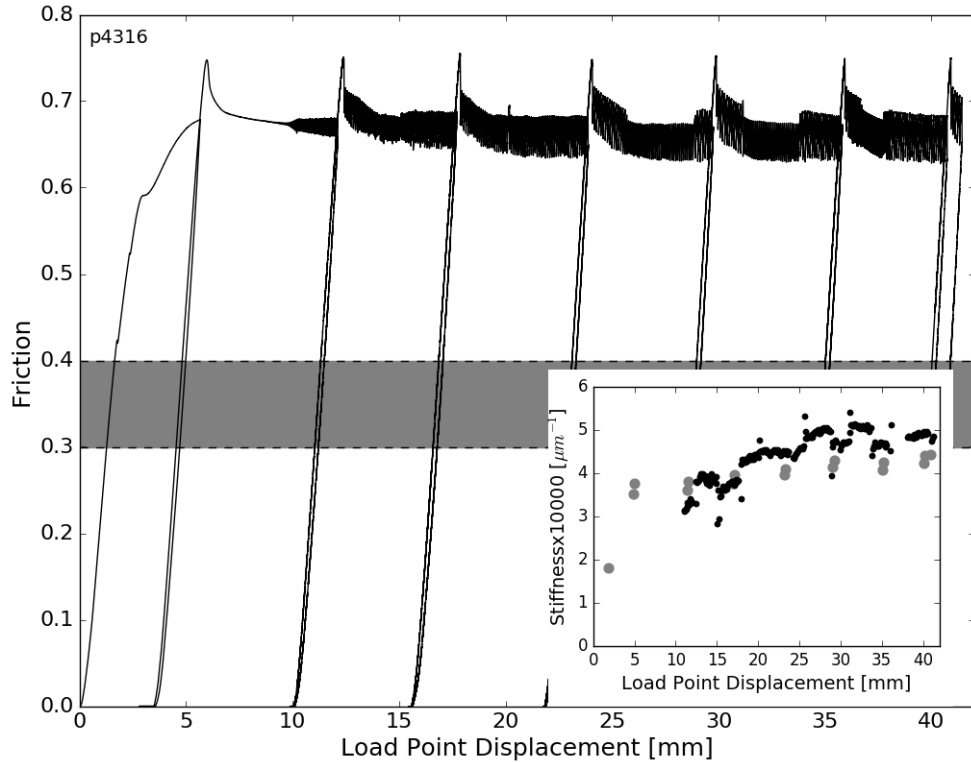


Fig. 2.4. Stiffness during an experiment. Friction data for one complete experiment (run p4316) with shear load-unload cycles. Slow slip events emerge spontaneously at a displacement of 8.5 mm. (Inset) Stiffness measured from unload-reload cycles in the range =0.3-0.4 (large grey circles) and from the slope of the elastic loading segments of individual stick-slip events (small black circles). Both measurements indicate an initial increase in stiffness, caused by shear enhanced compaction. In this experiment we explored multiple shearing rates during slow slip (e.g., for events in the range 27-29 mm and 31-33 mm), which had a clear effect on stick-slip amplitude and stiffness.

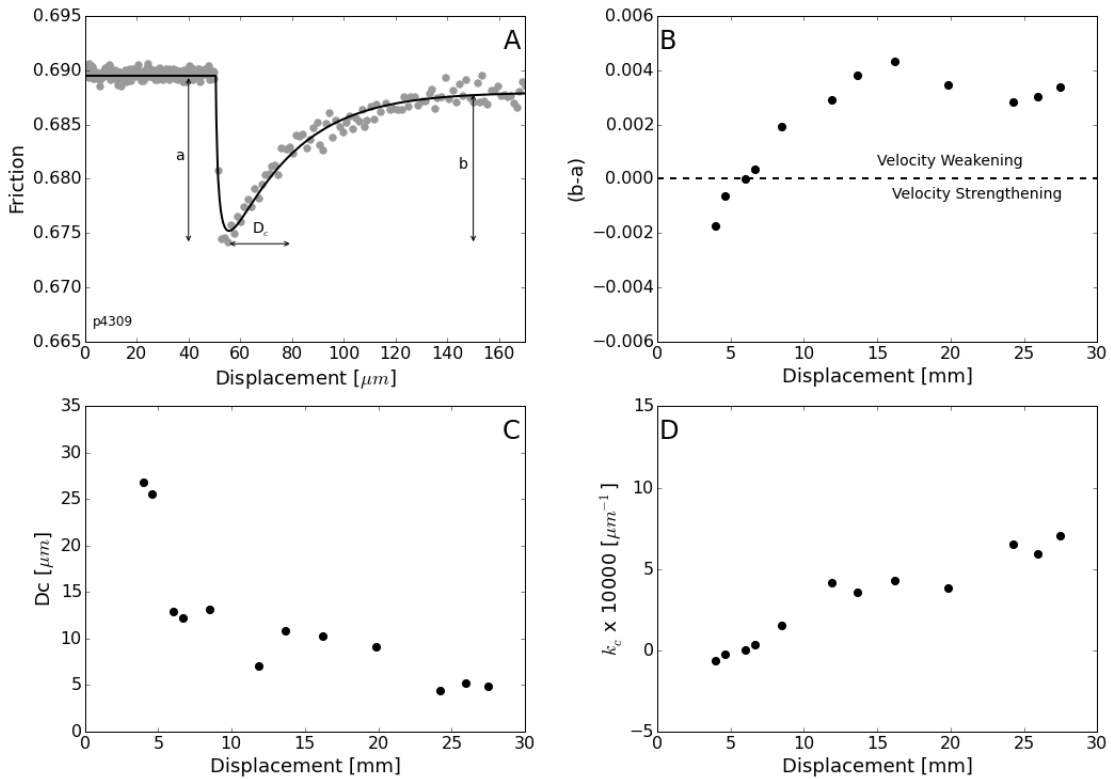


Fig. 2.5. Rate and State Parameters. Data and modeling procedure for obtaining rate-and-state friction parameters and their variation with shear displacement. A) Data from experiment p4309 (grey data points) and model (solid line) for a velocity step test from 10 to 1 m s⁻¹, with illustration of the friction direct effect a, evolution effect b, and critical slip distance D_c . B) Evolution of $(b-a)$ with shear displacement (see also Figure 3A). Note the transition from rate strengthening to rate weakening at 8 mm displacement, after which a steady-state behavior is reached. C) The critical slip distance decreases with shear displacement as frictional steady-state is reached. D) Evolution of the critical stiffness (k_c) with slip.

Experiment	Blocks	Normal Stress [MPa]	Humidity [%]	Comments	Unload/Reload Cycles
p4224	Ti/Acrylic	5	16	Stable - Vel. Steps	N
p4228	Steel	4	100	Stable - Slide Hold	N
p4229	Ti/Acrylic	4	100	Failed	N
p4248	Ti/Acrylic	4	100	Stable - Vel. Steps	N
p4249	Ti/Acrylic	4	100	Stable - Vel. Steps	N
p4267	Ti/Acrylic	2	100	Stable - Vel. Steps	Y
p4268	Ti/Acrylic	8	100	Slow-Slip	Y
p4269	Steel	4	100	Stable - Vel. Steps	Y
p4270	Steel	2	100	Stable - Vel. Steps	Y
p4271	Ti/Acrylic	2	100	Stable - Vel. Steps	Y
p4272	Ti/Acrylic	8	100	Slow-Slip	Y
p4273	Steel	8	100	Stable - Vel. Steps	Y
p4309	Steel	8	100	Stable - Vel. Steps	Y

p4310	Ti/Acrylic	8	100	Slow-Slip	Y
p4311	Ti/Acrylic	8	100	Slow-Slip	Y
p4312	Steel/Acrylic	8	100	Slow-Slip	Y
p4313	Ti/Acrylic	8	100	Slow-Slip	Y
p4314	Steel	12	100	Stable - Vel. Steps	Y
p4316	Ti/Acrylic	12	100	Stick-Slip	Y
p4317	Steel/Acrylic	12	100	Stick-Slip	Y
p4327	Steel	6	100	Stable - Vel. Steps	Y
p4328	Ti/Acrylic	6	100	Slow-Slip	Y
p4329	Ti/Acrylic	6	100	Slow-Slip	Y
p4330	Steel	6	100	Stable - Vel. Steps	Y
p4338	Ti/Acrylic	4	100	Stable - Vel. Steps	Y
p4339	Steel	4	100	Stable - Vel. Steps	Y
p4340	Ti/Acrylic	8	100	Slow-Slip	Y

p4341	Steel	12	100	Stable - Vel. Steps	Y
p4342	Ti/Acrylic	12	100	Slow/Fast Slip	N
p4343	Steel/Acrylic	6	100	Slow-Slip	N
p4344	Ti/Acrylic	7	100	Slow-Slip	N
p4345	Steel/Acrylic	8	100	Slow-Slip	N
p4346	Ti/Acrylic	9	100	Slow-Slip	N
p4347	Steel/Acrylic	10	100	Slow/Fast Slip	N
p4348	Ti/Acrylic	11	100	Slow/Fast Slip	N
p4350	Steel/Acrylic	13	100	Slow/Fast Slip	N
p4351	Ti/Acrylic	14	100	Slow/Fast Slip	N
p4381	Steel	4	100	Stable - Vel. Steps	N
p4382	Ti	4	100	Stable - Vel. Steps	N

Chapter 3

Characterization of Laboratory Slow Earthquakes

3.1 Abstract

sdfsdfs

Chapter 4

Mechanical and hydrologic properties of Whillans ice stream till: Implications for basal strength and stick-slip failure

4.1 Abstract

Ice streams transport large volumes of inland ice to the ocean and play a key role in the mass balance of the Antarctic ice sheet. The rate and style of ice stream basal slip are governed, in part, by the underlying till whose physical properties are poorly constrained. To address this problem, we conducted a suite of laboratory measurements to document the permeability, stiffness, consolidation behavior, and compressional wave speeds of Whillans Ice Stream till samples. We investigated the effects of stepped and cyclic loading on the evolution of the till. Initial permeabilities were $3.8\text{--}4.9 \cdot 10^{-17} \text{ m}^2$ (porosities 28.1–31.8%), which decreased to $2.0 \cdot 10^{-19} \text{ m}^2$ (20.4%) at 10 MPa effective stress. P-wave velocities span from 2.26–3 km/s over this effective stress range, and are well described by an effective medium model. The laboratory measurements were used to parameterize a 1-D numerical model to predict the till’s response to stress perturbations. Perturbations corresponding to tidal periods produce a drained and strengthened layer tens of cm thick. For perturbations over timescales of weeks to months, as expected for till motion over basement features, the drained zone is a few meters thick. This strong layer can become brittle upon unloading, and may facilitate observed stick-slip motion. Extrapolation of our effective medium model suggests low basal effective stresses, on the

order of a few tens of kPa, are needed to produce seismic velocities observed in the field (V_p 1750 m/s; V_s 160 m/s), and provides an approach to quantify and monitor in situ conditions.

4.2 Introduction

Ice streams are regions of fast-moving grounded ice shearing past slower-moving regions of ice. In Antarctica, ice streams discharge over 90% of the interior accumulation over only 13% of the coastline, making them critical to the ice sheet mass balance [Morgan et al., 1982]. Motion of ice streams is complex, as the flow can migrate, stagnate, or even occur in a stick-slip fashion, inducing seismicity [Anandakrishnan et al., 2003; Wiens et al., 2008; Walter et al., 2011]. Many models have attempted to explain the nature of ice stream movement, mostly invoking high basal water pressures, often coupled to soft subglacial sediments that smooth the bed and deform to lubricate motion [Bentley, 1987; Alley et al., 2004; Cuffey and Paterson, 2010]. However, direct measurements sampling the subglacial environment of ice streams remain highly limited [Cuffey and Paterson, 2010].

Ice streaming is often observed to start over sedimentary basins, suggesting that flow begins where the bed first becomes deformable [Anandakrishnan et al., 1998; Bell et al., 1998; Cuffey and Paterson, 2010]. Understanding the mechanical properties of the till immediately underlying the ice is therefore of primary importance, as it may control the flow rate and stability of the ice stream, and ultimately play a key role in the ice sheet mass balance [Tulaczyk et al., 2000; Kamb, 2001]. Sediment-water interactions

are also important in controlling grounding zone processes [e.g. Dowdeswell et al., 2008; Cowan et al., 2014].

Laboratory till-deformation experiments have provided important insights into the rheologic behavior of till [Clarke, 1987; Iverson et al., 1997; 1998; Kavanagh and Clarke, 2006; e.g. Thomason and Iverson, 2008; Iverson and Zoet, 2015], and the measured mechanical properties are comparable to the few reported field measurements, suggesting that the lab measurements can be upscaled effectively [Tulaczyk, 2006]. Since that important earlier work, there has been an increasing interest in the response of till to cyclic loading because of a growing body of evidence indicating that ice stream motion is tidally modulated in many cases. Examples include variations in velocity observed on Kamb Ice Stream (formerly ice stream C) [Anandakrishnan and Alley, 1997], on neighboring Bindschadler Ice Stream (formerly ice stream D) [Anandakrishnan et al., 2003], and elsewhere [Gudmundsson, 2007; Zoet et al., 2012]. Water-pressure observations beneath Whillans and Kamb Ice Streams also documented diurnal variations of 10-20 kPa, consistent with the dominant tidal frequency in the region [Engelhardt and Kamb, 1997; Kamb, 2001].

The downglacier part of Whillans Ice Stream exhibits two seismic motion events per day that are tightly linked to the tide, occurring just after high tide and just before low tide [Bindschadler et al., 2003; Winberry et al., 2014]. Walker et al. [2013] proposed that the rising tide beneath an adjacent ice shelf causes downward bending extending a few ice thicknesses inland, compacting till beneath; the falling tide is then hypothesized to cause upwarp that may pump ocean water upglacier into the grounded flexural zone.

The cyclic loading, with expected amplitude on the order of 50 kPa, leads to the development of ?sticky spots? or asperities with higher shear strength and stiffness than the surrounding material, which promote the observed repeated stick-slip failure [Winberry et al., 2011; Pratt et al., 2014; Winberry et al., 2014; Walter et al., 2015]. Features observed near the grounding zone of Whillans Ice Stream, including upwarped surface topography, folded internal reflectors that indicate increased basal drag, and water/sediment exchange at the grounding line, are consistent with flexural behavior producing sticky spots through till compaction [Christianson et al., 2013; Horgan et al., 2013].

This prior work leads to a conceptual model wherein the interplay of material properties and time-dependent hydraulic processes produces a layer of till sufficiently stiff to support brittle stick-slip failure. Till hydrologic and consolidation properties ultimately govern the time scales of pore pressure diffusion and drainage [Tulaczyk et al., 2000], which are central to the proposed tidal pumping mechanism, and also to hypothesized mechanisms of till weakening through generation of high pressures in front of ploughed debris [Thomason and Iverson, 2008]. Here, we report on a suite of tri-axial deformation experiments on till from beneath Whillans Ice Stream that include measurements of porosity, permeability, stiffness, and acoustic velocity under both stepped and cyclic loading conditions, aimed at understanding temporal and spatial scales of drainage-modulated processes in the till. We then incorporate these laboratory data into a transient 1-D model that couples till deformation (consolidation) and drainage to explore the hypothesis that cyclic loading produces a brittle layer that is able to support stick-slip failure.

4.2.1 Geologic Setting

Whillans Ice Stream, formerly ice stream B, is one of five major ice streams located on the Siple Coast of Western Antarctica (Figure 1). Whillans is considered a fast-flowing ice stream, with over 400 m of surface displacement per year, though its velocity is currently decreasing and it may become stagnant within 100-200 years [Whillans and Van der Veen, 1993; Joughin et al., 2005]. The ice is approximately 1 km thick at the UpB camp, located approximately 400 km from the grounding line, where the ice stream has been most intensively studied [Blankenship et al., 1986; 1987; Rooney et al., 1987; Engelhardt et al., 1990]. The ice flows over several meters of unconsolidated till that lie unconformably over a poorly lithified sedimentary sequence. Temperatures at the ice-till interface are at approximately the pressure melting point of -0.8 C [Engelhardt et al., 1990; Tulaczyk et al., 1998]. A surface slope of 0.0013–0.003 provides an average gravitational driving stress of 13–20 kPa [Alley, 1993; Tulaczyk et al., 1998].

Cores of till were obtained at the UpB camp during field seasons from 1989–1993 (Figure 1). This unique suite of samples has been subjected to mechanical testing to measure several geotechnical properties, including texture, composition, and strength as a function of strain, strain rate, and effective stress [Kamb, 1991; Tulaczyk et al., 1998; 2000]. After study, the samples were stored at room conditions (ambient humidity and temperature) by K. Licht at Indiana University-Purdue University Indianapolis and generously made available for this work. During drilling, observed fluid pressures in the borehole were within 50 kPa of the 9 MPa ice overburden (i.e. effective normal stresses less than 50 kPa and perhaps much less [Tulaczyk et al., 2001]), such that

shear stresses at the bed are much less than those required to significantly deform the ice internally. This is consistent with laboratory shearing experiments showing that the cohesion of the tills is generally negligible and their shear strength is only a few kPa under a normal stress of 9 kPa [Kamb, 1991; 2001]. Such a low shear strength has led to the interpretation that rapid surface displacement of the ice stream is primarily the result of basal processes (sliding between ice and till, ploughing, and till deformation) [Blankenship et al., 1986; 1987; Engelhardt and Kamb, 1997].

4.3 Materials and Methods

4.3.1 Sample Preparation

We tested two samples from the Up-B expedition, obtained from depths of 0.3-0.4 m and 1.6-1.7 m (Samples 1744 and 1754) below the ice-till interface in borehole 89-1-4 (Figure 1). The till in general is a dark-grey unstructured diamicton, consisting of sand, silt, and clay-sized fractions in a bimodal distribution with scattered pebbles [Tulaczyk et al., 1998]. Because the samples were stored at ambient conditions for many years, we used an ultrasonic humidifier with purified water to carefully re-hydrate the intact core samples. The samples were then trimmed into 2.54 cm diameter cylinders with lengths of 2.1 and 2.4 cm, with care taken to subsample only the most undisturbed parts of the core. Initial sample dimensions were recorded before jacketing and testing. The samples, together with end platens and porous frits, were jacketed with heat shrink tube. The shrink jacket was then sealed with tie-wire, and a thicker, stronger confining jacket was applied just over the ends of the specimen and secured with hose-clamps (Figure 2).

4.3.2 Tri-axial Loading

Samples were loaded into a tri-axial pressure vessel. Confining (radial) and axial stresses were set to be equal in our tests (isostatic stress condition wherein $\sigma_1 = \sigma_2 = \sigma_3$), and applied via a silicone oil pressurized by a piston syringe pump. Sample pore fluid pressure was controlled at each sample face using two additional high-precision syringe pumps. Prior to deformation, the samples were allowed to equilibrate for 24 hours under a pore pressure of 200 kPa and confining pressure of 300 kPa (effective pressure of 100 kPa) to ensure complete fluid saturation. During the equilibration stage, only one pore fluid pump was used to maintain pore pressure. Pore fluid pumps and the pressure vessel were maintained at a constant temperature of 29.5 $^{\circ}$ C using a temperature chamber that surrounds the apparatus to minimize thermal expansion effects. Both pressure and volume were monitored continuously in both of the pore fluid pumps to a precision of 1 kPa and 1 mm³ respectively, to document volumetric strain and changes in sample porosity.

The final porosity of the sample is obtained by weighing the fully saturated sample immediately after the test, and again after oven drying at 110 C for 24-48 hours [ASTM D2216]. The difference indicates the mass of interstitial water in the sample, from which the pore fluid volume is defined (assuming a water density of 1000 kg m⁻³); the total volume of the sample is determined from direct measurements of its dimensions using a micrometer. Using the final porosity value determined by this approach, porosity throughout the experiment is then calculated from the pore fluid pump volume measurements that record sample volume change (i.e. fluid expulsion or uptake).

Two loading paths were used to test the till samples. First, a simple incremental loading path was applied, in which the effective stress was increased step-wise and then allowed to equilibrate in a series of stages. Equilibration was defined as the point when pore volume and sample length were no longer changing significantly. Permeability and acoustic velocity were then measured after equilibration at each load step, as described in detail below. The second testing profile was designed to emulate cyclic loading as is hypothesized to result from tidally-driven ice flexure [Walker et al., 2013]. We achieved this by applying a sequence of sinusoidal loading patterns with a period of 24-hours and amplitudes of 20, 50, 75, and 150 kPa. The amplitude of each sinusoid pattern was maintained for 5-10 days (5-10 cycles), starting with 20 kPa and increasing sequentially. Pore volumes and axial strain were monitored continuously during the tests, and permeability was measured following equilibration after each set of cycles at a given amplitude.

4.3.3 Permeability and Compressibility

The permeability k [m^2] of the samples was determined using a steady-state constant-head method. The upstream and downstream pore pressure pumps were held at constant pressures to maintain a pressure gradient across the specimen (ranging from 20-80 kPa in our tests). After reaching a steady-state, defined by equal flow rates in the two pumps to within 10%, water flux through the sample was determined from pump volume records (Figure 3). We then computed permeability using Darcy's relation: (1) where Q is the steady-state flow rate [$m^3 s^{-1}$], η is the dynamic fluid viscosity (0.0008 Pas at 29.5C), L is the sample length [m], A is the cross-sectional area of the sample [m^2], and ΔP is the difference in pressure between the upstream and downstream pumps

[Pa]. For each effective stress step, we conducted permeability tests with three different pressure gradients, and report the permeability as the mean of these values (all data are provided in the Supplementary Materials). Sample compressibility, β [Pa⁻¹], is calculated from the total sample volume change, as recorded in pore-fluid pump volumes, resulting from a known change in effective stress: (2) where V and dV are sample volume and change in sample volume [m³], respectively, and dP_e is the increment in effective stress [Pa].

4.3.4 Acoustic Velocity

Compressional wave velocity was determined using a time-of-flight technique through the sample, corrected to account for travel time through the end-caps and porous frits [Knuth et al., 2013; Carpenter et al., 2014]. The end-caps used to apply axial load to the sample were equipped with lead-zirconate-titanate (PZT) transducers (Figure 2). A -900 VDC pulse was applied to one (transmitting) transducer, creating a propagating elastic wave with a center frequency of approximately 500 kHz. The signal from a second (receiving) transducer in the opposite end cap was recorded by a high-speed data acquisition system with a resolution of 16-bits over a 1 V range at 50 MHz sampling rate (Figure 4). To reduce noise in individual waveform records, 100 waveforms were recorded and stacked to form one record. This was repeated a minimum of 25 times for each effective stress state. The P-wave arrivals are emergent at low stresses, but can be resolved accurately with a pattern cross-correlation technique, in which a pattern arrival is correlated with measured waveforms and the point of maximum correlation picked

as the arrival. Velocity is then calculated from the corrected travel times for the first arrivals, and using directly measured sample length.

Acoustic velocities (both P- and S-wave speeds) in unconsolidated sediments and soils can also be predicted by effective-medium models [e.g. Dvorkin et al., 1999; Helgerud et al., 1999]. Application of such a model can provide a key link between in situ physical properties and conditions, including effective stress and pore-fluid pressure, and borehole or field-based geophysical data. Here we compose an effective-medium model following Dvorkin et al. [1999] (see Appendix for details), incorporating X-Ray Diffraction (XRD) data that define the bulk till mineralogy, and then benchmark the model against our laboratory measurements of P-wave velocity.

4.4 Results

The initial porosity of both core samples was 28-32%. This is lower than the estimated in situ porosity of 40% [Engelhardt et al., 1990], and may be attributed to storage and sampling artifacts. Samples were obtained with a piston corer; the hammering action of the coring process may have compacted the samples from their in situ state. After initial characterization and cataloging, the samples were stored at room temperature and humidity, and may have been subject to pore-space reduction associated with desiccation and matrix suction effects. To inform our effective-medium modeling, we conducted X-ray diffraction analyses on material from the two cores of till from beneath the ice stream that we tested in our deformation experiments (Figure S1). The diffraction patterns from both samples show almost identical mineralogy, with minor background

count differences, and indicate that the till consists primarily of clay minerals, with a significant quartz fraction and some feldspar family minerals (Table 1).

4.4.1 Consolidation and Compressibility

Our stepped loading tests (SAL1744) find a systematic decrease in porosity and concomitant increase in stiffness with increasing effective stress, following a strain-hardening trend typical of soils and sediments [Wood, 1990]. During stepped-loading, the effective confining pressure was increased from 100 kPa to 1 MPa in 100 kPa steps, decreased to 50 kPa, and then increased again (reloaded) to 10 MPa (Figure 5A). Volumetric and axial strain show very similar trends during the entire step loading test. The initial loading stages produced an integrated volumetric strain of about 3%, which was mostly recovered during unloading. Final strains of 6-10% were achieved at 10 MPa effective stress (Figure 5B). The initial porosity of the sample was 28.1% and the initial compressibility was 5×10^{-8} Pa⁻¹. At 10 MPa effective stress, the porosity was reduced to 20.4% and compressibility to 4.8×10^{-9} Pa⁻¹. Unloading the sample resulted in modest poroelastic rebound to a porosity of 23.6% (Figure 6B). During our cyclic loading tests (SAL1754), strain continued to accumulate with each cycle, even though the effective stresses did not exceed those applied in preceding cycles. The amount of incremental strain decreased asymptotically with each set of cycles at a given amplitude, and then increased sharply after increasing the amplitude of the oscillations (Figures 5C,D, S2). Initial loading produced 0.88% axial strain. After 10 cycles of 20 kPa, axial strain increased to 0.95% (corresponding to a porosity of 31.2%). After 25 cycles of 50 kPa, strain increased asymptotically to 1.04% (porosity of 31%); 10 cycles at 75 kPa increased

strain to 1.09% (porosity of 30.5%). The final 15 cycles at 150 kPa increased the strain to 1.77% and reduced the porosity to 28.3%.

4.4.2 Permeability

Permeability decreased systematically with loading, exhibiting nearly two orders of magnitude decrease upon loading to 10 MPa effective stress. Permeability decreases most rapidly early in the loading history, consistent with porosity loss and strain hardening. The samples had an initial permeability of 3.8×10^{-17} m² and 4.9×10^{-17} m² at an effective stress of 100 kPa, consistent with values reported for other till samples (110-19 m² to 110-13 m²) [Freeze and Cherry, 1979], and slightly lower than values of 210-16 m² reported from large scale field measurements at the Whillans drill site taken by a falling head permeameter [Engelhardt et al., 1990]. We note that the higher permeabilities reported from the field measurements may reflect a component of non-Darcian flow at the ice-till interface. At 1 MPa effective stress (corresponding to 25.3% porosity), permeability was reduced by a factor of 15-20, to 2.5×10^{-18} m², and recovered only slightly to 3.3×10^{-18} m² upon unloading. After loading to 10 MPa effective stress (20.4% porosity), permeability was reduced to 2.0×10^{-19} m² (Figures 6A,B). The cyclic loading test exhibited about an order of magnitude reduction in permeability over 60 loading cycles, despite the fact that the loading oscillations did not exceed the peak effective stress previously applied to the specimens, consistent with the trends of strain and porosity loss (c.f. Figures 5C-D). After 10 load cycles of 20 kPa (resulting in a porosity of 31.2%), the permeability of the specimen was reduced by a factor of 1.6, from an initial value of 3.8×10^{-17} m² to 2.4×10^{-17} m². This was followed by 25 load cycles of 50 kPa (31%

porosity) in which the permeability was reduced to $1.310\text{-}17 \text{ m}^2$. Another 10 cycles of 75 kPa loading reduced the permeability to $1.110\text{-}17 \text{ m}^2$ (30.5% porosity). The final cycle set consisted of 15 cycles at 150 kPa, and the permeability was reduced to $3.910\text{-}18 \text{ m}^2$ (corresponding to 28.3% porosity) (Figure 6C,D).

4.4.3 Acoustic Velocity

P-wave velocity increased systematically with effective stress in our stepped loading test. At an effective pressure of 0.7 MPa (corresponding to 26.4% porosity), V_p values of 2.26 km/s were observed, increasing to nearly 3 km/s at 10 MPa effective stress (20.4% porosity) (Figure 7A). The compressional wave velocity data from the laboratory are fit reasonably well by our effective medium model, assuming a critical porosity of 40% and grain contact number of 8 (Table 1; Appendix). Extrapolation of the effective medium model to slightly lower effective stresses predicts that in situ effective stresses $\gtrsim 100 \text{ kPa}$, and in situ porosities $\lesssim 40\%$ would be required to produce P and S wave velocities of 1750 m/s and 160 m/s, respectively, that are observed via field experiments [Blankenship et al., 1986; 1987; Luthra et al., 2016]. This provides new evidence supporting inferences of low effective stresses, and thus low shear strength, at the base of the ice stream (Figure 7).

4.4.4 Hydrologic Model

To explore the implications of our laboratory measurements for the hypothesized development of a ?hard layer? that enables stick-slip motion of the ice stream, we developed a simple 1-D transient finite-difference model implemented with the Python

package FiPy [Guyer et al., 2009] that simulates coupled compaction and drainage in a vertical column of till with heterogeneous properties (Figure 8). Because permeability and compressibility vary strongly and nonlinearly with effective stress, we use a 0.01 m nodal spacing and a time step of 0.01 - 1000 seconds, increasing as the model changes become more gradual. This allows us to quantify the evolution of till porosity, stiffness, permeability, and effective stress in response to perturbations at the ice stream bed. By incorporating the constitutive relations obtained from our laboratory measurements (Figure S3) we account for the significant and non-linear evolution of porosity, permeability, and compressibility during compaction [Skarbek and Saffer, 2009] that are typically not included in simple models having homogeneous and/or time-invariant physical properties [e.g. Gibson, 1958; Wissa et al., 1971]. This model provides first-order insights into the time-dependent behavior of the system and the time and length scales of drainage relevant to subglacial processes. The model is initialized with a hydrostatic pressure gradient, and the vertical effective stress at the top boundary (ice-till interface) is then increased instantaneously to explore the response to a perturbation. This value is then held constant (Dirichlet boundary), and the till layer is allowed to evolve. The bottom boundary, 10 m below the till-ice interface, is controlled with Neumann boundary conditions of zero flux to emulate the harder semi-consolidated bedrock on which the till is deposited. The upper boundary is physically equivalent to allowing drainage into an ice-contact water system at the specified pressure, of the sort known to exist beneath Whillans Ice Stream [Engelhardt and Kamb, 1997; Kamb, 2001]. The governing equation for fluid flow is:

where h is hydraulic head [m], s is specific storage [m⁻¹], and K is hydraulic conductivity [m s⁻¹]. Specific storage is in turn defined from compressibility, where α is the till compressibility and β is the fluid compressibility and the sample porosity. (4) Hydraulic conductivity is defined from permeability by: (5) where ρ is the fluid density [kg m⁻³], g the acceleration of gravity [m s⁻²], and η is the fluid viscosity [Pa s]. Porosity, permeability, and compressibility are determined for each model cell from empirical least-squares fits to our experimental data (equations 6-8), and updated at each time step as hydraulic head and effective stress evolve (Figure 8A). The permeability prediction from our empirical fit slightly under predicts observed permeabilities at the highest porosities, but errors are less than a factor of two and inconsequential in the modeling scheme. As the porosity is rapidly reduced during initial drainage, the empirical relation and model quickly converge. The model also provides a minimum estimate of active layer depth due to the slight under prediction of permeability in the early stages of the model run. (6)

(7) (8) For a simple drop in pressure at the top of the till (or equivalently a step increase in pressure within the till caused by mechanical loading), there is initial drainage to the top of the column. The uppermost few cm of the till quickly drains, and as a result its porosity and permeability are significantly reduced and its stiffness increases (Figure 9). This results in self-limited drainage from the top of the layer relative to that predicted for a homogeneous case (i.e. in which the till properties are time invariant) [Wissa et al., 1971], and leads to the development of a thin zone at the top of the till where consolidation has progressed. This zone is characterized by increased effective vertical stress (and thus increased shear strength), increased stiffness, and decreased porosity (Figure 9). As the till layer responds and drains, a minimum in vertical effective stress, and in

shear strength, propagates downward. Over timescales of tidally-driven perturbations, this minimum in strength reaches approximately 0.7 m; by 30 days it propagates to 4 m. Upon unloading, during upward flexure of the ice, the till is in an overconsolidated state and has become embrittled [Wood, 1990], possibly promoting seismogenic failure.

4.5 Discussion

Despite the fact that samples were stored at room conditions for a number of years, we expect their properties to be representative of in-situ conditions. Once rehydrated during sample carving, then saturated in the pressure vessel and loaded to effective stresses of 100 kPa the properties should track undisturbed samples. Our observations of systematic behaviors and trends as well as generally low permeability measurements suggest that any permanent effects from dry storage are negligible. In fact, it is likely that piston coring had a larger effect than desiccation on the sample properties.

4.5.1 Till physical properties and relevance to sticky spot development

The evolution of porosity, permeability, and stiffness observed in our experiments is consistent with the conceptual model of a hard layer of till that enables stick-slip behavior. For example, during compaction in our experiments, till compressibility was reduced by a factor of 7 from an initial value of 710-8 Pa⁻¹. We also observed that when subjected to load cycling, the till progressively compacts as a result of small-amplitude fluctuations in stress, even if the effective stresses never exceed values previously experienced by the material. These processes are likely to be increasingly important near the grounding line, where ice flexure due to ocean tides is continually changing the stress

state at the base of the ice and possibly produces persistent brittle layers of till. Drainage times obtained from the 1-D hydrological model are also consistent with this conceptual model. In a 12 hour tidal period a compacted zone a few tens of centimeters thick can form. In contrast, over timescales of a month, the expected drainage length is several meters, suggesting that any ice stream movement over sticky or rough bed features with a wavelength greater than 30 m should have enough time to fully equilibrate, drain, and consolidate. The decadal time scale for ice motion across the modeled flexural wavelength (a few km in most settings) of the grounding zone gives time for repeated tidal cycling to integrally effect large changes (i.e. decreased porosity and permeability, and increased stiffness) in till moving with ice or slower than the ice. To help test hypotheses about the in situ state of the till, direct measurements of pore pressure and effective stress are essential. Unfortunately, there are very few borehole measurements of key properties, and for Whillans ice stream they are concentrated at the UpB site. A calibrated effective medium model, defined by our laboratory measurements (Figure 7), can be used in conjunction with field seismic studies to estimate the in situ vertical stress, porosity, and pore pressure of the till. This allows mapping of these generally elusive physical properties using geophysical surveys in other areas, including those near known ?sticky spots? [e.g. Luthra et al., 2016], and provides a new line of evidence for inferred low in situ effective normal stresses and elevated pore pressures along the ice stream bed.

4.5.2 Shearing Processes

The ice-stream is heavily influenced by tidal signals on a diurnal time scale. These periodic stressing events and patchy basal hydrologic connection can result in load/unload cycles over large regions. According to our model, such daily perturbations likely have little influence below a few tens of centimeters in the till. For longer term perturbations, such as passing over hard/rough spots in the flow path, the influenced layer could be on the order of several meters. The prediction of a shallow active layer is consistent with other work and matches observations in the field on glaciers with accessible till layers [Boulton and Hindmarsh, 1987; Truffer et al., 2000; Kamb, 2001]. Under such periodic loading, upward drainage will reduce porosity just beneath the ice-till interface, producing a low-permeability cap. This layer will limit hydraulic communication between deeper till and any ice-contact water system, and upon subsequent unloading will be overconsolidated. A confined interval of lower effective stress, higher porosity and lower strength then will underlie this upper compacted centimeters-thick layer of till (Figure 9). The overconsolidated ? and thus brittle ? layer could easily break internally and/or slide on the till below. The depth variation in consolidation state and effective stress likely means that solid body sliding, ploughing, internal deformation, and brittle faulting could all be active in accommodating the movement of the ice stream [Iverson et al., 1998; Iverson and Iverson, 2001; Thomason and Iverson, 2008]. During shearing, the upper layer of till will be remolded and dilated, potentially ?resetting? its properties and re-introducing porosity and permeability. Alternatively, if the till properties are not

completely reset by shearing, a widespread, persistent thin, hard, and brittle layer of till could develop.

4.5.3 Effective Stiffness Feedback Mechanism

The proposition of a thin active layer of plastic till poses a fundamental problem. Such materials are generally not associated with stick-slip movement and seismic radiation like that observed on many ice streams [Anandakrishnan and Bentley, 1993; Anandakrishnan and Alley, 1997; Lipovsky and Dunham, 2016]. In fact, the movement of ice streams is analogous to that of tectonic slow-slip phenomena with a very regular period and small rupture area/rupture time ratios [Ide et al., 2007; Peng and Gomberg, 2010]. There are multiple proposed controls on this style of fault rupture, including high pore pressure and concomitant low effective normal stress, and complex rheologies that allow instabilities to nucleate, but which limit slip speeds by strengthening at higher sliding velocities [Peng and Gomberg, 2010; Rubin, 2011]. Recent work shows that for frictional failure, the stiffness of the loading system relative to a rheologically defined critical stiffness of the sliding region (termed k_c) may also be a key factor in controlling the style and speed of frictional slip [Scholz, 2002; Leeman et al., 2015; 2016]. Systems that are less compliant (stiffer) than the critical stiffness are inherently stable and exhibit aseismic creep. Systems that are more compliant (less stiff) than the critical stiffness are unstable, because any slip that initiates causes weakening that outpaces the rate at which accumulated elastic strain energy can be released. The mismatch between weakening and energy release results in a force imbalance that produces acceleration and dynamic stick-slip events. The rheologically defined stiffness (k_c) is a function of the

frictional properties of the sliding interface, as well as the effective normal stress across it; lower normal stress decreases k_c and leads to a tendency for stable slip. Systems at or near the stability threshold in which the stiffness approximately matches that of the critical stiffness may exhibit periodic slow-slip events, much like those observed in nature. It is possible that a feedback mechanism operates to buffer the aggregate stiffness of the highly deformable ice stream system at approximately the critical stiffness. Such a buffering effect could maintain the system in a regime of slow-slip failure, regardless of the shearing state of the till. In a system that is stiffer than k_c , we expect steady basal sliding. However, this rapid motion will result in vigorous reworking of the till, dilating it, reducing the system stiffness and bringing it nearer to or below the stability threshold. For systems more compliant than k_c , there would be long periods of ?sticking? during which consolidation and stiffening would occur as the system is loaded. From cyclic loading tests, we expect the till below the actively deforming layer to compact over multiple tidal cycles, also leading to stiffening. Increasing stiffness would drive the system back toward stability (i.e. toward k_c). These competing effects could buffer the aggregate stiffness near the stability threshold. When coupled with low effective normal stress along the base of the ice stream, this may offer a plausible explanation for failure in slow but periodic transient slip events.

4.6 Conclusions

Since the discovery of soft, deformable till beneath ice streams in the 1980?s, there have been more questions than answers about slip partitioning, till rheology, and the connection between basal hydrology, ice-till interaction, and ice stream flow, particularly

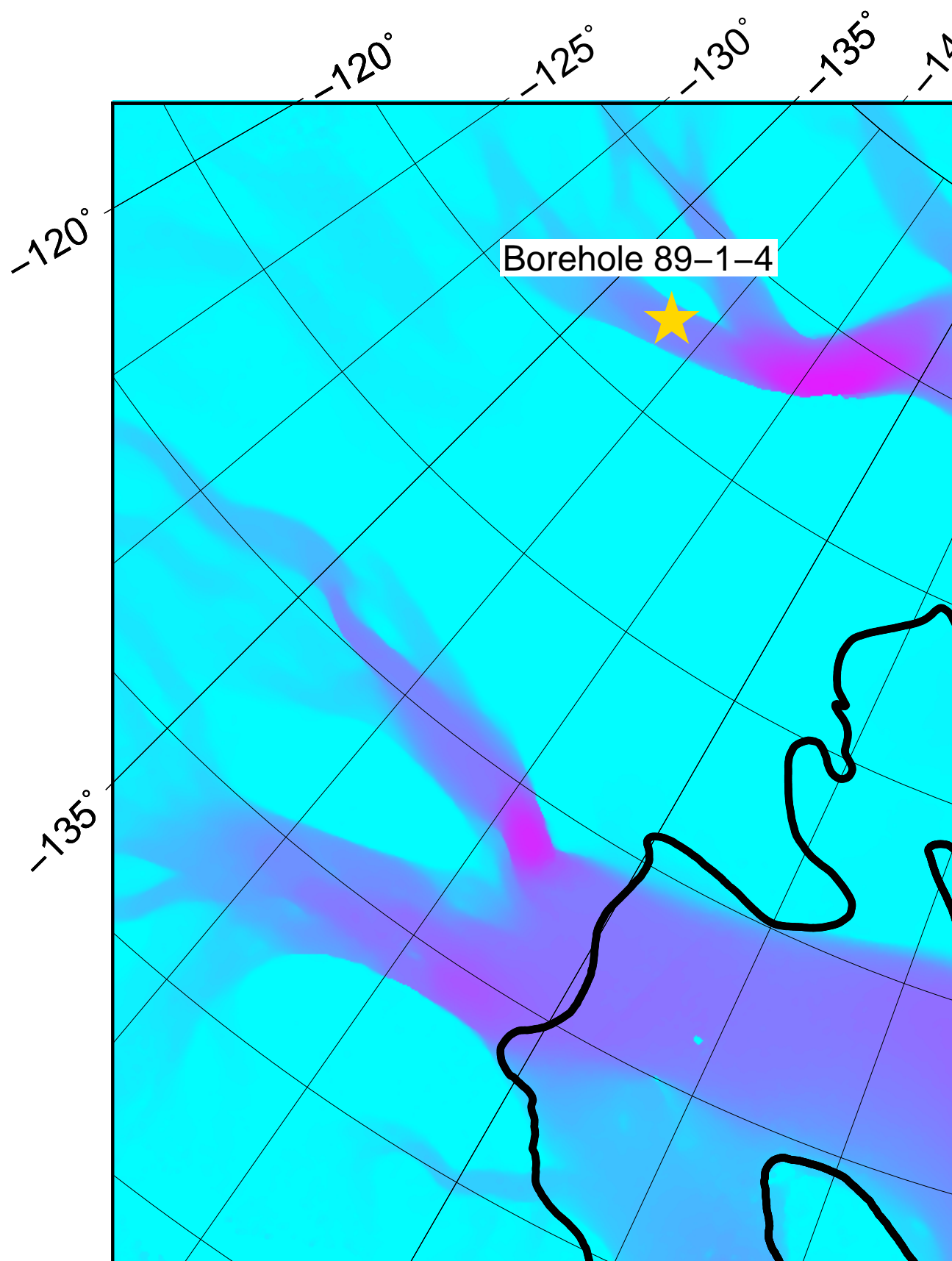
for fast-flowing streams. We provide laboratory data that can be used to constrain hydraulic property evolution in full ice-sheet models, and we show that tidal loading can have lasting effects on till properties that may or may not be completely erased during shearing and dilation. Our laboratory measurements and modeling provide a unique set of data and verification that is consistent with a limited body of existing work. We document systematic decreases in porosity and permeability with increasing effective stress. We also observed increasing stiffness, consistent with porosity reduction and strain-hardening behavior. Our cyclic loading tests show that non-recoverable strain, and associated reduction in permeability and increases in stiffness, may accumulate in till that is diurnally loaded through tidal processes. A numerical model incorporating these laboratory observations illustrates that the development of a thin strengthened and overconsolidated layer of till resulting from tidally-driven loading is plausible. The development of such a layer may explain strengthened ?sticky spots? at the base of the ice stream in areas where flexure is focused [Walker et al., 2014; Winberry et al., 2014]. Incorporation of our physical property measurements into more complex ice flow models could be a step towards reproducing the physics of stick-slip events. Finally, our measurements of acoustic velocity, coupled with effective medium modeling, defines - for the first time, and based on first-principles - a site-specific transform linking acoustic velocity and effective stress immediately beneath the ice stream. The results provide new and quantitative evidence for basal effective stresses ≥ 100 kPa as inferred in previous work or measured in isolated locations in boreholes, and highlights a potentially fruitful approach to quantify and map basal conditions regionally. Furthermore, the low effective stress and near critical stiffness conditions believed to exist at the bottom of stick-slipping

ice streams are analogous to conditions believed to exist in environments of tectonic slow-slip. Merging glacial and tectonic observations with ice streams serving as a natural laboratory may yield new and valuable insight to the conundrum presented by slow-slip and tremor observations.

4.7 Effective Medium Model Formulation

Mineral	Volume Percent	Bulk Modulus [GPa]	Shear Modulus [GPa]	Density [kg/m ³]
Quartz	23.73	36.6	45	2650
Clay	50.49	48	20	2626
Feldspar	25.78	76	26	2560

Table 4.1. Physical parameters used to construct the effective medium model of compressional and shear wave velocities. Values are based on Dvorkin [1999] and Wang [2001].



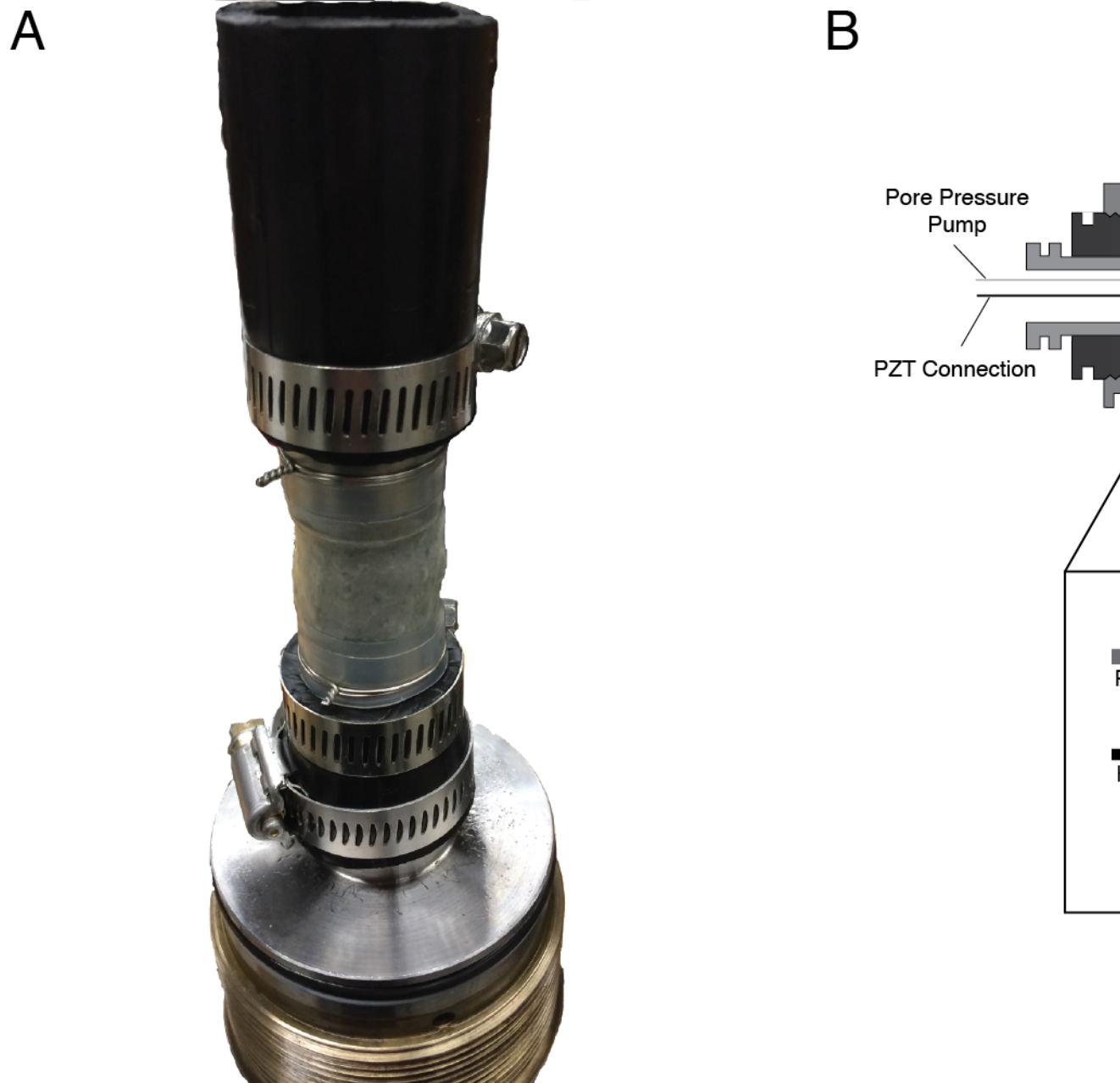


Fig. 4.2. A) The completed sample assembly ready to be loaded into the pressure vessel. B) Schematic diagram of the tri-axial loading cell. Heat shrink tubing was used as a thin, low-strength jacketing material. A hydraulic syringe pump provided isotropic confining and axial loading stresses. A linearly variable displacement transformer (LVDT) measured sample strain. Two high-precision water syringe pumps imposed a hydraulic head to determine sample permeability. Piezoelectric transducers in the loading platens measured the elastic wave travel time through the core (inset).

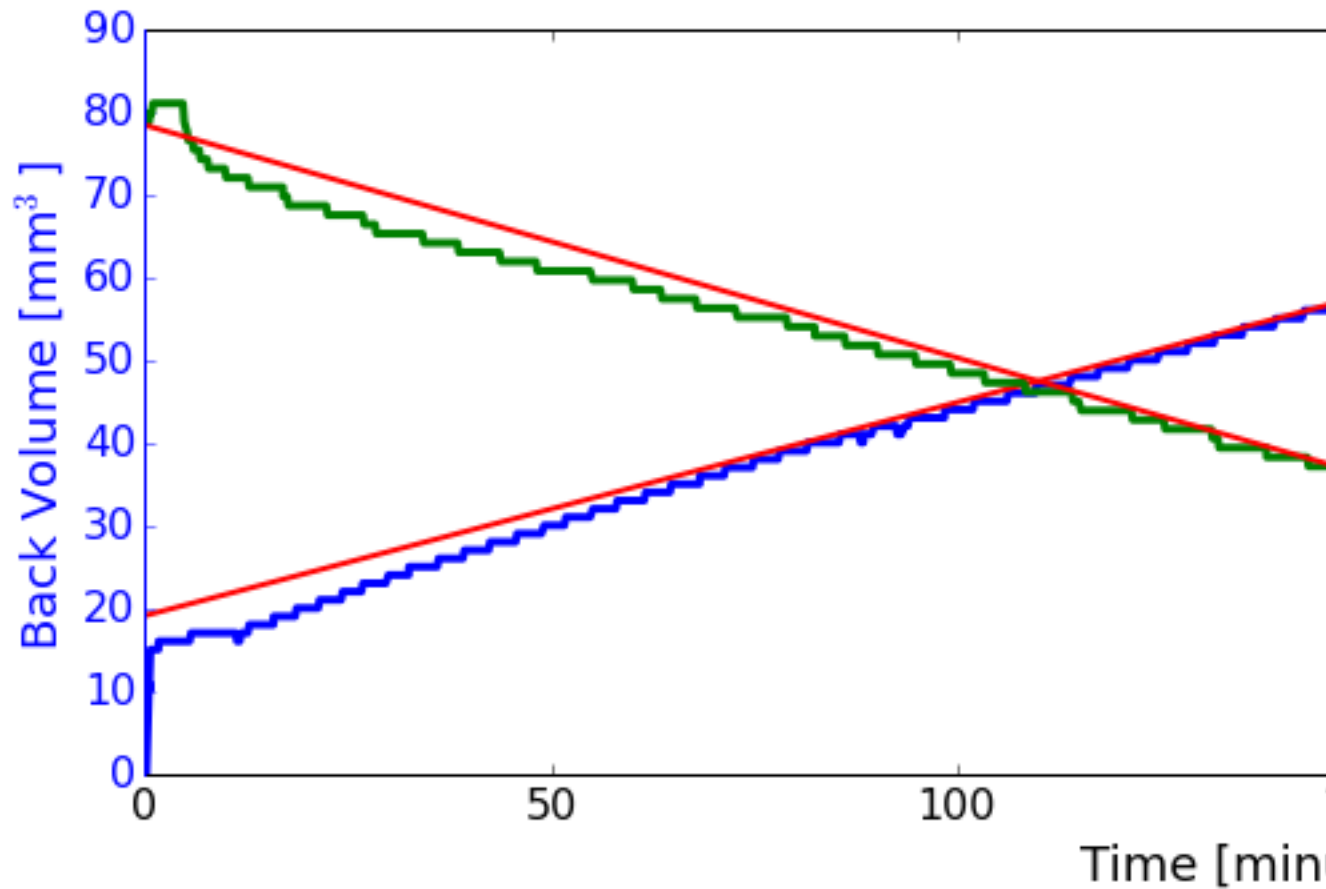


Fig. 4.3. To determine permeability, flow rates from the upstream (blue) and downstream (green) pumps are fit with a least squares fit (red) when the steady-state flow condition is achieved (shaded area). The procedure is repeated at multiple hydraulic heads for repeated permeability measurement.

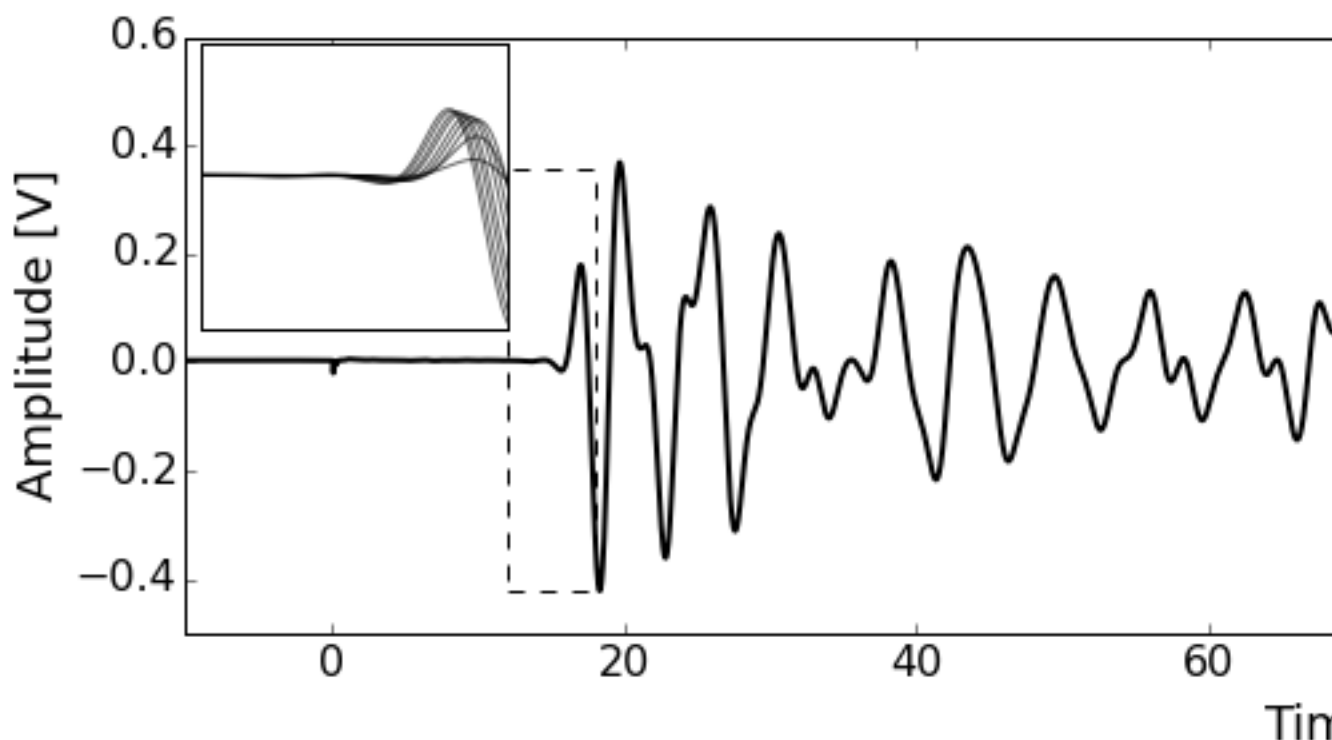
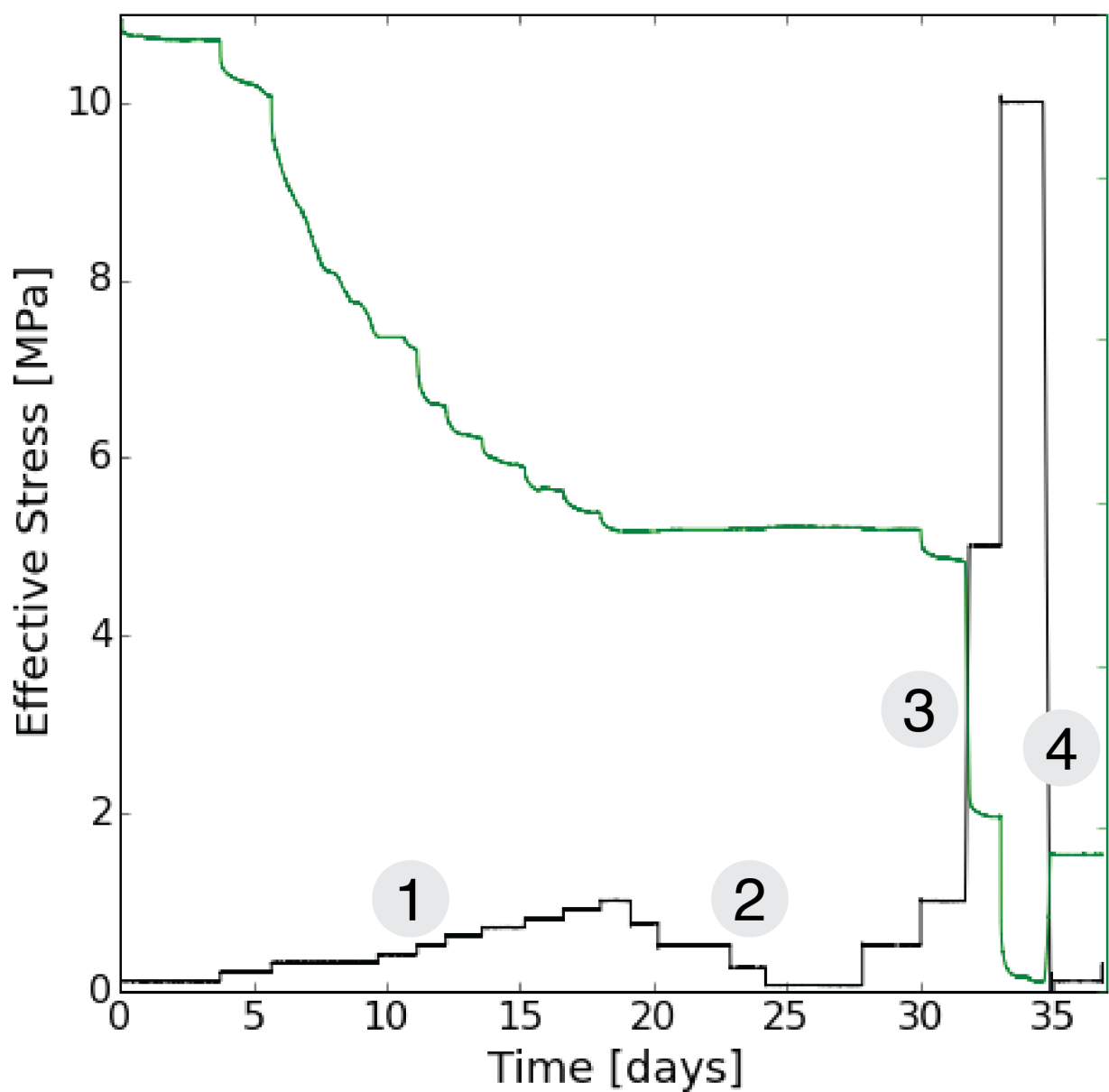
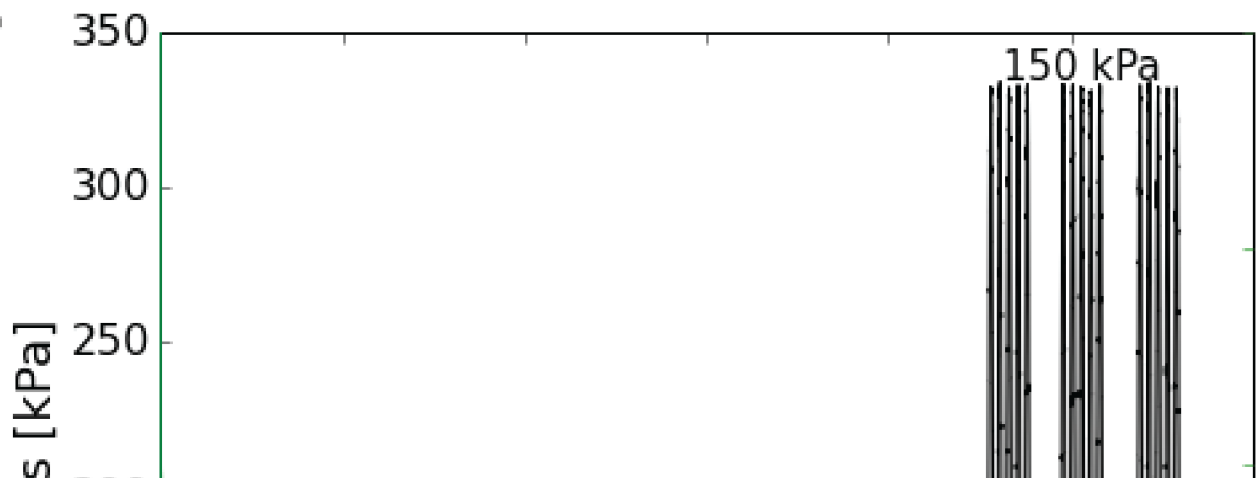
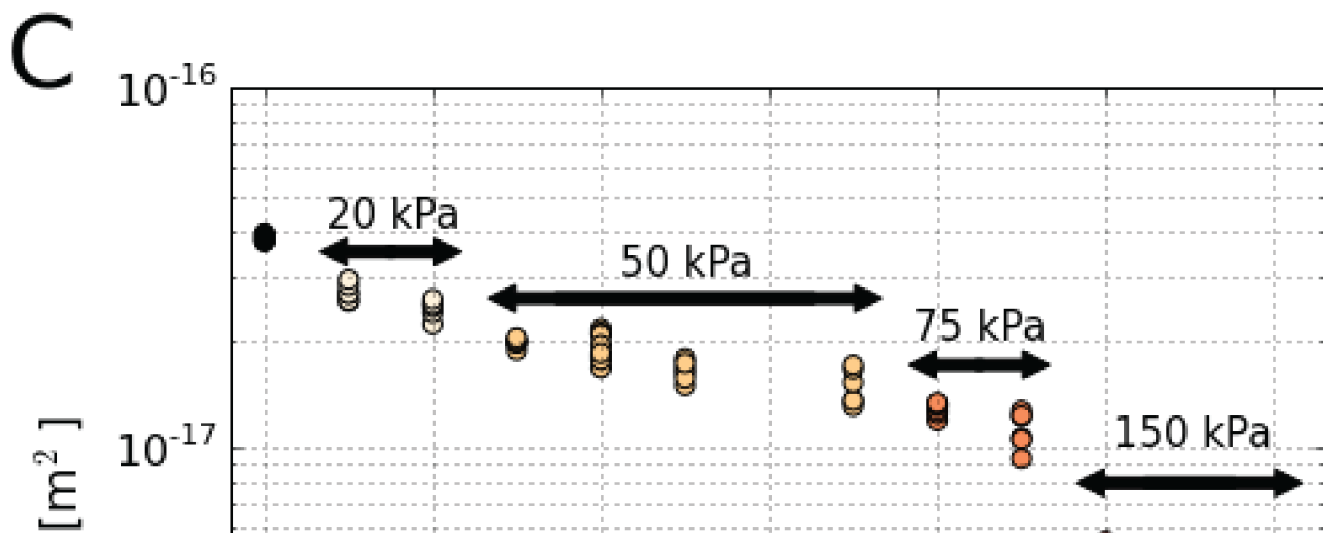
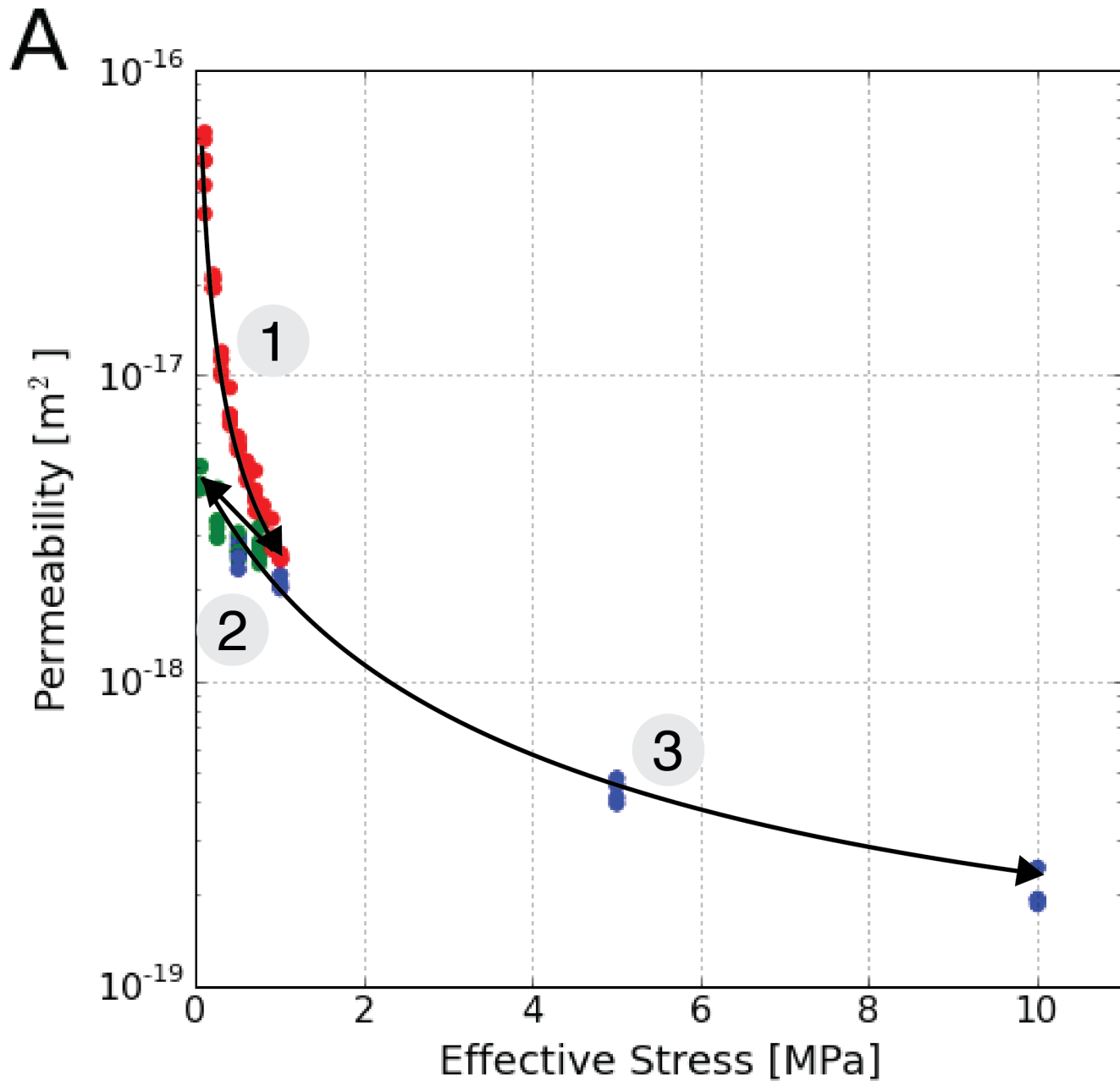


Fig. 4.4. An example acoustic waveform collected during the step-loading test. Inset shows changes in travel time with step loading to 1 MPa effective stress. First arrivals are picked with a cross-correlation technique for consistency.

A**C**



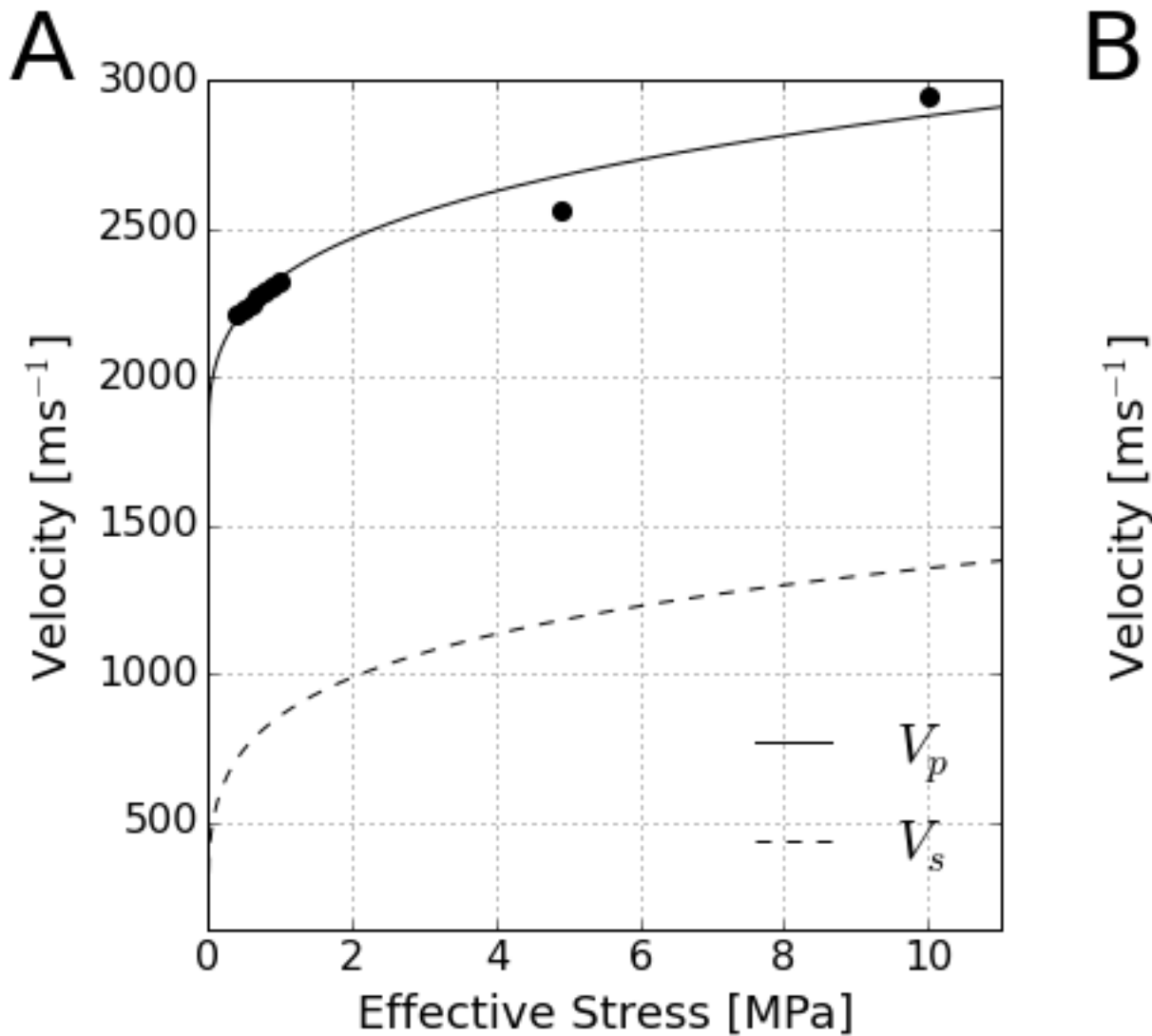


Fig. 4.7. (A) Predicted compressional and shear wave velocities from the effective medium model as a function of effective stress, (B) an expanded view showing field velocity measurements from seismic experiments, and porosity (C). The model is supported by experimental compressional wave velocity measurements, but no shear wave measurements could be obtained in the laboratory due to the very low effective pressures of the experiment. Black circles represent direct measurements from the laboratory, gray bars are velocity estimates by Luthra et al. [2016] and black triangles are estimates by Blankenship et al. [1987].

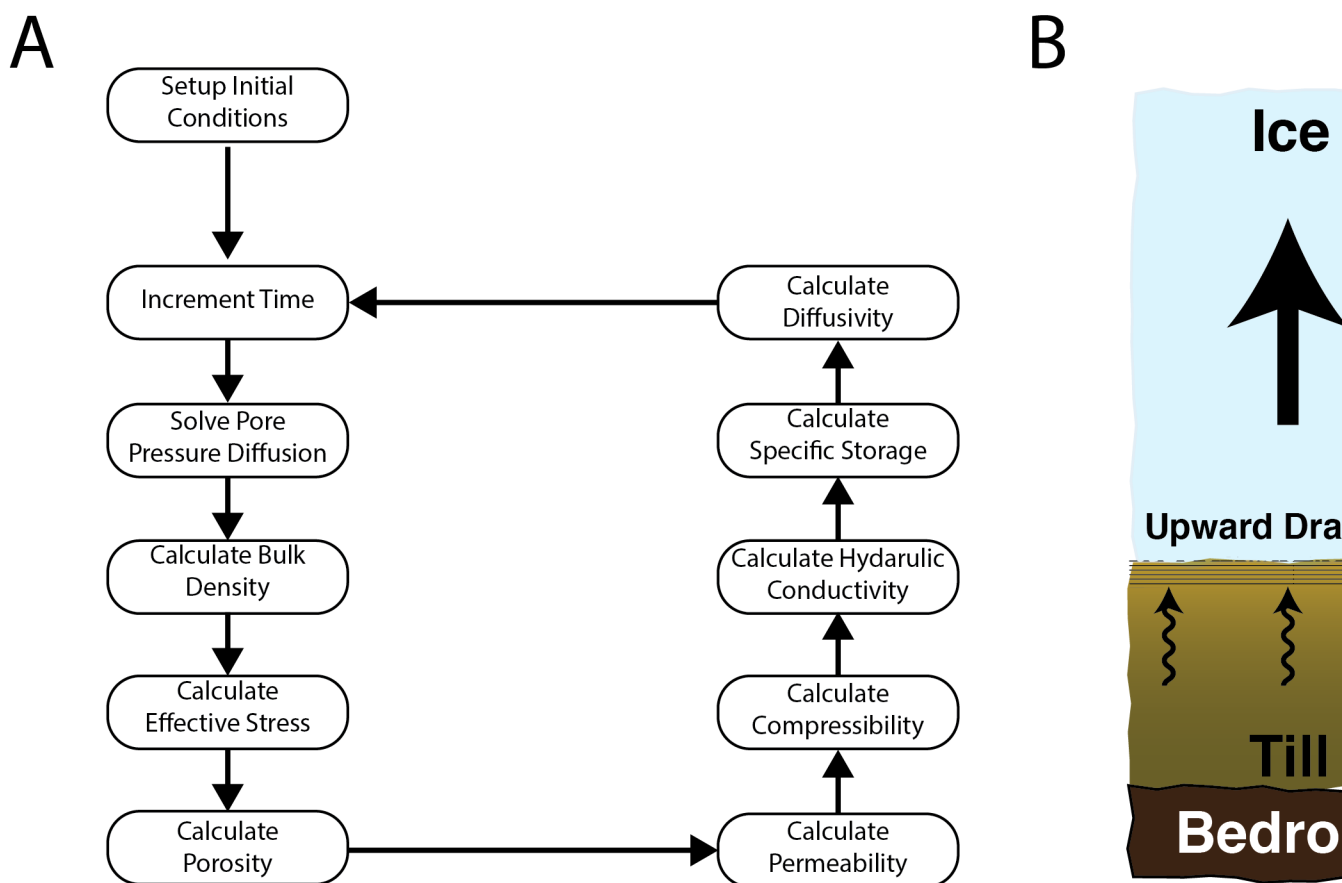


Fig. 4.8. A) Flow chart showing the sequence used when computing the 1-D hydrologic model. B) A cartoon version of the system with ice unloading the till beneath it on a tidal timescale. Upward drainage as a result of lower effective stress at the ice-till interface will quickly result in the formation of a hard layer that slows further drainage and limits the hard layer depth to tens of centimeters. C) Loading from the ice will inject water back into the till as the basal hydraulic pressure is increased.

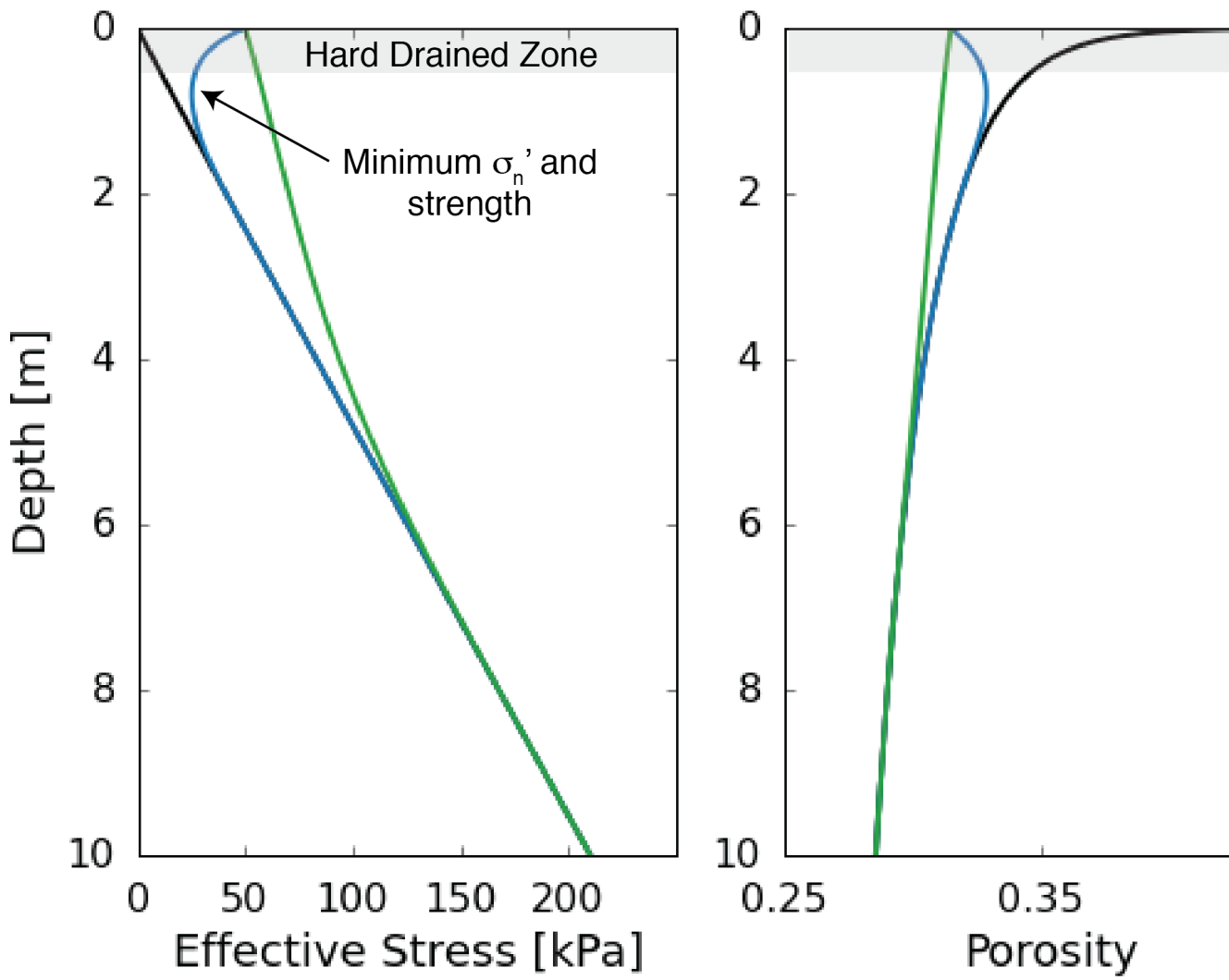


Fig. 4.9. Model results for a coupled diffusion/compaction model of the till layer with an imposed 50 kPa effective stress perturbation at the top boundary. The perturbation can affect the till over several tens of centimeters in a 12 hour tidal time scale. Over a longer perturbation, such as moving over a rough area on the bed, the till can come close to equilibrium in a month.

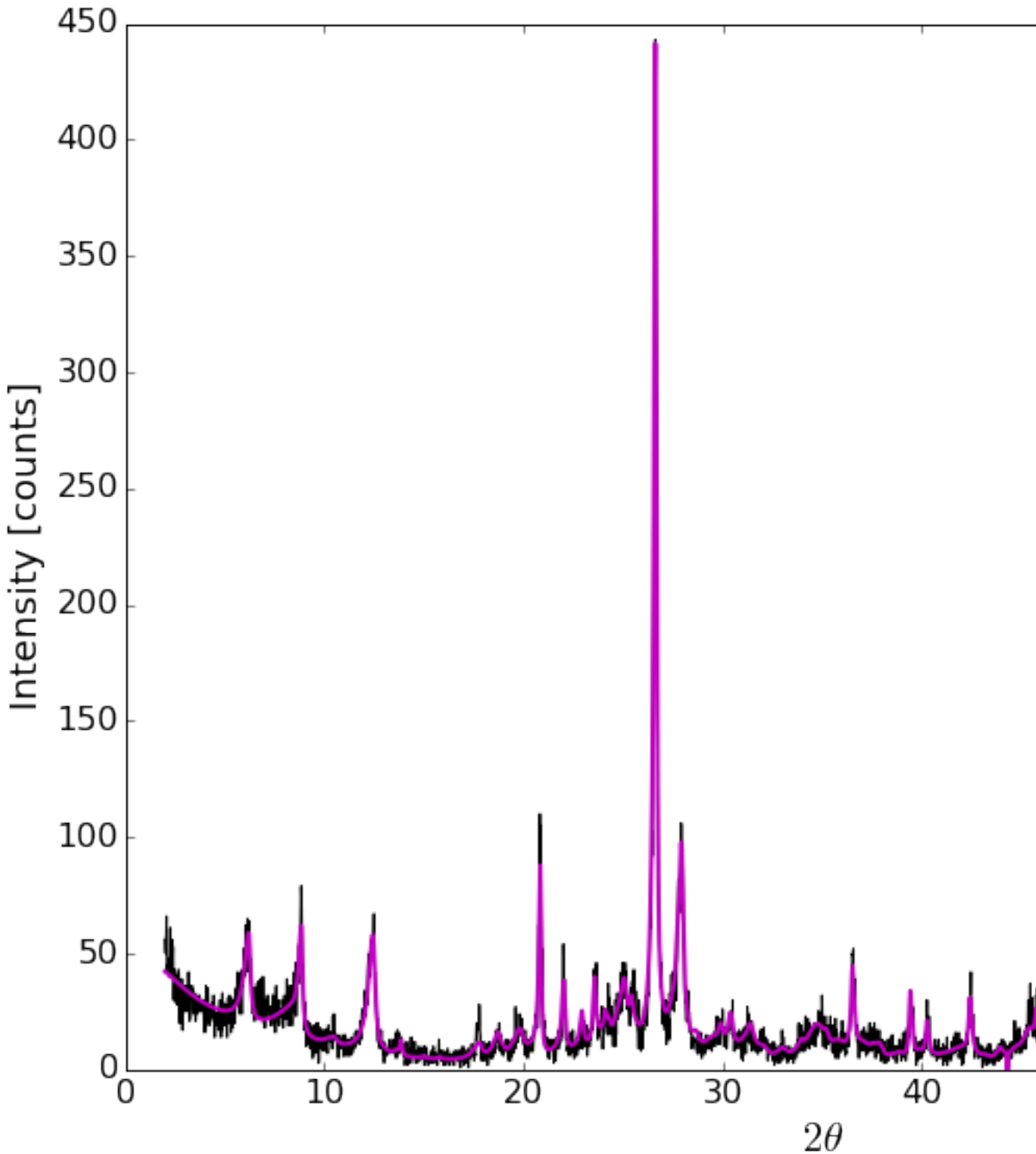


Fig. 4.10. XRD analysis shows very high clay content in the till samples with significant amounts of quartz as well. Some non-uniqueness exists in the type of clays present, but an effort was made to minimize the misfit with reasonable geological constraints.

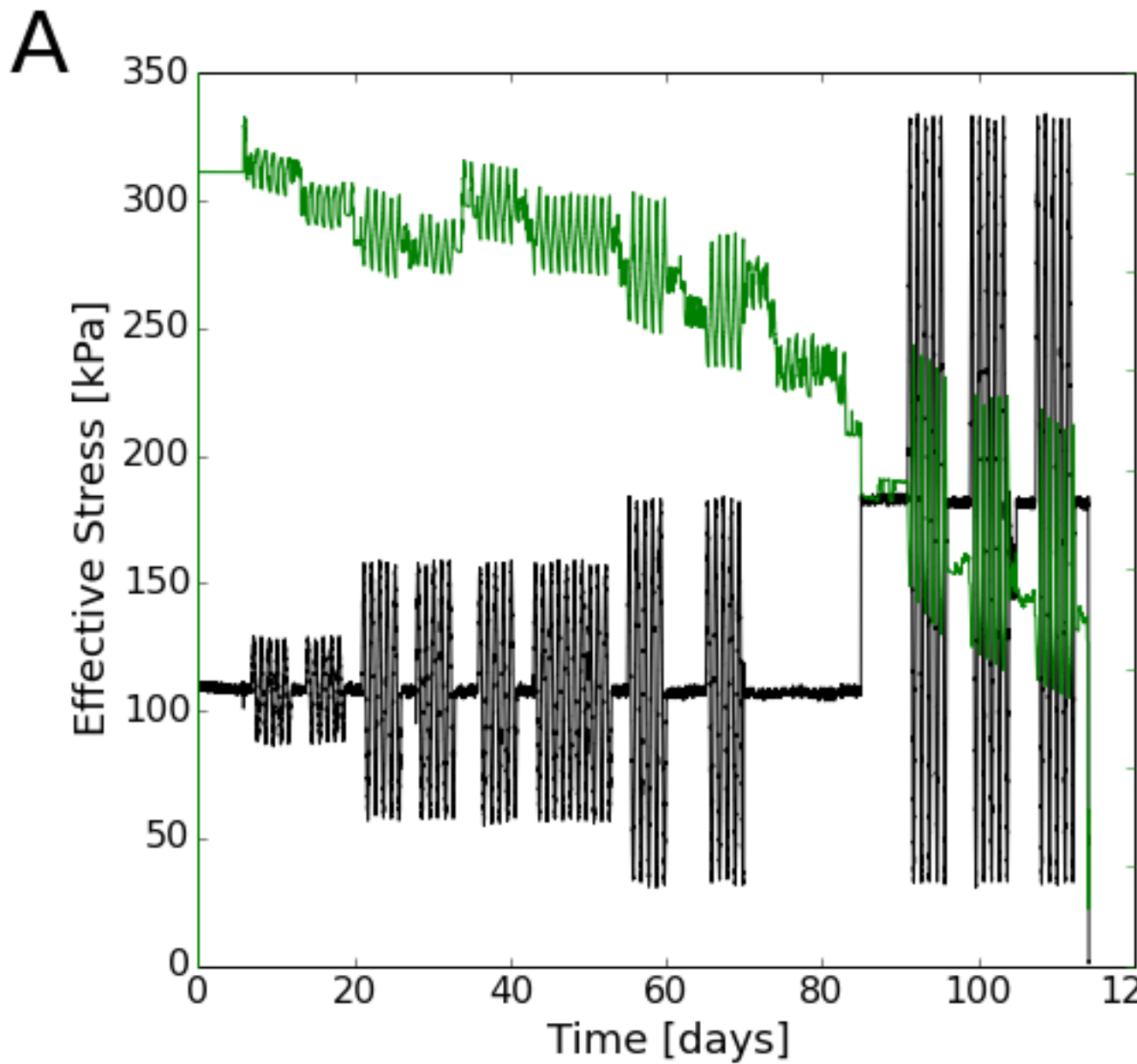


Fig. 4.11. A) Evolution of volumetric strain during repeated tidal load cycling. B) Strain was accumulated during all cycle sets, similar to the axial strain trends, but with some slight anomalies likely induced by thermal effects on pump volume measurements as volume changes are very small.

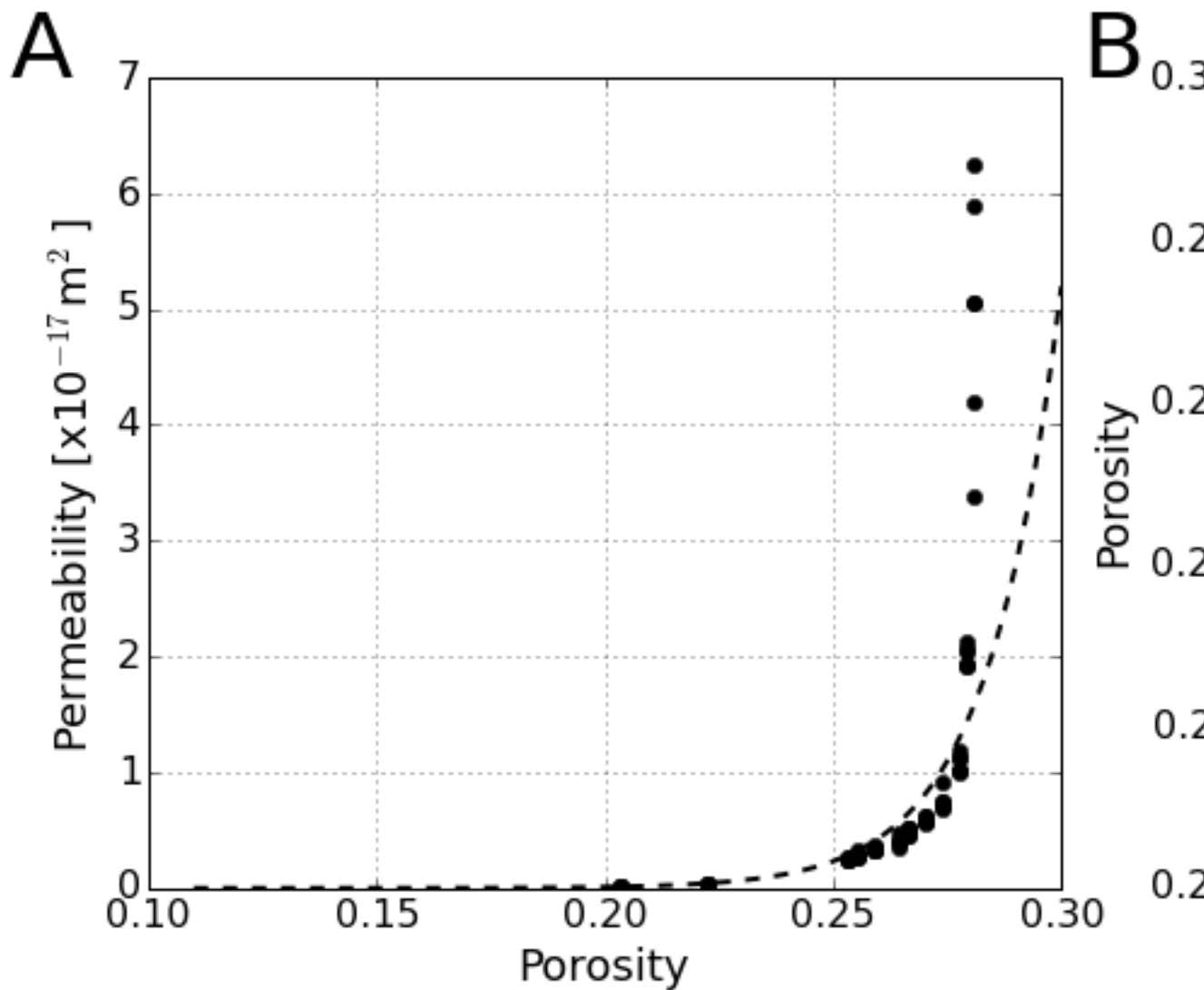


Fig. 4.12. Experimental data and fits used in loading portions of the simple hydrologic model. Porosity-permeability (A) was fit with an exponential, while effective stress - porosity (B) and effective stress - compressibility (C) were fit with logarithmic relationships.

Chapter 5

On the origin and evolution of electrical signals during frictional stick slip in sheared granular material

5.1 Abstract

Electromagnetic signals have been reported in association with geophysical phenomena including earthquakes, landslides, and volcanic events. Mechanisms that suggested to explain seismoelectrical signals include triboelectricity, piezoelectricity, streaming potentials, and the migration of electron holes, yet the origin of such phenomena remains poorly understood. We present results from laboratory experiments regarding the relationship between electrical and mechanical signals for frictional stick-slip events in sheared soda-lime glass bead layers. The results are interpreted in the context of lattice defect migration and granular force chain mechanics. During stick-slip events, we observe two distinct behaviors delineated by the attainment of a frictional stick-slip steady state. During initial shear loading, layers charge during stick-slip events and the potential of the system rises. After steady state stick-slip behavior is attained, the system begins to discharge. Coseismic signals are characterized by potential drops superimposed on a longer-term trend. We suggest that the observed signal is a convolution of two effects: charging of the forcing blocks and signals associated with the stress state of the material. The long-term charging of the blocks is accomplished by grain boundary movement during the initial establishment of force chain networks. Short-term signals associated

with stick-slip events may originate from produced electron holes. Applied to tectonic faults, our results suggest that electrical signals generated during frictional failure may provide a way to monitor stress and the onset of earthquake rupture. Potential changes could produce detectable signals that may forecast the early stages of failure, providing a modest warning of the event.

5.2 Introduction

A number of electromagnetic signals have been observed during tectonic faulting and mechanical failure of rocks, but the mechanisms underlying these phenomena are still unclear. Recently, efforts to couple observations by the physics and materials science communities with observations of natural phenomena in the geoscience community have begun to show promise [Enomoto and Zheng, 1998; Balk et al., 2009; Takeuchi et al., 2010; Freund, 2010; Onuma et al., 2011; Shinbrot et al., 2012]. Existing studies indicate that large earthquakes are, in some cases, preceded or accompanied by ultra low frequency electromagnetic emissions, residual magnetic anomalies, and even visible electrical atmospheric discharges known as ‘earthquake lights’ [Derr, 1973; Park et al., 1993; Uyeda et al., 2009]. Understanding these phenomena may improve our ability to provide early warning of seismic events or other hazardous material failures, and will provide insight into fault zone physical processes and stress conditions during the seismic cycle.

Several mechanisms have been proposed to explain the generation of electrical potentials in Earth, including: piezoelectric effects, streaming potential, contact/tribo electrification, fracto-emission, plasma excitation, and semiconductor-like effects [Finkelstein et al., 1973; Dickinson, 1982; Dickinson et al., 1982; Dickinson, 1984; Freund,

2000; Frid et al., 2000; Jouniaux and Ishido, 2013; Takeuchi and Nagao, 2013]. Even with an assumed mechanism of charging, there are still many mysterious aspects of the phenomenon, including conduction of the charge to the surface, charge residence time, and Earth/atmosphere interaction. Here, we examine electrical potentials observed for sheared granular layers that exhibit regular frictional stick-slip instabilities in the laboratory. We interpret the results of experiments on this fault gouge analog in the context of modern theories of charge separation in geologic materials.

5.3 Previous Work

5.3.1 Natural Occurrences

Light emissions have been reported in association with rock failure during both seismic rupture at Earth's surface (so-called Earthquake lights) and during rock bursts in mines. Earthquake lights have been reported during various stages of the seismic cycle, in addition to other electromagnetic phenomena. Related electrical phenomena believed to be connected with rock failure include ultra low frequency electromagnetic emissions, resistivity variations [Park et al., 1993], and anomalous animal behavior [Kirschvink, 2000]. A summary of these phenomena by Uyeda et al. [2009] and the references therein illustrate the breadth of observations.

The first photographically well-documented sequence of earthquake lights (EQL) occurred during the 1965-1967 Matsushiro earthquake swarm [Derr, 1973]. Earthquake lights were also observed in the M7.2 November 29, 1975 Kalapana earthquake. The M7.2 1995 Kobe earthquake was reported to have EQL as well as observations of burned

plant roots at the rupture site, and natural remanent magnetization (NRM) anomalies [Enomoto and Zheng, 1998]. Anomalous NRM have been measured in pseudotachylite, suggesting that high remanent magnetizations were acquired in a co-seismic electrical process and locked into thin, rapidly cooling layers of melt [Ferré et al., 2005]. Visual electromagnetic phenomena were reported before the M6.3 April 6, 2009 L'Aquila earthquake [Fidani, 2010]. Although reports were confused by astronomical/meteorological events and coseismic power line flashes, a number of unexplained observations remain.

Most reported EQL have been generated on intraplate faults with relatively shallow sources, for magnitude 7 and greater events, and commonly for earthquakes with demonstrated surface rupture. Lockner et al. [1983] suggest that vaporization of water produces a charge separation that is then moved to the surface by a central fluid conductor. Reports of EQL phenomena often include descriptions of the anomalies being most intense at topographic highs, suggesting that surface charge on the ground was concentrated by the topography. EQL may be more common in high stress drop events and/or in association with branching and geometrically complex events [Scholz, 2002].

5.3.2 Previous Experimental Work

Much experimental work has been done to test physical mechanisms that could cause electrical anomalies during seismic activity and rock failure. The most relevant explanations are briefly discussed here, but more in depth discussion may be found in Uyeda et al. [2009], Freund [2000], and references therein.

Early work by Nitsan [1977] investigating piezoelectric effects showed electromagnetic radiation in the 1-10 MHz range during the fracturing of quartz bearing rocks

under uniaxial compression. The idea of the piezoelectric effect causing changes in the electrical field during failure suggested that frequency content of the signal would be related to the rate of stress release. This relationship is supported by a spectral shift to higher frequencies with smaller particles [Nitsan, 1977]. Uniaxial compression studies using cores of Red Texas Granite, Barre Granite, Dakota Sandstone, Carthage Marble, and quartzite exhibited electromagnetic signals peaking below 40 kHz in association with failure. Observed signals also exhibited some degree of directionality [Rowell et al., 1981; Hanson and Rowell, 1982]. Signals peaking at 100 kHz were observed during impact and cratering tests by Bianchi et al. [1984] both in vacuum and at atmospheric pressure.

Mechanisms involving the formation of cold plasmas during fracture and impact have also been proposed to explain charge generation [Martelli and Cerroni, 1985], but have not been investigated thoroughly. Calculations considering a beam-plasma interaction producing an ion-acoustic instability suggest that the expected radiation frequencies are at \sim 50 kHz.

A recent study by Onuma et al. [2011] examined gabbro and quartz powders, used as simulated fault gouge and sheared between gabbro forcing blocks in a saw-cut geometry. Electrical signals in the co-seismic period were detected by direct contact electrodes as well as toroidal induction coils surrounding the sample. In 25% of their experiments, a possible pre-cursory signal was detected, but not consistently on all instruments. Piezoelectricity was ruled out as a dominant mechanism, because signals were observed in piezoelectric and non-piezoelectric gouges and there was no preferred c-axis orientation in the quartz powder. Signals were observed from piezoelectric and non-piezoelectric materials by Cress et al. [1987] as well, but in their experiments on

quartz produced larger signals than other materials. Onuma et al. [2011] did not observe signals during initial loading; however, such signals have been observed by other workers in natural and experimental cases [Takeuchi et al., 2010] who attributed them to frictional electrification because they scaled roughly linearly with slip.

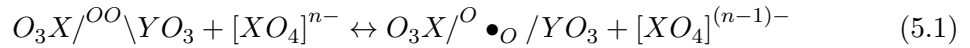
The presence of moving dislocations with respect to propagation of microcracks producing a ‘pressure stimulated current’ in marble samples has been examined [Triantis et al., 2008]. These currents are a result of charge separation during the beginning stages of failure, not during the initial loading stages.

Piezoelectric effects are well-documented in materials such as quartz, but geologic materials are not expected to have the required mineralogy or grain alignment to make this a viable mechanism in nature. Randomly oriented grains would produce a series of randomly oriented dipoles that would cancel to produce a net-neutral field. Streaming potentials and electrokinetic effects [Mizutani et al., 1976] are well-documented, but are generally not of sufficient magnitude to explain the observed phenomena, because large potentials are difficult to maintain with generally conductive fluids present. Electrification by relative surface movement (tribo-electrification) is also well-documented [Pingali et al., 2009; Pähzt et al., 2010], but does little to explain electrical signals produced while contacts are stationary to quasi-stationary.

Evidence for electrical signals during and possibly as precursors to failure in a low stress environment has been collected [Shinbrot et al., 2012] in experiments examining slope failure and crack opening or closing in powdered pharmaceutical materials. An electrostatic voltmeter (ESVM) like that used in this study was used to monitor rotating

and tilting drums of powder as well as flexure of powder layers resulting in opening and closing fissures of the material.

Another model of charge generation during deformation of geomaterials is the ‘semiconductor’ effect. In geologic materials, oxygen is generally considered to exist in the O^{-2} valence state, but the more oxidized form O^- is also present in a pair of coupled O^- atoms known as a peroxy defect. The peroxy link can be broken via mechanical strain such as during passage of a mechanical deformation front in the form of a propagating elastic wave or elastodynamic rupture front. In this case, an electron is sourced in an attempt to satisfy the newly formed electrical imbalance at the site of the broken peroxy bond. This oxidizes the donor, forming a single defect electron (eq.5.1). [Freund, 2000; Freund et al., 2006; Freund, 2010]



Electrons are not free as charge carriers, but holes remain mobile [Freund, 2000; Freund et al., 2006; Freund, 2010; Balk et al., 2009]. The semi-conductor effect has been explored in solids [Takeuchi and Nagao, 2013; St-Laurent et al., 2006], but few studies have been conducted on granular materials, which are likely to be important in the behavior of tectonic fault zones.

5.4 Methods

We conducted experiments on granular layers used to simulate fault gouge under controlled boundary conditions, with concurrent measurement of electrical potential,

stresses, and strains of the layer to explore the relationship between stress state and the evolution of electrical signals. We used glass beads to represent granular fault gouge because they exhibit repeated frictional stick-slip behavior and share key friction constitutive properties with rock. The main advantage of this choice lies in the reproducibility of stick-slip behavior, allowing investigation and isolation of the processes that cause electrical signals relevant to natural faults containing granular gouge by using a simple, well-characterized system. We note that glass should contain fewer starting defects than silicate minerals found in natural fault gouges, such that any effects observed in our glass bead experiments would likely be amplified in natural materials.

5.4.1 Apparatus

All experiments were conducted on a biaxial deformation machine with a servo-hydraulic control system [Karner and Marone, 2000; Frye and Marone, 2002]. Hydraulic servo valves are operated in either displacement or force feedback modes through a series of analog amplifiers and comparators. Control displacement signals are generated by a 16-bit digital to analog converter capable of $\pm 5\text{V}$ range. The apparatus (Figure 5.1A) is capable of 1 MN of force on the horizontal ram and 1.5 MN on the vertical ram. Ram velocity can be controlled to $0.1 \mu\text{m/s}$ in displacement mode, or to about 10N in load mode [Hong and Marone, 2005; Rathbun et al., 2008].

We used forcing blocks of cast acrylic with a dielectric strength of 15-17 V/ μm and a tensile strength of 55-77 MPa. Forcing blocks were cut to size and machined with grooves 1 mm deep and 2 mm wide perpendicular to the shearing direction to ensure that shear occurred within the layer and not at the layer boundary [Anthony and Marone,

2005; Knuth and Marone, 2007]. Acrylic side shields were also made to confine the sample material. The nominal frictional contact area was 10 cm x 10 cm.

Force was measured using Beryllium-Copper strain gauge load cells built in-house and placed in series with the loading ram and sample. The load cells and the wheat-stone bridge electronics are calibrated regularly with a proving ring traceable to the National Bureau of Standards. Displacement is measured with direct current displacement transducers (DCDTs) affixed to the ram nose and referenced to the end platens of the hydraulic rams. Positions of both classes of instrumentation are noted in Figure 5.1A.

We recorded data using a 24-bit, 16-channel simultaneous, delta-sigma style analog to digital system. Samples are collected at 10 kHz and averaged to the desired rate from 1 Hz to 10 kHz as necessary to maintain the appropriate signal-to-noise ratio. Recording rates may be changed during the experiment, and our tests show minimal cross-talk or dwell errors in this system.

5.4.2 Sample Material & Preparation

Samples were built in the double direct shear configuration (Figure 5.1B) using soda-lime glass beads [Anthony and Marone, 2005]. Two layers of beads were confined in a three forcing block assembly with a rubber membrane at the bottom and side-shields on the boundaries to avoid lateral extrusion of the material. The top of the sample was unconfined.

Layers were built by placing the side forcing blocks on a leveling jig and applying cellophane tape around the perimeter. The tape was then trimmed to the desired height

to produce uniform, reproducible layers. We used 5 mm thick layers for all experiments in this study (Table 1). Sample material was poured into the form, lightly compacted, and leveled. The center forcing block was affixed to one side block (and the sample) with additional cellophane tape, securing the blocks and gouge layer and providing enough strength to allow transport of the sample from the bench to the deformation apparatus. The process is repeated for the second layer.

We constructed layers using Class IV soda lime glass spheres (product GL0191B4/106-150) from Mo-Sci Specialty Products in Rolla, Missouri (composition shown in Table 5.2). Two mono-disperse size distributions were tested: 100-150 μm and 420-500 μm . Scanning electron microscopy (SEM) analysis of the beads shows that they are homogeneous, with few exceptions, and smooth (Figure 5.2). Past work has shown that bead comminution is minimal until $\sigma_n > 10 \text{ MPa}$ [Mair et al., 2002; Mair and Abe, 2011].

5.4.3 Potential Measurement

Electrical potential on the layers was measured by a model 344 electrostatic non-contact volt meter (ESVM) manufactured by Trek Inc. This instrument reported the potential with respect to system ground sensed in its field of view. An analog output of the measured voltage was divided by 100 to provide a sensing range of $\pm 2 \text{ kV}$ with a $\pm 20 \text{ VDC}$ output signal recorded. A ‘response’ setting on the instrument controlled internal damping constants.

The sensor head contains two electromechanically oscillated plates. Plates are fixed parallel to each other with the surface normal facing the surface under test. The front plate is affixed to the instrument body and has a small aperture in the center.

The rear plate is inside the instrument and is the oscillating plate. The sensor operates by varying the voltage across the plates and sensing the alternating current (AC) signal resulting from the movement of the plates with respect to one another. When the AC component of the signal is nulled, the voltage across the plates exactly matches the voltage on the surface under test. This sensor configuration has several advantages: 1) no contact is required with the surface under test, which is excellent for systems where coupling is a challenge, 2) there is no arcing risk since the instrument and surface under test are at the same potential, and 3) the sensor is easily portable, allowing tests with different viewing positions.

Two different sensor geometries were used: side view and top view (Figure 5.1C). In the top view, all tape between the sensor and the sample was removed. In the side view, a notch was cut in the side shield, leaving only a thin layer of tape (necessary to prevent extrusion) for the sensor to observe through. In our calibrations, we found that the sensor operates normally when viewing signals through thin obstacles.

5.4.4 Experimental Procedure

Samples were placed into the testing machine and normal load of 4 MPa was applied and maintained to compact the layers. The shear load was then applied by driving the vertical ram at a constant displacement rate (1, 30, or 100 $\mu m/s$). Electrical potential was recorded by placing the sensor in either the top or side view geometry with a distance of ~ 1 cm between the front of the sensor and the gouge layer. The response setting was set to the maximum value of 9.

We conducted experiments at room (ambient) humidity, at 100% relative humidity (RH), and under submerged conditions using de-aired water. 100% RH was achieved by placing the sample assembly in a plastic membrane with a beaker of anhydrous sodium carbonate solution (2:1 ratio with distilled water) within the membrane. This exothermic reaction produced a 100% RH environment in the membrane. For all experiments under controlled humidity, samples were left to equilibrate overnight with a small normal stress applied by a hand-clamp, and then placed in the testing machine. When the experiment began, we refreshed the anhydrous sodium carbonate solution, applied the normal stress and proceeded with our standard loading protocol. For these experiments, we cut a small window in the humidity-control membrane to provide access for the sensor. A capacitive sensor hygrometer (Lifft C200 with a maximum error of $\pm 3\%$) verified that the relative humidity never fell below 100%. Saturated experiments were performed in a similar manner, but the membrane was filled with distilled water and the sample allowed to saturate as load was applied. The water level just covered the top of the blocks and a top-view ESVM geometry was employed.

5.4.5 Calibration and Control Tests

We performed tests to ensure calibration of the ESVM, as well as to evaluate the sensitivity of the response control. The ESVM probe was affixed to an electrically insulating base and placed approximately 1 cm from an aluminum plate. The plate was charged with a precision DC power supply (HP 6216B) and the true and measured plate voltages recorded. Performance was further evaluated by attaching the surface under

test to a function generator. Square waves were measured on each response setting (1-9) to evaluate ringing of the instrument (Appendix A).

In addition, an experiment identical to those testing electrical potential on the layers was performed with the ESVM pointed away from the load frames into the room and towards a DC charged aluminum plate. This test was performed to ensure that the signals we observed during shearing were not from electrical interference of the hydraulic control electronics or measurement/recording electronics. We note that our records include motion of the vertical hydraulic ram when it was not in contact with the sample, and no change in voltage was seen. This further indicates that no DC offsets or interference were experienced by the ESVM from the testing machine and/or control electronics and transducers.

All calibration and control tests were conducted with identical analog to digital conversion hardware as the experiments. ESVM calibration tests were also conducted on an independent logger (the LabJack U6) to ensure there was consistent performance and minimal measurement burden from either system.

5.4.6 Data Analysis

Changes in electrical voltage during stick-slip events were picked by hand to evaluate the electrical signal. ESVM data are more noisy than the mechanical data and electrical anomalies are not found with every stick-slip event, making manual picking the most accurate. Measured electrical potential and shear stress were plotted on the same x-axis and mouse position clicks were recorded. Interpretation was aided by superposition of a smoothed potential signal. The potential was smoothed using a Savitzky

Golay filter [Savitzky and Golay, 1964], as it preserves peaks, but decreases noise. With the Savitzky Golay filter, a line of specified low-order is fit to a certain data window using a linear least squares technique. The analysis is then stepped forward and fit signals convolved.

Data were recorded in a binary form, decoded, converted from bits to engineering units through use of calibrations derived from our transfer standards, and then written out as either a binary or ASCII for analysis. The Python environment was used for processing and analysis. All stick-slip events were automatically picked by first computing the smoothed derivative of shear stress with respect to time using a running-average slope tool. Zero-crossings of the derivative indicate a slope change from positive (like that during load up) to negative (like that during failure) or the reverse. The automatically determined stress drops were checked against a threshold value to ensure that no noise was picked as events. Automatic picks were visually inspected to ensure algorithm performance.

5.5 Results

5.5.1 Mechanical Data

The application of shear load resulted in a characteristic linear-elastic stress-displacement record during initial run-in (Figure 5.3). Stick-slip behavior began as we reached the failure strength of the material. As shear load increased during the stick-slip cycle, the material began to creep and deform elasto-plastically, as indicated by deviation of the stress-strain curve from the initial, linear-elastic trend. When the ultimate

strength of the layer was reached, layers failed and a stress drop was observed. We define the stress drop as the magnitude of shear stress change during stick-slip failure. In a series of repeating events, we define the recurrence time as the time between peak stresses of two slip events. For a summary of this terminology see Figure 5.3 inset. Mechanical steady-state (not to be confused with steady-state frictional sliding) refers to the system state after the initial run-in period, defined as the point at which stress drops in repeated stick-slip events become constant.

All experiments exhibited a maximum coefficient of friction during mechanical steady-state ($\mu \equiv \tau/\sigma_n$) of 0.3-0.4. For experiments at 100% humidity or water saturated, we observed an increased stress drop and ultimate strength due to the activation of chemo-mechanical mechanisms such as solution-reprecipitation [Frye and Marone, 2002; Yasuhara, 2005; Scuderi et al., 2013].

The recurrence time between events has been shown to vary with load point velocity [Karner and Marone, 2000; Beeler et al., 2001]. We observe a power law relation between load point velocity and recurrence time with a characteristic slope of -1.14 (Figure 5.4A). For faster load point velocities, there is less time for contact healing to occur before the layer fails, resulting in lower maximum stresses and shorter recurrence times. Shorter healing times also result in smaller stress drops, which produce a correlation between longer recurrence times and larger stress drops (Figure 5.4B).

Experiments performed using the 420-500 μm glass beads exhibited repeated stick-slip behavior and a lower coefficient of friction of $\sim 0.2 - 0.3$. The occurrence of stick-slip events was less regular than that of the 100-150 μm experiments, as there were five times fewer beads spanning the same 5 mm layer thickness. For the larger

beads, we conducted experiments only at $30 \mu\text{m}/\text{s}$ and we did not explore the role of loading velocity. Due to the large stresses applied to the acrylic forcing blocks by the large beads, some chipping of the grooves was observed, so no further experiments were conducted.

5.5.2 Electrical Data

During shearing we observe two common signals in the electrical potential. The first is characterized by a long period signal (lasting for the entire experiment) that is a general charging/discharging trend (Figure 5.5). The magnitude of this varies between experiments, but can be as much as 250 V. The second is characterized by signals that are of smaller magnitude and shorter duration. These are superimposed on the long-term trend, and are synchronous with individual stick-slip events. The polarity of these events (co-seismic charging or discharging) varies systematically during an individual experiment. During the initial charging stage of the experiment, prior to reaching mechanical steady-state sliding, the anomalies are generally positive. During the phase of overall discharging, the electrical anomalies coincident with stick-slip are generally negative. There are occasional events of unexpected polarity, but there is a strong polarity preference based on the stage of the long-term trend. We consistently observed that the long-term charging/discharging trends were marked by the attainment of mechanical steady-state (Figure 5.5).

After reaching mechanical steady-state, the electrical anomalies associated with each stick-slip event varied systematically with loading velocity (Figure 5.6). For experiments subject to loading at $1 \mu\text{m}/\text{s}$, voltage increased by 1-2 V during shear loading

between stick-slip events and then dropped rapidly during co-seismic failure. Similar behavior was observed at $30 \mu\text{m}/\text{s}$, where voltage changes were 2-4 V. For shearing at $100 \mu\text{m}/\text{s}$ we found a change of electro-mechanical behavior. Initial loading still produced an increase of electrical potential, but during co-seismic slip the potential spiked by tens of volts with the peak occurring just after the stress drop.

We found that the magnitude of potential change during stick-slip events follows a power law relationship with sliding velocity, resulting in an increase of about 5x in voltage for the range of velocities we explored (Figure 5.7). For experiments at 100% RH (saturated) and submerged boundary conditions there was no regular electrical signal associated with the stick-slip events. Minor long-term charging/discharging trends were observed in some experiments.

Electrical anomalies were also observed in the three experiments run with larger ($420\text{-}500 \mu\text{m}$) grain-size material. The anomalies were of similar nature and magnitude to those observed under identical conditions with the smaller grain-size material.

5.6 Discussion

One likely explanation for the electrical signals we observed during stick-slip events involves force chains and their role in the mechanical behavior of granular layers [Majmudar and Behringer, 2005]. Our experiments had no preferred c-axis orientation of piezoelectric grains, ruling out the piezoelectric effect as a main contributor to the observed potentials. Likewise, vaporization of porewater cannot explain our data, because we observe co-seismic signals in low humidity conditions. Streaming potentials are likewise not a major contributor in this configuration. Zeta potentials near individual grains

are insufficient to explain the net external voltage we observed, and would be expected to increase in the saturated and submerged conditions. The plasma model is not applicable to our conditions of low shear velocity and non-fracture experiments. Semi-conductor effects and tribo/contact electrification are two possible mechanisms operating in our experiments; each has the capability to create a potential gradient within the sheared granular samples. Broadly, semi-conductor effects are stress-dependent mechanisms and triboelectric effects are displacement dependent phenomena.

We note that cellophane tape was used in our experiments and that it is electrically active [Camara et al., 2008]. However, based on our calibrations and from tests with no tape, we believe this is not responsible for the signals we observe. Elastic strains in the forcing blocks, where the tape is attached are low and signals are observed when the system is stationary to quasi-stationary during elastic loading. Also, the observed change of sign, from charging to discharging is not consistent with signals from a single mechanism (tape peeling). Finally, we also observed very similar signals from a top-viewing geometry with no tape between the sensor and the layer.

Our experiments consider a fault zone on the order of 10 cm in length. This presents a potential challenge in upscaling our observations to natural fault zones. Additionally, the electrical potentials generated in our experiments are much smaller than those required to explain most field observations, and our measurements were conducted with direct access to the fault zone. One possible explanation is the low number of defects likely to be present in industrially produced glass versus natural silicate minerals.

5.6.1 Electro-Mechanical Model

We hypothesize that the shear load across our granular layers is supported primarily by a small percentage of grains that form layer-spanning chains of highly stressed particles. Granular force chains produce a ‘fragile’ configuration and are separated by regions of spectator grains that support little to no load [Sammis et al., 1987; Liu et al., 1995; Liu and Nagel, 1998; Cates et al., 1998; Boettcher, 1999; Albert et al., 2001; Aharonov and Sparks, 1999].

The observation that the overall electrical signal consists of two parts, charging and discharging, suggests that two mechanisms may be responsible for our observations. The long-term charging trend ceases at approximately the same time as the system reaches mechanical steady-state, suggesting a dependence on the mechanical evolution of the layers. During the initial load up of the system there is large-scale grain rearrangement as force chain networks form and the layers compact. This grain rearrangement involves enhanced grain boundary sliding that can triboelectrically charge the system (Figure 5.8A). The acrylic forcing blocks will hold surface charge, but the charge will slowly drain through various sinks, including contact with the metal loading platens. After a mature force chain network is formed, interparticle movement and grain boundary sliding at the forcing block interface are minimal, which would reduce charging of the forcing blocks. We posit that at this point the rate of discharge becomes equal to or greater than the rate of triboelectric charging, resulting in long-term discharging.

After the system reaches mechanical steady-state behavior, we expect a network of force chains to support the load during the loading portion of the stick-slip cycle. Grains

involved in supporting the load experience much higher local stresses than the spectator grains or the bulk stress measured on the layer. Any electron defects in the highly stressed grains will migrate to less stressed grains adjacent to the force chain. Grains involved in a force chain will be at a lower potential (thus serving as acting anodes) than the spectator grains that are now enriched in positive charge carriers (thus, acting as cathodes). This would result in the net measurement of a positive potential that increases with the shear load (Figure 5.8B).

When the force chain network can no longer support the applied load, the chains fail, resulting in stick-slip and returning the grains (temporarily) to a more homogeneous stress state. The resulting return current redistributes the potential, producing the observed net drop of potential on the layer during stick-slip failure (Figure 5.8C).

The nature of the sharp positive potential spikes just after co-seismic slip in the $100 \mu\text{m}/\text{s}$ driving velocity case remains unexplained by our conceptual model, but the coincidence of the spike with the time during which grains are moving suggests a dominating tribo-electric mechanism at high load point velocities.

Co-seismic charging events observed during the initial loading and first few stick-slips of the experiments appear to be related to the attainment of mechanical steady-state. As the force gradient driving the electrical potential is released during the co-seismic slip, it is possible that instead of neutralizing the charge on layers that the charge follows a second electromotive gradient to the initially lower potential side blocks. This results in an increase in the net potential to ground in the viewing area of the instrument. It is also possible that the rapid charging is a result of triboelectric effects with boundaries during grain rearrangement as the slip occurs before the force chain

network is established. The lack of co-seismic charging events during the bulk system discharging phase after steady-state supports the latter hypothesis.

We note that the 100% RH experiments and the experiments where layers were submerged produced no consistent electrical signals. These experiments showed hints of the long-term potential variations, similar to the charging and discharging trends observed in ambient humidity experiments, but never over 50 V during the course of an experiment. In such moist environments, where conductivity is expected to be high, electrical potential gradients are difficult to maintain without a significant forcing mechanism. The high mobility of electrons in water would allow charge to move; in contrast, holes are not easily mobile in water, further reducing the potential gradient [Balk et al., 2009].

5.7 Conclusions

We show that reproducible electrical potential anomalies can be observed during laboratory shear experiments and are associated with repeated stick-slip failure events. The test material of soda-lime beads allows a well-controlled study, and is geologically relevant to faults containing granular gouge. We propose that our observations may be explained by a combination of the semiconductor effect, triboelectric charging, and a force chain model of loading in granular materials.

The results of this study suggest that small precursory stress drops (foreshocks) in nature may produce electromagnetic signals that could be used as an early warning mechanism for large earthquakes. Such signals would provide more warning than current methods, even if associated with the main shock because of their velocity of propagation.

Even in rock, the electromagnetic signal produced by a time-variant electrical field would propagate at many times the elastic p-wave velocity, producing seconds of warning for observers sufficiently far away. Our research may also find application in mines with relation to wall and column failure, and in slope failure research. In those cases, an understanding of the electrical signals produced could lead to the design of optimum receiver location and improved processing methods, which would increase warning time of natural disasters.

We note that questions about charge conduction to the surface in earthquake faulting, upscaling of laboratory experiments, and the nature of the charge release through the Earth/atmosphere system, remain unexplained. Complex resistivity and the frequency dependence of resistivity are likely important in natural systems. Further investigations of the natural observations and of how chemistry of the material and pore waters influences charge generation are necessary. Similarities in fault zones with reported observations may provide clues, but such observations are rare and generally poorly instrumented. Establishing small sensor networks of visual, spectral, and electromagnetic instruments is crucial to documenting the phenomena and beginning to understand its potential for early warning.

Future experiments will attempt to measure the flow of electrons to and from system ground required to hold the entire system at zero potential in contrast to the presented experiments, in which we isolated the system and measured the resulting potential. This technique allows conductive forcing blocks to be used, making contact with the entire layer and eliminating charging concerns. Spectral characterization of the electrical signals may also provide further insight into the charging mechanism.

5.8 ESVM Calibration

The electrostatic volt meter (ESVM) from Trek is a relatively new method of non-contact surface potential measurement and has not been applied in rock mechanics studies before. To gain confidence in the instrument, a series of tests were conducted by mounting the instrument to a set of non-conductive granite blocks with an adhesive backed paper tape as a bench-top jig. An aluminum plate of 5 cm diameter was placed 1 cm from the aperture of the probe (which has a viewing area of approximately 1:5 according to the manufacturer).

Constant DC voltages, stepped DC patterns, and a square wave pattern were utilized to check the response time of the instrument, calibrate the use of the ‘response’ setting, and to ensure there was negligible cross-talk between channels on the analog to digital converter. The input signal (true) to the plate was recorded simultaneously with the ESVM measured voltage for each of the 9 ‘response’ settings (Figure 5.9). DC offsets during this calibration come from changing the setting on the instrument. For all settings the power was not cycled and the instrument probe remained stationary.

Recorded waveforms at low response show smoothing of the sharp edges of the square wave. High response waveforms do not exhibit smoothing or ringing, but in both cases the waveform rapidly reaches the correct voltage (Figure 5.10). High response waveform recordings are more noisy, but share the mean of the smoothed waveforms. All waveform leading/falling edges corresponded well with changes in the input signal in the time domain (Figure 5.11).

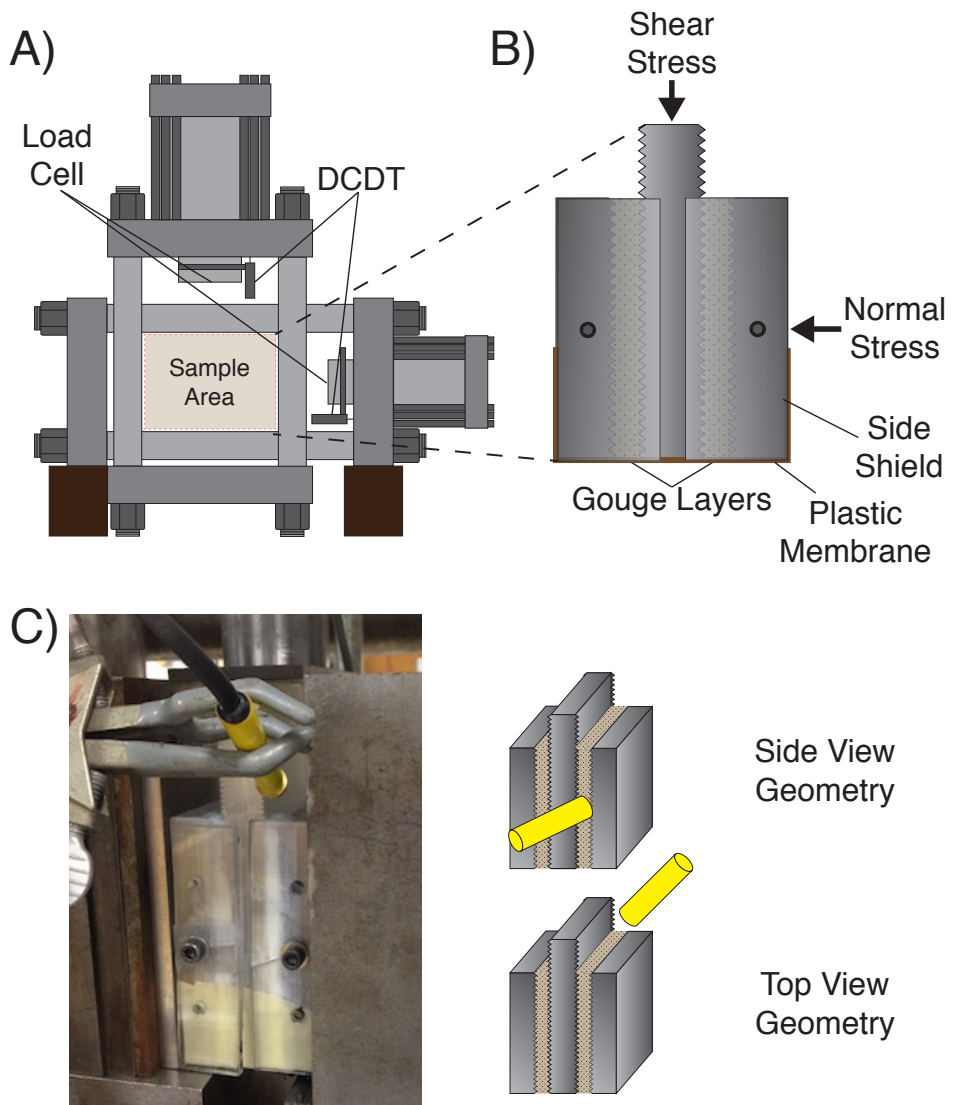


Fig. 5.1. Experimental setup. A) The biaxial hydraulic press: sample assemblies are supported by steel blocks in the sample area. B) Double direct shear geometry consists of two layers of gouge confined between three forcing blocks. Side shields and a plastic membrane are used to contain gouge material as the sample is sheared. C) Placement of the electrostatic voltmeter (yellow cylinder) in the side and top view positions. A window was cut into the side shield for the side view geometry.

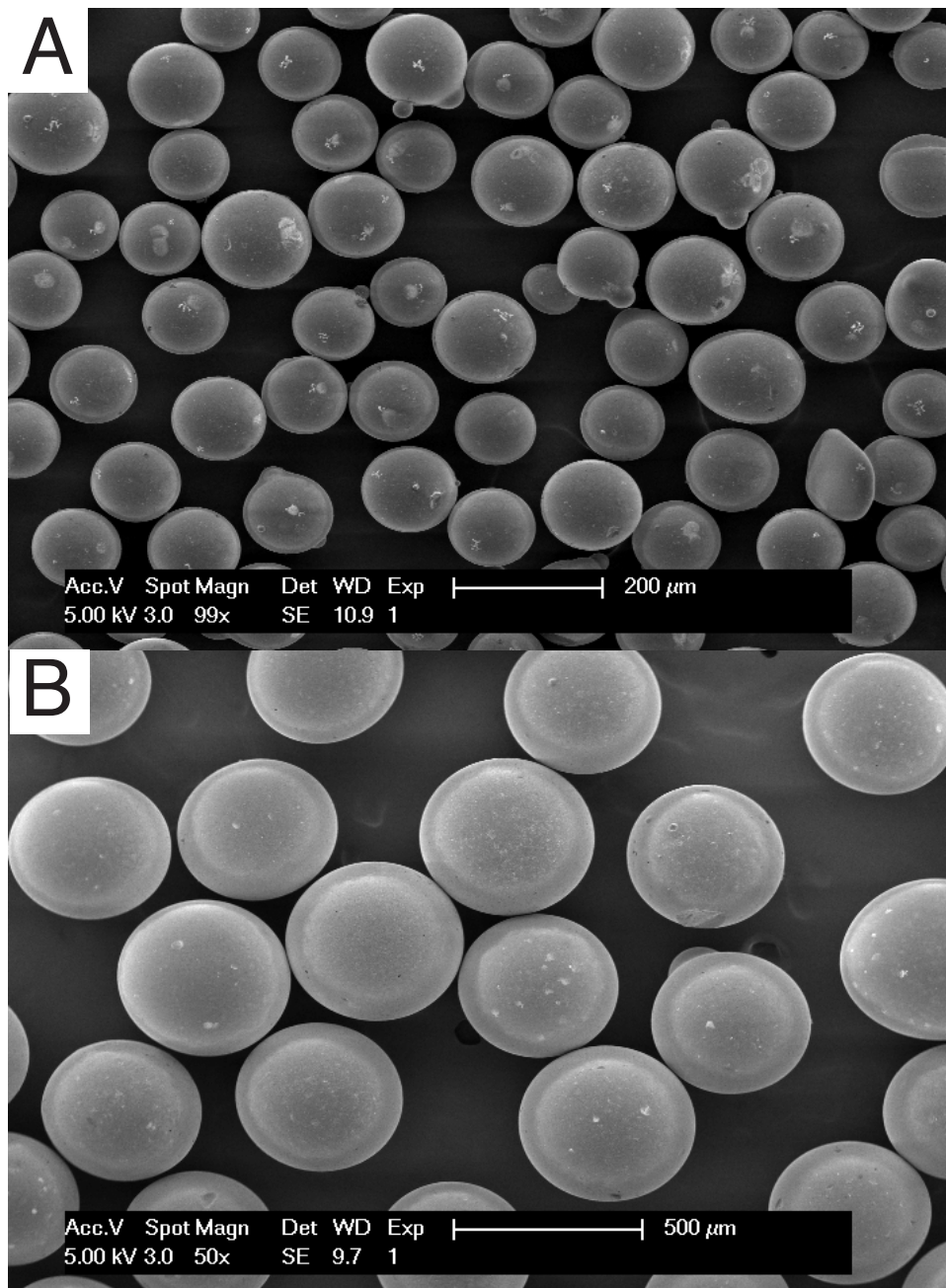


Fig. 5.2. Scanning electron microscope micrographs of the starting glass beads for all experiments. A) 100-150 μm B) 420-500 μm

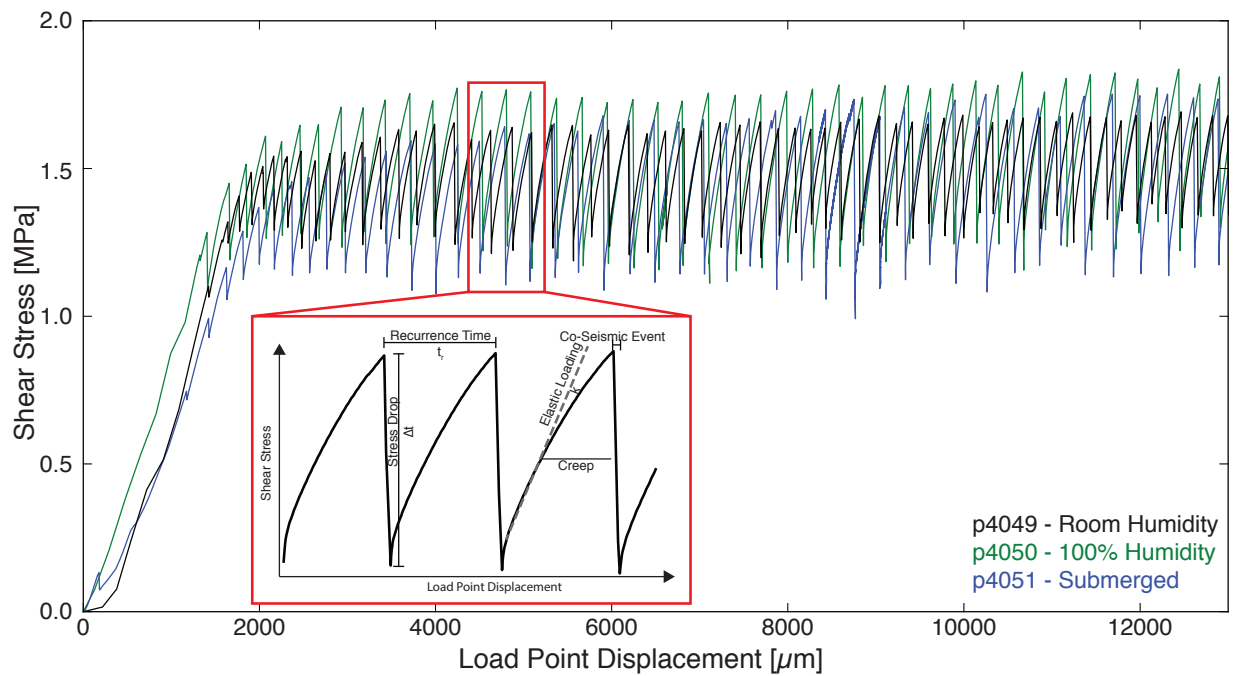


Fig. 5.3. Experiments performed on glass beads ($100\text{-}150\mu\text{m}$ diameter) under ambient humidity, 100% humidity, and submerged conditions exhibit similar mechanical behavior. Increased stress drops are observed with increased humidity and in the submerged case. Inset: Anatomy of a stick-slip event. The recurrence time is the time between peaks in shear stress. Initially the shear stress increases linear-elasticly. Deviation from line-elastic behavior marks the onset of elasto-plastic deformation and pre-seismic slip. When the ultimate strength of the layer is reached shear stress drops rapidly and the cycle begins again.

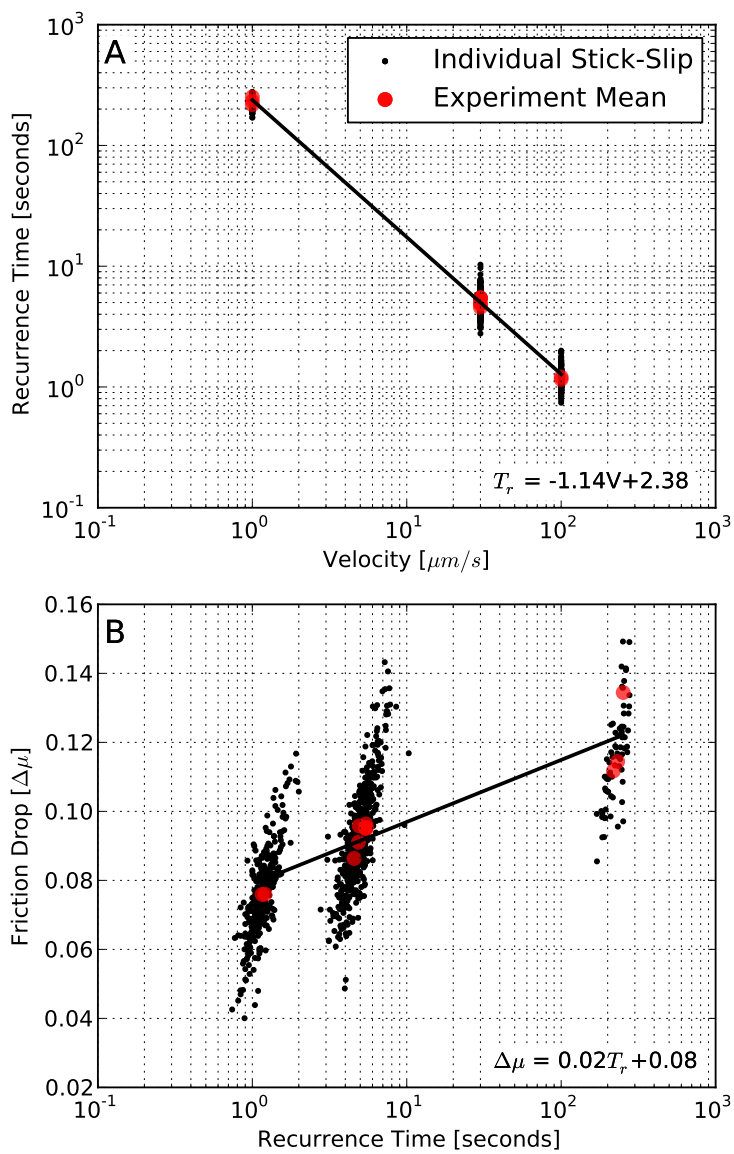


Fig. 5.4. A) Samples exhibit a log-log linear relation between recurrence time and velocity. Faster loading rates result in shorter recurrence times. B) Friction drop increases with the recurrence time as there is more time for the layer to heal before the next stick-slip event.

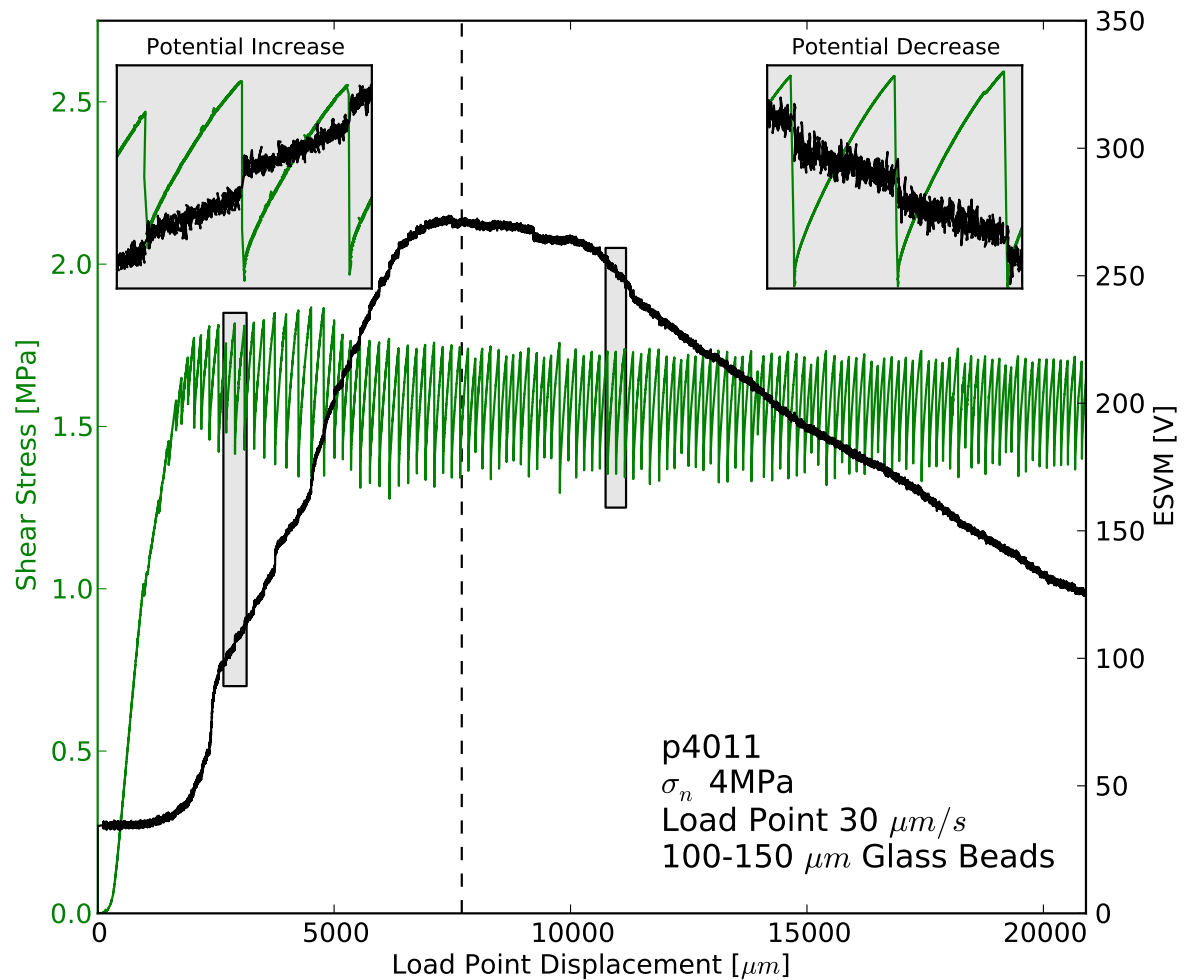


Fig. 5.5. During shearing two trends are observed: 1) A long-term charging/discharging trend in the electrical potential and 2) Potential change related to individual stick-slip events. The entire system initially charges, approximately until mechanical steady-state is reached. During this phase co-seismic potential changes are dominantly positive (top left inset). After attainment of mechanical steady-state, the system begins to maintain or discharge potential. During this phase the co-seismic potential changes are dominantly negative (top right inset).

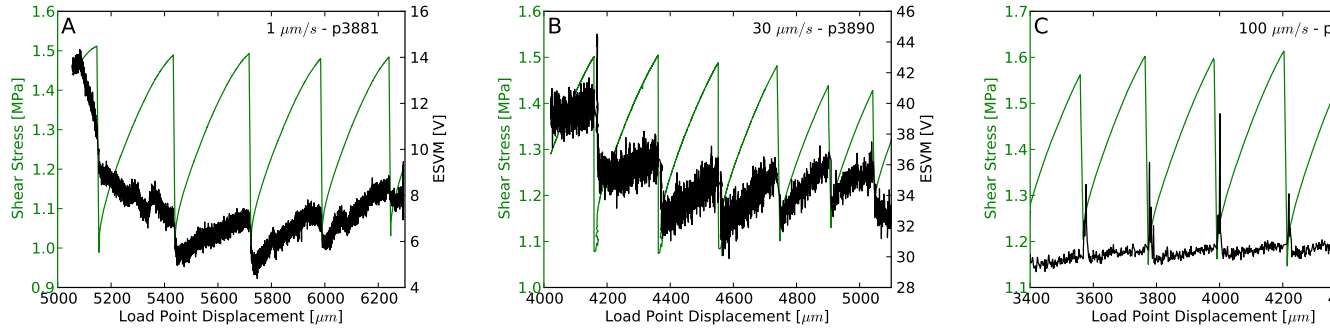


Fig. 5.6. Stick-slip events and associated ESVM measurements for three-different load point velocities of 1, 30, and 100 $\mu\text{m}/\text{s}$. A) At slow loading velocities the electrical signal clearly mirrors the stress curve in most cases B) For intermediate velocities, the relation is still present. C) At high velocities, the electrical signal is a sharp pulse an order of magnitude higher than those observed at low velocities, and we observe small inter-seismic charging.

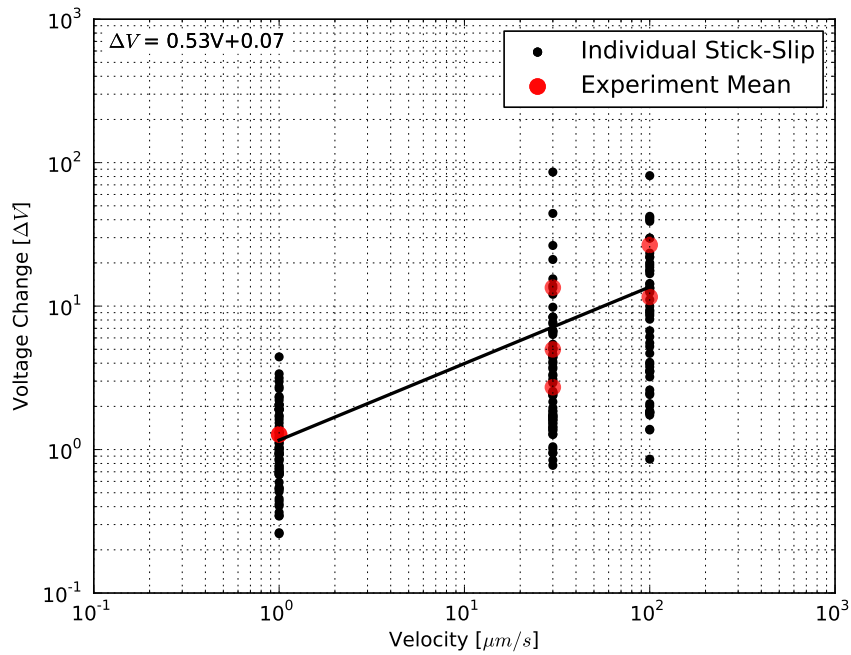


Fig. 5.7. Each order of magnitude driving velocity change produces a $\sim 5\times$ increase in the electrical signal observed. All experiments shown are with the side-view sensor geometry.

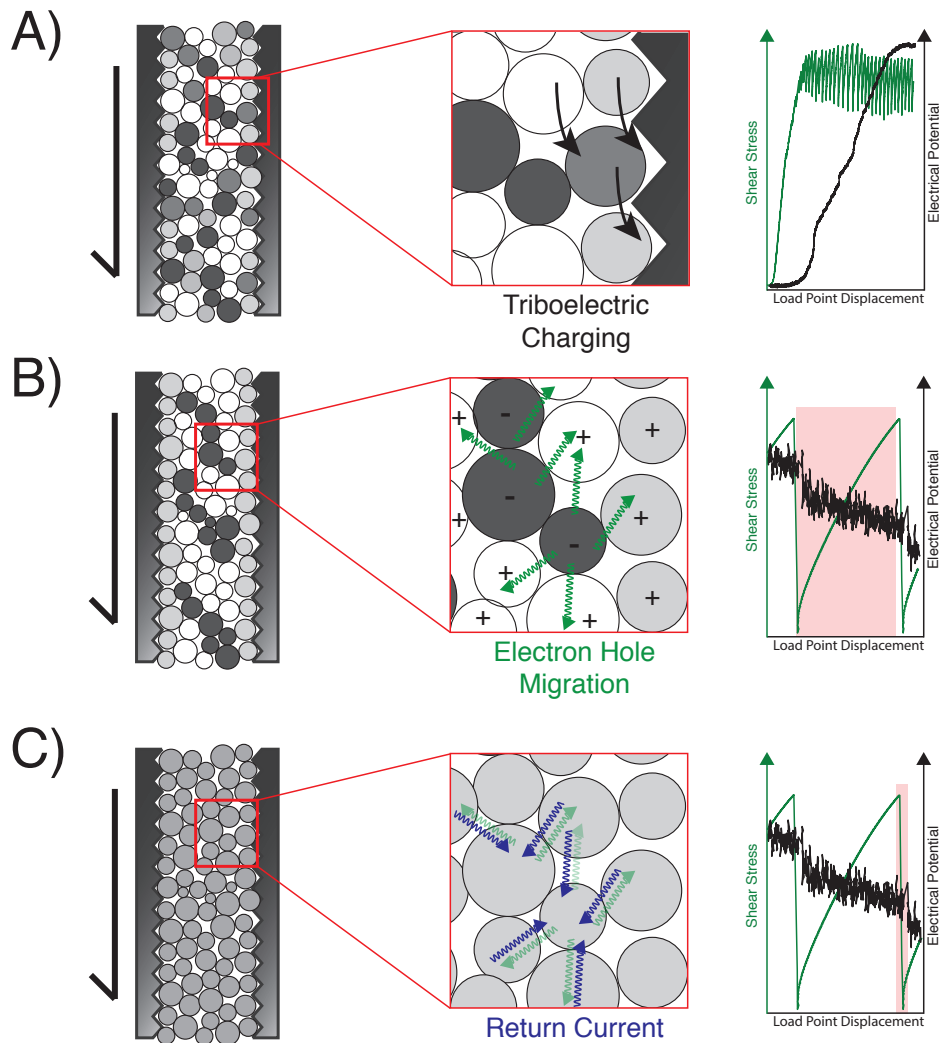


Fig. 5.8. A schematic representation of the stages of electrical behavior during an experiment: A) During the initial run-in there is massive grain rearrangement as force chain networks begin to form. This sliding motion tribo-electrically charges the system. B) After the force chain network forms there is minimal grain-boundary sliding. Shear loads are supported in the granular layer by highly stressed force chains (dark colors). Electron holes migrate away from highly stressed beads into the matrix creating an electrical potential gradient. C) When the layer fails and all grains are at roughly the same low stress, a return current redistributes the electrical gradient and the cycle begins again.

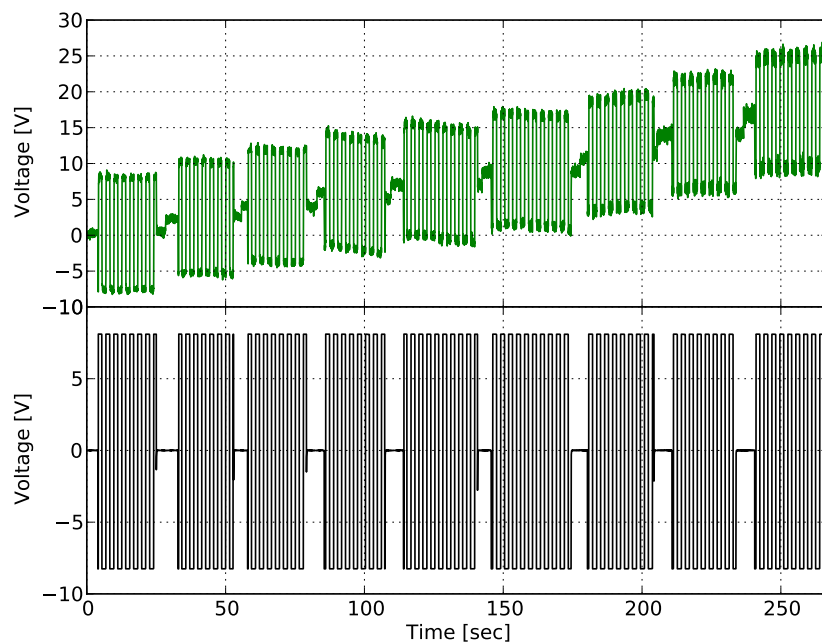


Fig. 5.9. Calibration of the ESVM from a function generator source (bottom panel). A series of steps through the ESVM ‘response’ setting from 1-9 shows that the input square wave applied to the aluminium surface under test is well-recorded on each setting (top panel). The upward trend in ESVM data is a product of a DC offset that occurs each time the response setting is changed on the instrument.

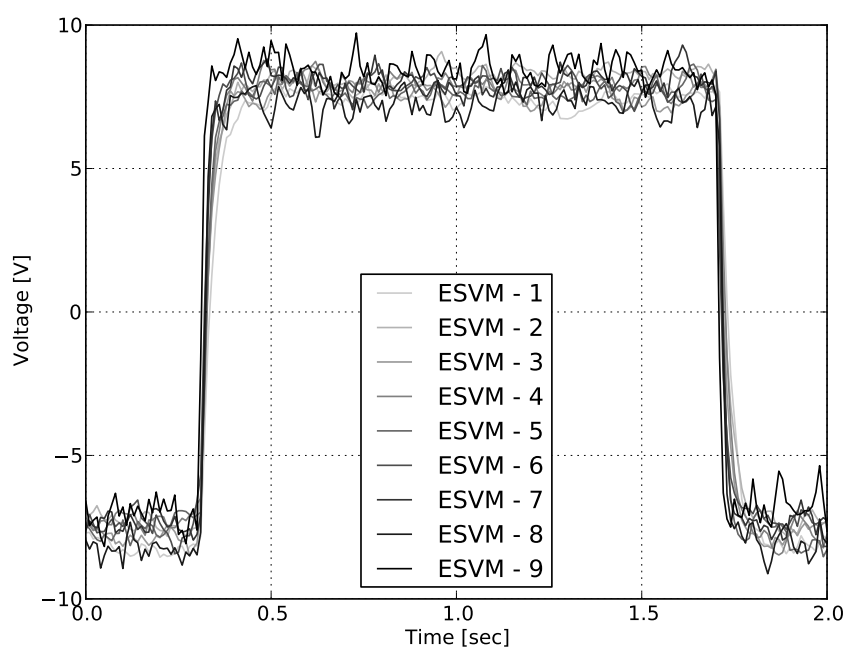


Fig. 5.10. A detailed comparison of a single waveform shows that at lower response settings (lighter colors) the waveform is smoothed slightly, with the nearly instantaneous voltage change distributed over up to 0.1 seconds on both the rise and fall. At higher resolutions (darker colors) the sharp transition is clearly seen, but at the price of a higher noise level during the flat hold states.

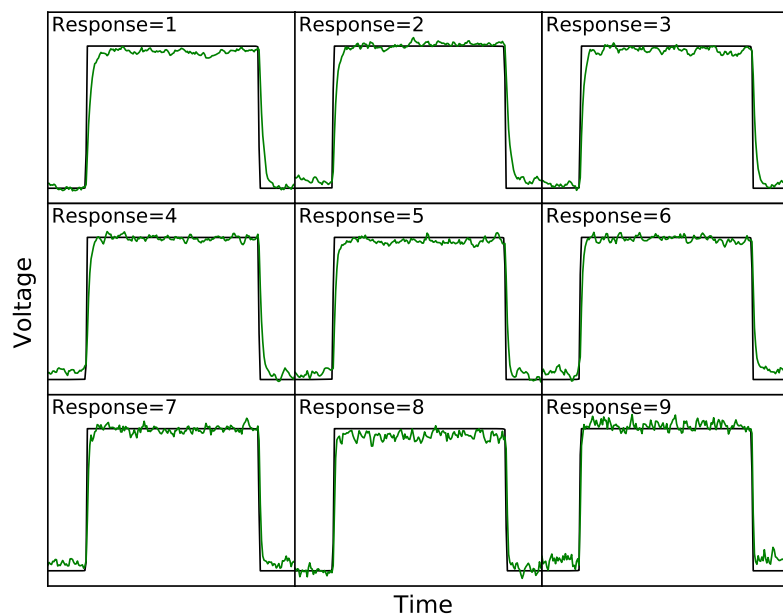


Fig. 5.11. At all response settings the beginning of ESVM signal change corresponds well in the time domain with the leading and falling edge of the input signal. Smoothing due to longer integration times is observed at low response settings.

Table 5.1. List of Experiments

Experiment	$V_{lp}, \mu\text{m/s}$	Bead Size, μm	Temperature, $^{\circ}\text{C}$	Humidity, %	Comment
p3853	30	420-500	23.3	41.2	Large Beads
p3878	30	100-150	23.8	23.8	Side View
p3879	30	420-500	24.7	20.2	Large Beads
p3880	30	420-500	25.7	20.7	Large Beads
p3881	30	100-150	26.9	20.7	Side View
p3882	30	100-150	26.0	14.0	Side View
p3887	30	100-150	22.7	22.5	Side View
p3889	1	100-150	23.4	24.8	Side View
p3890	100	100-150	24.1	33.8	Side View
p3893	100	100-150	21.9	19.9	Side View
p3894	1	100-150	22.7	19.8	Side View
p4010	30	100-150	23.9	23.0	Top View - Isolated Group
p4011	30	100-150	24.2	23.7	
p4012	30	100-150	24.5	22.0	
p4013	1	100-150	24.3	22.3	
p4014	30	100-150	23.0	100	
p4015	30	100-150	23.3	N/A	
p4049	30	100-150	23.9	27.0	
p4050	30	100-150	23.8	100	
p4051	30	100-150	23.9	N/A	
p4052	30	100-150	23.8	100	

Table 5.2. Composition of glass beads.

Compound	Composition, %
SiO_2	65-75%
Al_2O_3	0-5%
CaO	6-15%
MgO	1-5%
Na_2O	10-20%
Fe_2O_3	<0.8%

Appendix A

List of Biaxial Experiments

Date	Experiment	Block	Material	Grain Size	Thickness	Normal Stress	Velocity	Temperature
Text	Num	Matieral	Text	um	mm	Mpa	um/s	C
8/31/12	p3805	Granite	Glass Beads	100-150	5	5	5?	24
9/3/12	p3809	Granite	Glass Beads	100-150	5	5	10	24
9/21/12	p3825	Granite	Glass Beads	100-150	5	1	10	-
9/22/12	p3826	Granite	Glass Beads	100-150	5	31	10	23.4
9/22/12	p3827	Steel	Glass Beads	100-150	5	2.5,4	10,1,10	23.1
9/23/12	p3828	Steel	Glass Beads	100-150	5	2.5,4	10	22.8
9/23/12	p3829	Steel	Glass Beads	100-150	5	10	10	23.5
9/24/12	p3830	Steel	Glass Beads	100-150	5	10	10,30,10,100,10,30,500,30,10	21.9
9/24/12	p3831	Steel	Glass Beads	100-150	5	10	10,30,100,10	22.3
10/18/12	p3846	Acry/UMHW	Glass Beads	100-150	5	0.5,1	N/A	25.8
10/29/12	p3851	Acrylic	Glass Beads	100-150	5	4.3	10,100,10	22.4
10/29/12	p3852	Acrylic	Glass Beads	420-500	5	4.3	10,100,10,100,30	22.7
10/29/12	p3853	Acrylic	Glass Beads	420-500	5	4.3	30	23.3

DRAFT: OCTOBER 21, 2016 AT 3:49 PM

11/13/12	p3878	Acrylic	Glass Beads	100-150	5	4	30	23.8
11/14/12	p3879	Acrylic	Glass Beads	420-500	5	4	30	24.7
11/14/12	p3880	Acrylic	Glass Beads	420-500	5	4	30	25.7
11/15/12	p3881	Acrylic	Glass Beads	100-150	5	4	30	26.9
11/16/12	p3882	Acrylic	Glass Beads	100-150	5	4	30	26
11/22/12	p3886	Ice Core	Ice	N/A	N/A	N/A	100	21.6
11/22/12	p3887	Acrylic	Glass Beads	100-150	5	4	30	22.7
11/22/12	p3888	Acrylic	Glass Beads	Mixed	7	4	10	22.7
11/23/12	p3889	Acrylic	Glass Beads	100-150	5	4	1	23.4
11/23/12	p3890	Acrylic	Glass Beads	100-150	5	4	100	24.1
11/23/12	p3891	Ice Core	Ice	N/A	N/A	N/A	100	23.8
11/23/12	p3892	Acrylic	Glass Beads	Mixed	7	4	10	23.3
11/24/12	p3893	Acrylic	Glass Beads	100-150	5	4	100	21.9
11/24/12	p3894	Acrylic	Glass Beads	100-150	5	4	1	22.7
11/24/12	p3895	Ice Core	Ice	N/A	N/A	N/A	100	22.5

DRAFT: OCTOBER 21, 2016 AT 3:49 PM

12/13/12	p3916	Acrylic	Flour	Unknown	7	1	10,1,10,100,10,100,1,0.1	23.5
12/14/12	p3917	Acrylic/Steel	Flour	Unknown	7	1	10,1,0.1	22
12/15/12	p3918	Acrylic	Flour	Unknown	7	1	10,1	23.1
12/15/12	p3919	Acrylic	Flour	Unknown	7	1	1	24.2
12/15/12	p3920	Acrylic	Flour	Unknown	7	1	1,10	24.4
3/13/13	p4010	Acrylic	Glass Beads	100-150	5	4	30	23.9
3/13/13	p4011	Acrylic	Glass Beads	100-150	5	4	30	24.2
3/13/13	p4012	Acrylic	Glass Beads	100-150	5	4	30	24.5
3/13/13	p4013	Acrylic	Glass Beads	100-150	5	4	1	24.3
3/14/13	p4014	Acrylic	Glass Beads	100-150	5	4	30	23
3/14/13	p4015	Acrylic	Glass Beads	100-150	5	4	30	23.3
4/13/13	p4049	Acrylic	Glass Beads	100-150	5	4	30	23.9
4/14/13	p4050	Acrylic	Glass Beads	100-150	5	4	30	23.8
4/14/13	p4051	Acrylic	Glass Beads	100-150	5	4	30	23.9
4/15/13	p4052	Acrylic	Glass Beads	100-150	5	4	30	23.8

DRAFT: OCTOBER 21, 2016 AT 3:49 PM

4/15/13	not p	N/A	N/A	N/A	N/A	N/A	N/A	N/A
4/15/13	not p	N/A	N/A	N/A	N/A	N/A	N/A	N/A
5/5/13	p4061	N/A	Granite Core	N/A	N/A	N/A	N/A	-
5/26/13	p4071	Steel/Acrylic	F110	-	3	2	various	23.3
5/26/13	p4072	Steel/UMHW	F111	-	3	2	various	23.4
5/27/13	p4073	Steel	Flour	-	8	1	various	23.4
5/27/13	p4074	Steel/Acrylic	Flour	-	8	1	various	23.1
6/28/13	p4080	Large Steel	N/A	N/A	N/A	N/A	5	24.1
6/28/13	p4081	Large Steel	N/A	N/A	N/A	N/A	5	24.2
6/28/13	p4082	Large Steel	N/A	N/A	N/A	N/A	5	24.2
6/28/13	p4083	Large Steel	N/A	N/A	N/A	N/A	5	24.4
6/28/13	p4084	Large Steel	N/A	N/A	N/A	N/A	5	24.6
6/28/13	p4085	Large Steel	N/A	N/A	N/A	N/A	5	24.6
7/1/13	p4086	Large Steel	N/A	N/A	N/A	N/A	5	24.1
7/1/13	p4087	Large Steel	N/A	N/A	N/A	N/A	5	23.9

DRAFT: OCTOBER 21, 2016 AT 3:49 PM

7/1/13	p4088	Large Steel	N/A	N/A	N/A	N/A	5	23.9
7/22/13	p4108	Granite	N/A	N/A	N/A	2	various	25.5
7/25/13	p4111	Granite	N/A	N/A	N/A	2	various	25.2
7/26/13	p4112	Steel	Flour	Unknown	8	1	various	24.3
7/26/13	p4113	Steel	Flour	Unknown	8	1	various	24.3
7/30/13	p4115	Granite	N/A	N/A	N/A	4	various	24.5
7/30/13	p4116	Granite	N/A	N/A	N/A	4	various	N/A
7/30/13	p4117	Granite	N/A	N/A	N/A	4	various	24.7
7/31/13	p4118	Granite	N/A	N/A	N/A	4	various	24.3
7/31/13	p4119	Granite	N/A	N/A	N/A	4	various	24.5
8/1/13	p4120	Granite	N/A	N/A	N/A	4	various	24.4
8/2/13	p4121	Steel	F110	N/A	5	25	various	24.7
11/9/13	p4175	steel	F110	N/A	5	25	10	24.3
11/10/13	p4176	steel	Alpine Fault	<125	5	30	10	23
11/10/13	p4177	steel	Alpine Fault	<125	5	30	10	23.6

DRAFT: OCTOBER 21, 2016 AT 3:49 PM

11/10/13	p4178	steel	Alpine Fault	<125	5	30	10	23.8
11/15/13	p4181	Steel	Glass Beads	100-150	5	4.5	various	24.7
11/15/13	p4182	Steel	Glass Beads	100-150	5	4.5	various	24.6
11/16/13	p4183	Steel	Glass Beads	100-150	5	4.5	various	25.4
11/16/13	p4184	Steel/UMHW	Min-u-sil	10	3	1	various	26
11/16/13	p4185	Titanium/Acrylic	Min-u-sil	10	3	4	various	24.3
11/17/13	p4186	Titanium/Acrylic	Min-u-sil	10	3	4	various	23.9
11/17/13	p4187	Titanium/Acrylic	Min-u-sil	10	3	4	various	25.5
11/17/13	p4188	Steel/Acrylic	Westerly Po	<125	3	4	various	25
11/17/13	p4189	Titanium/Acrylic	Min-u-sil	10	3	4	various	26
11/18/13	p4190	Granite	N/A	N/A	N/A	3	various	24.3
11/18/13	p4191	Titanium/Acrylic	Min-u-sil	10	3	4	various	24.6
1/10/14	p4206	Steel/Acrylic	Min-u-sil	10	3	4	various	23.3
1/10/14	p4207	Steel/Acrylic	Min-u-sil	10	3	4	various	23.2
1/23/14	p4211	Steel	F110	110	5	25	various	23.3

DRAFT: OCTOBER 21, 2016 AT 3:49 PM

11/18/13	p4192	Steel	Min-u-sil	10	3	4	various	25.4
2/27/13	p4224	Titanium/Acrylic	Min-u-sil	10	3	5	various	26
2/28/14	p4225	Titanium/Acrylic	Min-u-sil	10	3	5	various	22
2/28/14	p4226	Titanium/Acrylic	Min-u-sil	10	3	4	various	22
3/1/14	p4227	Titanium/Acrylic	Min-u-sil	10	3	4	various	24
3/1/14	p4228	Steel	Min-u-sil	10	3	4	various	24
3/3/14	p4229	Titanium/Acrylic	Min-u-sil	10	3	4	various	24
	p4238							
4/25/14	p4247	Titanium/Acrylic	Min-u-sil	10	3	4	various	23
4/26/14	p4248	Titanium/Acrylic	Min-u-sil	10	3	4	various	24.2
4/26/14	p4249	Titanium/Acrylic	Min-u-sil	10	3	4	various	23.2
4/27/14	p4250	Titanium/Acrylic	Min-u-sil	10	3	4	various	22.7
4/27/14	p4251	Titanium/Acrylic	Min-u-sil	10	3	4	various	23.2
5/22/14	p4267	Titanium/Acrylic	Min-u-sil	10	3	2	various	23.2
5/23/14	p4268	Titanium/Acrylic	Min-u-sil	10	3	8	10	23.4

DRAFT: OCTOBER 21, 2016 AT 3:49 PM

5/23/14	p4269	Steel	Min-u-sil	10	3	4	various	23.4
5/24/14	p4270	Steel	Min-u-sil	10	3	2	various	
5/24/14	p4271	Titanium/Acrylic	Min-u-sil	10	3	2	various	
5/25/14	p4272	Titanium/Acrylic	Min-u-sil	10	3	8	10	22.7
5/25/14	p4273	Steel	Min-u-sil	10	3	8	various	23.4
8/28/14	p4308	Steel	N/A	N/A	N/A	4	N/A	23.5
8/31/14	p4309	Steel	Min-u-sil	10	3	8	various	23.2
8/31/14	p4310	Titanium/Acrylic	Min-u-sil	10	3	8	various	24.2
9/1/14	p4311	Titanium/Acrylic	Min-u-sil	10	3	8	various	23.3
9/1/14	p4312	Steel/Acrylic	Min-u-sil	10	3	8	various	23.6
9/2/14	p4313	Titanium/Acrylic	Min-u-sil	10	3	8	various	23.5
9/2/14	p4314	Steel	Min-u-sil	10	3	12	various	24.3
9/2/14	p4315	N/A	N/A	N/A	N/A	N/A	N/A	N/A
9/3/14	p4316	Titanium/Acrylic	Min-u-sil	10	3	12	various	23.6
9/3/14	p4317	Steel/Acrylic	Min-u-sil	10	3	12	various	24.2

DRAFT: OCTOBER 21, 2016 AT 3:49 PM

10/11/14	p4327	Steel	Min-u-sil	10	3	6	various	22.5
10/11/14	p4328	Titanium/Acrylic	Min-u-sil	10	3	6	various	22.7
10/12/14	p4329	Titanium/Acrylic	Min-u-sil	10	3	6	various	22
10/12/14	p4330	Steel	Min-u-sil	10	3	6	various	22.9
11/3/14	p4336	Titanium/Acrylic	Min-u-sil	10	3	8	10	24.8
11/4/14	p4337	Titanium/Acrylic	Min-u-sil	10	3	8	10	24.8
11/15/14	p4338	Titanium/Acrylic	Min-u-sil	10	3	4	10	24.2
11/15/14	p4339	Steel	Min-u-sil	10	3	4	various	24.8
11/16/14	p4340	Titanium/Acrylic	Min-u-sil	10	3	8	various	24
11/24/14	p4341	Steel	Min-u-sil	10	3	12	10	23.4
11/24/14	p4342	Titanium/Acrylic	Min-u-sil	10	3	12	10	24.3
11/25/14	p4343	Steel/Acrylic	Min-u-sil	10	3	6	10	23.9
11/25/14	p4344	Titanium/Acrylic	Min-u-sil	10	3	7	10	24.5
11/26/14	p4345	Steel/Acrylic	Min-u-sil	10	3	8	10	24.2
11/26/14	p4346	Titanium/Acrylic	Min-u-sil	10	3	9	10	24.2

DRAFT: OCTOBER 21, 2016 AT 3:49 PM

11/29/14	p4347	Steel/Acrylic	Min-u-sil	10	3	10	10	23.1
11/29/14	p4348	Titanium/Acrylic	Min-u-sil	10	3	11	10	23.9
11/29/14	p4349	Steel	Glass Beads	100-150	3	6	10	24.1
11/30/14	p4350	Steel/Acrylic	Min-u-sil	10	3	13	10	22.7
11/30/14	p4351	Titanium/Acrylic	Min-u-sil	10	3	14	10	23.1
1/14/15	p4362	N/A	Si Powder	N/A	N/A	N/A	N/A	N/A
3/3/15	p4379	Steel	Min-u-sil	10	3	4	various	24.5
3/7/15	p4381	Steel	Min-u-sil	10	3	4	various	22.7
3/7/15	p4382	Titanium	Min-u-sil	10	3	4	various	23.1
4/27/15	p4397	Granite	N/A	N/A	N/A	4	various	N/A
4/28/15	p4398	Steel	F110		3	25	various	21.8
10/20/15	p4462	Granite	Core	N/A	N/A	N/A	N/A	21.8
1/29/16	p4522	Steel/Acrylic	Min-u-sil	10	3	7	10	21.6
1/29/16	p4523	Titanium/Acrylic	Min-u-sil	10	3	7	30	21.8
1/30/16	p4524	Steel/Acrylic	Min-u-sil	10	3	7	3	20.8

DRAFT: OCTOBER 21, 2016 AT 3:49 PM

1/30/16	p4525	Titanium/Acrylic	Min-u-sil	10	3	7	100	21.9
1/31/16	p4526	Steel/Acrylic	Min-u-sil	10	3	7	300	N/A
1/31/16	p4527	Titanium/Acrylic	Min-u-sil	10	3	7	10, 30	21.9
5/4/16	p4599	Titanium/Acrylic	Min-u-sil	10	3	7	acceleration file	22.3
5/5/16	p4600	Steel	Min-u-sil	10	3	2	various	22.7
5/5/16	p4601	Steel/Acrylic	Min-u-sil	10	3	12	30	22.7
5/6/16	p4602	Titanium/Acrylic	Min-u-sil	10	3	12	3	22.7
5/7/16	p4603	Steel/Acrylic	Min-u-sil	10	3	12	300	22.7
5/7/16	p4604	Steel/Acrylic	Min-u-sil	10	3	12	100	22.1
5/8/16	p4605	Steel/Acrylic	Min-u-sil	10	3	9	100	21.9
5/8/16	p4606	Steel/Acrylic	Min-u-sil	10	3	9	300	21.9
5/9/16	p4607	Steel/Acrylic	Min-u-sil	10	3	7	100	22.6
5/9/16	p4608	Steel/Acrylic	Min-u-sil	10	3	7	300	22.6
5/9/16	p4609	Titanium	Kinetic Sand	?	3	7	various	22.5
5/10/16	p4610	Steel/Acrylic	Min-u-sil	10	3	5	10	21.1

DRAFT: OCTOBER 21, 2016 AT 3:49 PM

5/10/16	p4611	Steel/Acrylic	Min-u-sil	10	3	5	30	22.2
5/11/16	p4612	Westerly	N/A	N/A	N/A	4	various	N/A
5/12/16	p4613	Steel	Min-u-sil	10	3	7	10	21.9
5/12/16	p4614	Steel/Acrylic	Min-u-sil	10	3	5	3	20.8

DRAFT: OCTOBER 21, 2016 AT 3:49 PM

Appendix B

List of Triaxial Experiments

Electromagnetic signals have been reported in association with geophysical phenomena including earthquakes, landslides, and volcanic events. Mechanisms that suggested to explain seismoelectrical signals include triboelectricity, piezoelectricity, streaming potentials, and the migration of electron holes, yet the origin of such phenomena remains poorly understood. We present results from laboratory experiments regarding the relationship between electrical and mechanical signals for frictional stick-slip events in sheared soda-lime glass bead layers. The results are interpreted in the context of lattice defect migration and granular force chain mechanics. During stick-slip events, we observe two distinct behaviors delineated by the attainment of a frictional stick-slip steady state. During initial shear loading, layers charge during stick-slip events and the potential of the system rises. After steady state stick-slip behavior is attained, the system begins to discharge. Coseismic signals are characterized by potential drops superimposed on a longer-term trend. We suggest that the observed signal is a convolution of two effects: charging of the forcing blocks and signals associated with the stress state of the material. The long-term charging of the blocks is accomplished by grain boundary movement during the initial establishment of force chain networks. Short-term signals associated with stick-slip events may originate from produced electron holes. Applied to tectonic faults, our results suggest that electrical signals generated during frictional failure may

provide a way to monitor stress and the onset of earthquake rupture. Potential changes could produce detectable signals that may forecast the early stages of failure, providing a modest warning of the event.

Appendix C

Sample Preparation Procedures

Electromagnetic signals have been reported in association with geophysical phenomena including earthquakes, landslides, and volcanic events. Mechanisms that suggested to explain seismoelectrical signals include triboelectricity, piezoelectricity, streaming potentials, and the migration of electron holes, yet the origin of such phenomena remains poorly understood. We present results from laboratory experiments regarding the relationship between electrical and mechanical signals for frictional stick-slip events in sheared soda-lime glass bead layers. The results are interpreted in the context of lattice defect migration and granular force chain mechanics. During stick-slip events, we observe two distinct behaviors delineated by the attainment of a frictional stick-slip steady state. During initial shear loading, layers charge during stick-slip events and the potential of the system rises. After steady state stick-slip behavior is attained, the system begins to discharge. Coseismic signals are characterized by potential drops superimposed on a longer-term trend. We suggest that the observed signal is a convolution of two effects: charging of the forcing blocks and signals associated with the stress state of the material. The long-term charging of the blocks is accomplished by grain boundary movement during the initial establishment of force chain networks. Short-term signals associated with stick-slip events may originate from produced electron holes. Applied to tectonic faults, our results suggest that electrical signals generated during frictional failure may

provide a way to monitor stress and the onset of earthquake rupture. Potential changes could produce detectable signals that may forecast the early stages of failure, providing a modest warning of the event.

Appendix D

Load Cell Theoretical Response

D.1 Introduction

Load cells are essential tools to measuring force in any industrial or scientific system. One of the most common types of load cells is the strain gauge load cell. In this type of load cell the deformation of a test material is measured as a change in the electrical resistance of bonded strain gauge elements. The test material that the load cell is made of is ideally very rigid, otherwise significant elastic energy is stored by the load cell and it will account for a non-negligible amount of deformation in the total system. Large strains can also permanently damage the load cell by permanently deforming the load cell or strain gauges and/or breaking the bonding of the load cells to their substrate.

Here, I will summarize the load cells used in the biaxial deformation apparatus and provide a reference for calculations of the predicted load cell response and calibration procedures. Calibration and verification of that calibration against the predicted theoretical model is essential to performing accurate experiments and ensuring that the system is performing as expected and not in need of further maintenance/repair.

D.2 Load Cell Design

Load cells on the biaxial apparatus are generally constructed of beryllium-copper, but could be constructed of any material with the appropriate properties. We desire

a rigid material that can sustain several times the maximum designed load without permanent deformation. Temperature stability is also essential and resistive heating from the strain gauges and environmental temperature changes can introduce undesirable zero point drift in the system. Our design strives to cancel as much of these effects as possible.

D.2.1 Material properties

Our loads cells are made of Beryllium copper (BeCu). This material was chosen for its resilience to repeated straining. It has long been a standard for load cells and is a non-ferrous, non-sparking material. The material properties are as follows in table 1.

D.2.2 Mechanical design

Currently we employ two load cell geometries: 1) a hollow ring with an ~ 62 mm outer diameter and ~ 54 mm inner diameter, 2) a solid cylinder of ~ 44 mm diameter (Fig.D.1). The load cells provide similar responses and are both linear with load under the applicable conditions. The area of loading is important for modeling cell response. Area of the load cell can be calculated via eq.D.1 assuming a load cell outer diameter r_o and inner diameter r_i .

$$A = \pi(r_o^2 - r_i^2) \quad (\text{D.1})$$

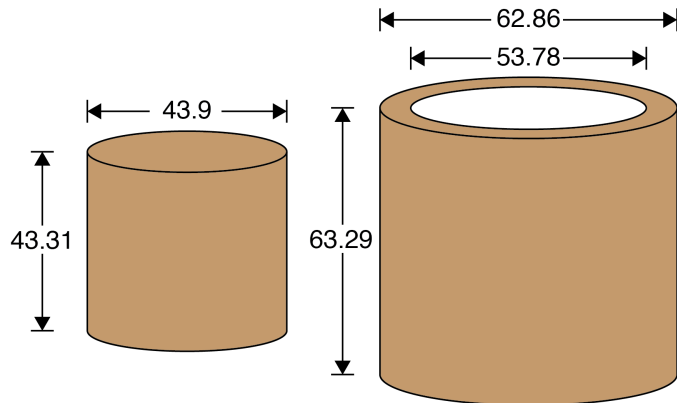


Fig. D.1. Mechanical drawings of the two styles of load cells used in the lab. Dimensions are in mm. Oblique view not to scale.

D.2.3 Electrical design

Load cells are fitted with eight bonded foil strain gauges. This configuration provides high sensitivity and information from two orientations (axial and radial). A simple Wheatstone bridge configuration is used (Fig.D.2). Sets of gauges are placed at 90° intervals around the load cell and bonded following the manufacturer's instructions. A cartoon of the construction and electrical hook-up is often helpful when troubleshooting or constructing load cells (Fig.D.3).

The Wheatstone bridge is excited by XX VDC provided by the strain gauge signal conditioner. The signal conditioner is a 1B31AN, manufactured by Analog Devices. A raw voltage from the load cell returns to the control system through an INA105 amplifier with switchable gain on the control panel (for the horizontal axis). The signal then passes to the 1B31AN for further gain and filtering.

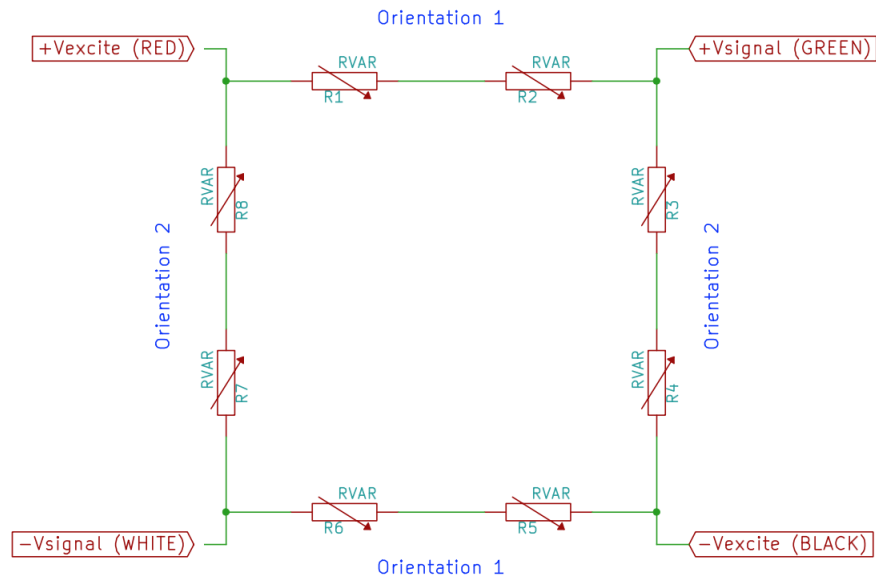


Fig. D.2. Electrical schematic of the 8-gauge load cell design. Orientation 1 and 2 are marked for identification convenience.

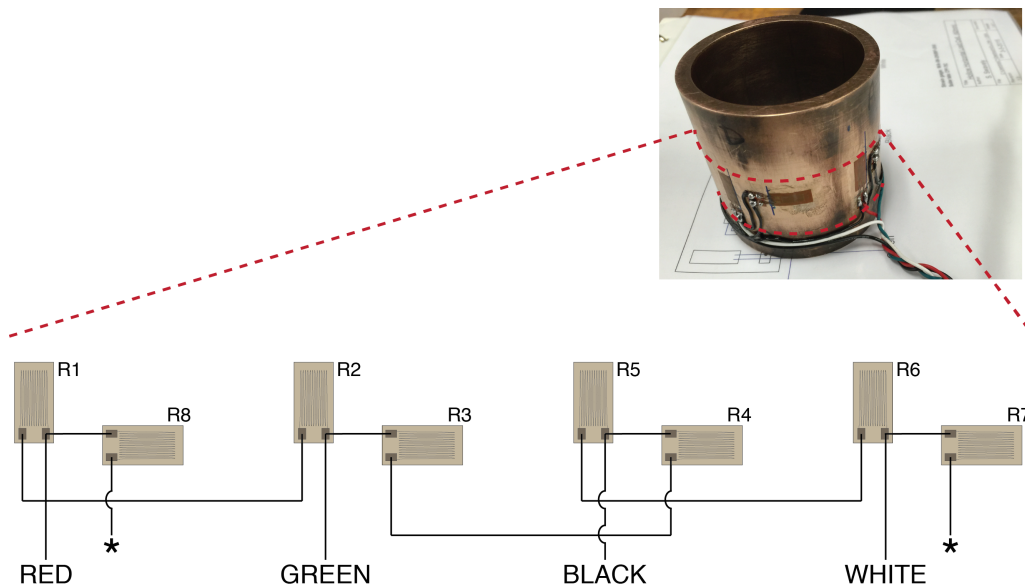


Fig. D.3. Physical construction of the load cell and arrangement of strain gauges. gauge sets are set apart by 90°. Electrical points marked * are connected.

D.3 Predicted response

Predicting the response of the load cell involves calculating the mechanical response to stress and then transferring that information to calculations about the response of the strain gauges and amplifier circuits. This has been accomplished in a jupyter notebook that can be easily modified and experimented with. Here I will outline the basic procedure for the calcualtions.

First we must ascertain the necessary mechanical properties of the load cell material. In this particular case, the shear modulus (G) and Young's modulus (E) were most easily obtained. Lame's first parameter can then be calculated using eq.D.2. With the elastic parameters in place, the response of the load cell to applied stress can be calculated. Since for the stresses applied in the lab BeCu behaves in a linear-elastic fashion, Hook's Law for elastic solids can be applied (eqs. D.3,D.4,D.5). These equations can be simplified for a case of uni-axial loading, but have been left in their full form to provide the most versatility for future application. Proof of equality is provided in the notebook. Initially intuition will say that a correction is needed for circumferential gauges, but writing out the equation for circumferential strain (eq.D.6) shows that no correction is needed since the diametric strain is equal to ϵ_3, ϵ_3 .

$$\lambda = \frac{G(E - 2G)}{3G - E} \quad (\text{D.2})$$

$$\epsilon_1 = \sigma_1 \frac{(\lambda + G)}{G(3\lambda + 2G)} - \sigma_2 \frac{\lambda}{2G(3\lambda + 2G)} - \sigma_3 \frac{\lambda}{2G(3\lambda + 2G)} \quad (\text{D.3})$$

$$\epsilon_2 = -\sigma_1 \frac{\lambda}{2G(3\lambda + 2G)} + \sigma_2 \frac{(\lambda + G)}{G(3\lambda + 2G)} - \sigma_3 \frac{\lambda}{2G(3\lambda + 2G)} \quad (\text{D.4})$$

$$\epsilon_3 = -\sigma_1 \frac{\lambda}{2G(3\lambda + 2G)} - \sigma_2 \frac{\lambda}{2G(3\lambda + 2G)} + \sigma_3 \frac{(\lambda + G)}{G(3\lambda + 2G)} \quad (\text{D.5})$$

$$\epsilon_c = \frac{\Delta c}{c_i} = \frac{\pi(d_f - d_i)}{\pi d_i} \quad (\text{D.6})$$

Next the response of the strain gauges must be calculated. The fractional change in resistance per strain is characterized by the gauge factor (ξ) of the particular strain gauge. This is a number typically near 2 for the strain gauges used in our applications. With slight manipulation the proportional resistance change to the no-strain resistance (R_g) or the change in resistance is obtained through equation D.7.

$$\xi = \frac{\Delta R/R_g}{\epsilon} \quad (\text{D.7})$$

With a predicted resistance change for each gauge, it is possible to calculate the bridge balance with equation D.8.

$$V_{bridge} = V_{ex} \left(\frac{R_5 + R_6}{R_5 + R_6 + R_7 + R_8} - \frac{R_3 + R_4}{R_1 + R_2 + R_3 + R_4} \right) \quad (\text{D.8})$$

Appendix E

Load Cell Calibration Procedure

E.1 Introduction

Load cells are essential tools to measuring force in any industrial or scientific system. One of the most common types of load cells is the strain gauge load cell. In this type of load cell the deformation of a test material is measured as a change in the electrical resistance of bonded strain gauge elements. The test material that the load cell is made of is ideally very rigid, otherwise significant elastic energy is stored by the load cell and it will account for a non-negligible amount of deformation in the total system. Large strains can also permanently damage the load cell by permanently deforming the load cell or strain gauges and/or breaking the bonding of the load cells to their substrate.

Here, I will summarize the load cells used in the biaxial deformation apparatus and provide a reference for calculations of the predicted load cell response and calibration procedures. Calibration and verification of that calibration against the predicted theoretical model is essential to performing accurate experiments and ensuring that the system is performing as expected and not in need of further maintenance/repair.

E.2 Calibration procedure

Calibration of load cells is accomplished with a NIST traceable transfer calibration standard. The transfer standard is periodically sent out for recalibration or re-calibrated

if it encounters a physical shock such as dropping or hitting. The transfer standard and load cell are loaded in a series configuration and the readings of both recorded. From this a calibration curve can be constructed. The calibration procedure is as follows:

1. Connect the load cell to the appropriate electronics on the biax (i.e. vertical or horizontal axis). Allow a minimum of 30 minutes warm-up to ensure that the cell will not drift due to resistive heating from the strain gauges. The mechanical installation of the cell and preparation for calibration can take place during warm-up.
2. Plug the 4.5 digit multimeter into the appropriate load cell plugs on the biax front panel.
3. Adjust the zero point of the load cell on the biax control panel. A no-load voltage of around -4.5 VDC is best.
4. Attach the appropriate ram nose adapter on the vertical hydraulic ram and insert the load cell, gently tightening the set screws. Be sure the cell is inserted all the way into the adapter. Attach a DCDT to the adapter and connect it.
5. Place the proving ring beneath the load cell, centered in both axes. Centering is crucial to ensure no damage to the load cell or the proving ring. Be careful, the proving ring is heavy.
6. Place a steel loading puck between the proving ring and the load cell. Verify that the setup is aligned and that all parts are in-place (Fig.E.1).

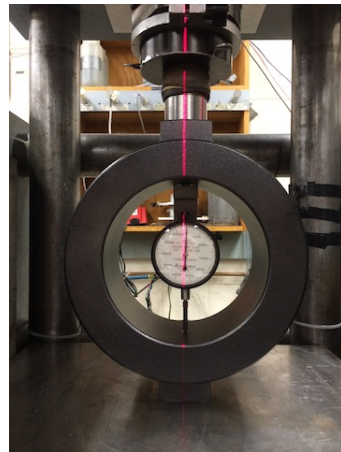


Fig. E.1. A proper setup of the load cell, steel puck, proving ring stack. Notice the careful alignment of all members.

7. With the vertical servo control system set to displacement feedback, zero and unlock the machine. Be sure you are at the beginning of the displacement range for the DCDT.
8. Bring the piston down until it is almost touching the proving ring. Check and make sure that a DCDT offset isn't needed. Running out of DCDT range during calibration will result in severe damage to the proving ring.
9. Check the proving ring dial gauge readout. If needed, adjust it to read zero klf (Fig.E.2).
10. Begin recording on the LabView recorder. This data isn't used unless something goes wrong, in that case it provides a "black box" style recording of what occurred.
11. Set the controller to run the piston downward at 5 um/s. This setting will depend on which DCDT you have installed.

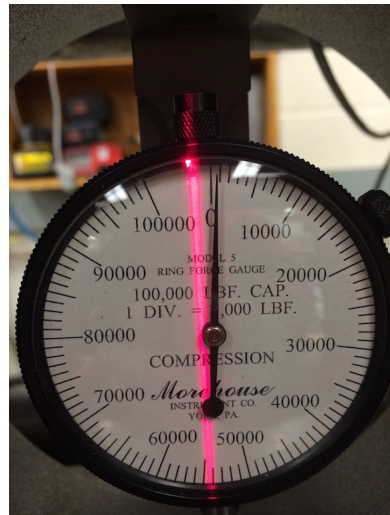


Fig. E.2. An example of a proving ring dial under no load that needs adjustment. Simply loosen the dial face set-screw to move the gauge legend.

12. Take a reading at zero load from the panel meter. Record this value.
13. Apply a load to the cell and record the voltage reading. Generally we calibrate low gain biax load cells from 0-65 klbf and high gain from 0-15 klbf. Low stresses should be sampled more often. A common sequence is 0,2.5,5,7.5,10,15,20,25,30,35,...,65 klbf).
14. Repeat step 12 for all loads listed in the loading table. Be sure to not go out of range on the DCDT or load cell.
15. Repeat the measurements for all loads during the unloading process as well. This characterizes any drift or repeatability issues.
16. Convert the loads from klbf to kN. $1 \text{ kN} = 4.44822162 \text{ klbf}$

17. Plot the voltage (in mV) and load (in kN). Fit a line. There should not be any appreciable non-linear or hysteresis behavior. If there is, consider recalibrating or troubleshooting the load cell.
18. Update load cell calibration numbers in the calibration file, logsheets, and your notes.

E.3 Typical measured response

As an example of a typical load cell response, a calibration of the 44mm solid load cell shows a very linear trend with no hysteresis (Fig.E.3).

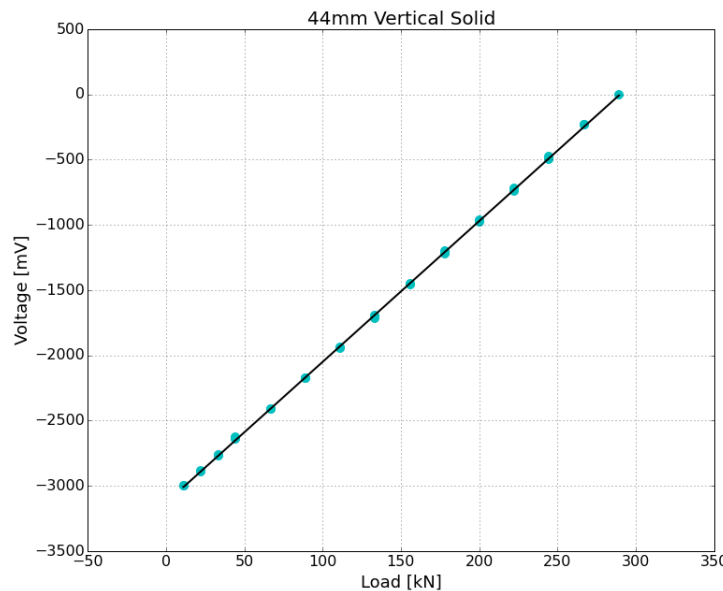


Fig. E.3. An example calibration obtained from the 44mm solid load cell.

Appendix F

DCDT Calibration Procedure

F.1 Introduction

Direct Current Displacement Transducers or Direct Current Differential Transformers (DCDTs) are devices used to very precisely measure rectilinear motion. In the transducer there are a primary and two secondary coils wound around a tube through which the core of the transducer travels. The primary coil is driven with a high frequency alternating current waveform. The alternating magnetic field created is coupled into the two counter wound secondary coils via a magnetically permeable core. The position of the core determines how much coupling there is between the primary and each of the secondary coils. Therefore the output of the secondary coils is a linear function of displacement. Which side of center the core is on is encoded by the phase of the output with respect to the input. We use DCDTs which are excited by a direct current input and provide a direct current output. The creation of the driving waveform and conditioning of the signal output is all done on board the transducer.

In this appendix I will briefly show the calibration procedures used to calibrate our DCDTs in the laboratory. Calibrations should be performed semi-annually. If a transducer's response has changed significantly, it could be time to replace the transducer. Other problems such as response hysteresis and noise should be noted as well.

F.2 Calibration procedure

Calibration of displacement transducers is accomplished with a NIST traceable transfer calibration standard. Using the electronics that will be used during the experiment, the transducer is placed a number of displacements using a vernier height gage. The response is recorded and a calibration curve constructed. The calibration procedure is as follows:

1. Connect the DCDT to the appropriate electronics on the biax (i.e. vertical or horizontal axis). Allow a minimum of 10-15 minutes warm-up to ensure that the transducer will not drift. You will notice that the transducers and cores get very warm. It is best to have the transducer near its null position during warm-up.
2. Mount the transducer to a ring-stand using a universal clamp and adjust it to be perpendicular to the table.
3. Using a 4-40 all thread segment, mount the core of the transducer to the vernier height gage.
4. Set the height gage to an even millimeter increment.
5. Make sure the transducer zero settings are close to their minimum values and that no DC offsets are being applied.
6. Plug the 4.5 digit multimeter into the appropriate banana plugs on the biax front panel.
7. Slide the transducer over the core and find the bottom of the output range. Lock it in place on the ring stand.

8. Take a reading at this zero displacement condition from the panel meter. Record this value.
9. Move the transducer in 1 mm or 0.5 mm steps, depending on its range. A minimum of 10 displacement values should be measured over the range of the transducer. At each step record the output voltage of the system.
10. Plot the voltage (in mV) and displacement (in mm). Fit a line. There should not be any appreciable non-linear or hysteresis behavior. If there is, consider recalibrating or troubleshooting the transducer.
11. Update DCDT calibration numbers in the calibration file, logsheets, and your notes.

F.3 Typical measured response

As an example of a typical load cell response, a calibration of a TransTek DCDT shows a very linear trend with no hysteresis (Fig.F.1).

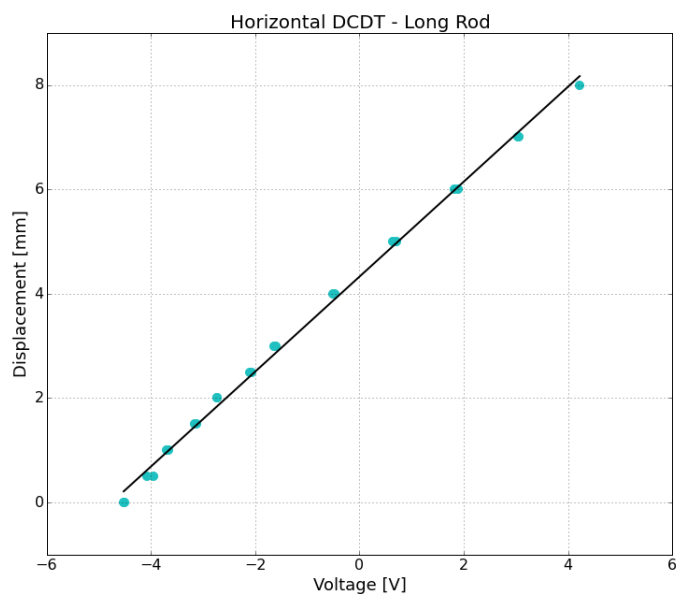


Fig. F.1. An example calibration obtained from a DCDT.

Appendix G

Look File Format Description and Biaxtools

G.1 Purpose

This script was designed to read data into an easy to use format from xlook output in ASCII or binary form. Data is read, the header parsed for column names, lengths, etc., and a rec array or Pandas dataframe object returned that is easy to access and call from within a script. Column names are used to call the data columns, so as long as consistent naming is used the column order in the file is irrelevant.

G.2 Description

G.2.1 ASCII Files

The function ReadAscii first opens the text file with a standard open command. We know that each column in the data is written as 12 characters wide. The first line of the header is the number of records, the second is the column number, the third the column headings, the fourth the column units, and the fifth the number of records in each column. This information if parsed and stored. Numerical data is read into an array. A rec array is created with the numpy package and the labels of the column names that were parsed or the data is converted into a dataframe object.

G.2.2 Binary Files

The function ReadBin opens the binary file in 'read binary' mode. The initial file information is stored as follows (in big-endian format):

Information	Format	Bytes
Name	20 characters	20
Number of Columns	int	4
Sweep	int	4
Date/Time	int	4

For each possible column there are 84 bytes of information. There are 32 possible columns. We read the information for each column and store information for columns that have data. Blank columns are identified by the first 6 characters of the name 'no_val'.

Information	Format	Bytes
Name	13 characters	13
Units	13 characters	13
Gain	int	4
Comment	50 characters	50
Number of Elements	int	4

Data is stored as the default machine format, which for modern Intel based computers in little-endian. This is the default for the module, but big-endian can be specified. Each column is written out as a sequence of doubles that are n_{elem} long. Doubles are read and stored in a numpy array. The array is then combined with datatype information collected from the headers and stored as a rec array.

To find the default machine binary format run: `python -c "import struct; print 'little' if ord(struct.pack('L', 1)[0]) else 'big'"`

G.3 Cautions

A few cautions should be observed when using the baxread script:

1. The empty array is shaped by row number information from the header. If a datafile is cut, but the header is left unmodified there will be many extra zero data pairs at the end of the array.

G.4 Usage

G.4.1 Return Formats

By default data will be returned as a Numpy record array (recarray). Data can also be returned as a Pandas dataframe object that is indexed on the row number of the data. To do this, set `pandas=True` in the function call to either ReadAscii or ReadBin.

G.4.2 ASCII Files

First process the experimental data in xlook and output a text file with headers. To do this input `type 0 -1 1 12 pxxxx-data.txt` at the xlook command line or add it to the data reduction file. Be sure to correct any column or row number specifications here. Start IPython or open your own Python script. Import baxread and pass the function ReadAscii the name of the text output file from xlook. The array is now returned and ready to use.

G.4.3 Binary Files

Process the experimental data in xlook and output a binary file. This is done with the ‘write’ command with the syntax *write filename*. In IPython or your Python script import baxread and pass the function ReadBin the name of the binary file. The array is returned and ready to use.

Files that were written in a big-endian format by setting dataendianess to ‘big’. The function call would look like *ReadBin(filename,dataendianess='big')*.

G.5 Acknowledgements

Thank you to Marco Scuderi for using the code and being patient as little issues were worked out. Please send any bug reports to kd5wxb@gmail.com or as an issue in the github repository.

G.6 Code

```
import numpy as np

import struct

import pandas as pd


def ReadAscii(filename ,pandas=False):

    """
    Takes a filename containing the text output (with headers) from xlook and
    reads the columns into a rec array or dataframe object for easy data
    processing and access.

    """

try:
    f = open(filename , 'r')

except:
    print "Error Opening %s" %filename

    return 0

col_width = 12 # Columns are 12 char wide in header

# First line of the file is the number of records
```

```

num_recs = f.readline()

num_recs = int(num_recs.strip('number of records = '))

print "\nNumber of records: %d" %num_recs

# Second line is column numbers, we don't care so just count them

num_cols = f.readline()

num_cols = num_cols.split('col')

num_cols = len(num_cols)

print "Number of columns: %d" %num_cols

# Third line is the column headings

col_headings_str = f.readline()

col_headings_str = col_headings_str[5:-1]

col_headings = [ 'row_num' ] # Row number the the first (unlabeled) column

for i in xrange(len(col_headings_str)/12):

    heading = col_headings_str[12*i:12*i+12].strip()

    col_headings.append(heading)

# Fourth line is column units

col_units_str = f.readline()

col_units_str = col_units_str[5:-1]

col_units=[]

```

```

for i in xrange(len(col_units_str)/12):

    heading = col_units_str[12*i:12*i+12].strip()

    col_units.append(heading)

col_units = [x for x in col_units if x != '\n'] #Remove newlines


# Fifth line is number of records per column

col_recs = f.readline()

col_recs = col_recs.split('recs')

col_recs = [int(x) for x in col_recs if x != '\n']


# Show column units and headings

print "\n\n-----"
print "|%15s|%15s|%15s|" %( 'Name' , 'Unit' , 'Records' )
print "-----"

for column in zip(col_headings, col_units, col_recs):

    print "|%15s|%15s|%15s|" %(column[0], column[1], column[2])

    print "-----"


# Read the data into a numpy recarray

dtype=[]

#dtype.append(( 'row_num' , 'float' ))
for name in col_headings:

```

```
        dtype.append((name, 'float'))  
        dtype = np.dtype(dtype)  
  
data = np.zeros([num_recs, num_cols])  
  
i=0  
  
for row in f:  
    row_data = row.split()  
    for j in xrange(num_cols):  
        data[i,j] = row_data[j]  
    i+=1  
  
f.close()  
  
if pandas==True:  
    # If a pandas object is requested, make a data frame  
    # indexed on row number and return it  
    dfo = pd.DataFrame(data, columns=col_headings)  
    dfo = dfo.set_index('row_num')  
    return dfo  
  
else:
```

```
# Otherwise return the default (Numpy Recarray)

data_rec = np.rec.array(data, dtype=dtype)

return data_rec

def ReadBin(filename, dataendianess='little', pandas=False):

    """
    Takes a filename containing the binary output from xlook and
    reads the columns into a rec array or dataframe object for easy
    data processing and access.

    The data section of the file is written in the native format of the machine
    used to produce the file. Endianess of data is little by default, but may
    be changed to 'big' to accomodate older files or files written on power p
    chips.

    try:
        f = open(filename, 'rb')
    except:
        print "Error Opening %s" %filename
    return 0
```

```
col_headings = []

col_recs      = []

col_units     = []

# Unpack information at the top of the file about the experiment

name = struct.unpack('20c', f.read(20))

name = ''.join(str(i) for i in name)

name = name.split("\0")[0]

print "\nName: ", name

# The rest of the header information is written in big endian format

# Number of records (int)

num_recs = struct.unpack('>i', f.read(4))

num_recs = int(num_recs[0])

print "Number of records: %d" %num_recs

# Number of columns (int)

num_cols = struct.unpack('>i', f.read(4))

num_cols = int(num_cols[0])

print "Number of columns: %d" %num_cols
```

```

# Sweep (int) - No longer used

swp = struct.unpack('>i', f.read(4))[0]
print "Swp: ", swp


# Date/time(int) - No longer used

dtime = struct.unpack('>i', f.read(4))[0]
print "dtime: ", dtime


# For each possible column (32 maximum columns) unpack its header
# information and store it. Only store column headers of columns
# that contain data. Use termination at first NUL.

for i in range(32):

    # Channel name (13 characters)

    chname = struct.unpack('13c', f.read(13))
    chname = ''.join(str(i) for i in chname)
    chname = chname.split("\0")[0]

    # Channel units (13 characters)

    chunits = struct.unpack('13c', f.read(13))
    chunits = ''.join(str(i) for i in chunits)
    chunits = chunits.split("\0")[0]

```

```
# This field is now unused, so we just read past it (int)
gain = struct.unpack('>i', f.read(4))

# This field is now unused, so we just read past it (50 characters)
comment = struct.unpack('50c', f.read(50))

# Number of elements (int)
nelem = struct.unpack('>i', f.read(4))
nelem = int(nelem[0])

if chname[0:6] == 'no_val':
    continue # Skip Blank Channels
else:
    col_headings.append(chname)
    col_recs.append(nelem)
    col_units.append(chunits)

# Show column units and headings
print "\n\n-----"
print "|%15s|%15s|%15s|" %('Name', 'Unit', 'Records')
```

```
print "-----"  
  
for column in zip(col_headings,col_units,col_recs):  
  
    print "|%15s|%15s|%15s|" %(column[0],column[1],column[2])  
  
    print "-----"  
  
  
# Read the data into a numpy recarray  
  
dtype=[]  
  
for name in col_headings:  
  
    dtype.append((name,'double'))  
  
dtype = np.dtype(dtype)  
  
  
data = np.zeros([num_recs,num_cols])  
  
  
for col in range(num_cols):  
  
    for row in range(col_recs[col]):  
  
        if dataendianess == 'little':  
  
            data[row,col] = struct.unpack('<d',f.read(8))[0]  
  
        elif dataendianess == 'big':  
  
            data[row,col] = struct.unpack('>d',f.read(8))[0]  
  
        else:  
  
            print "Data endian setting invalid, please check and retry"  
  
            return 0
```

```
data_rec = np.rec.array(data,dtype=dtype)

f.close()

if pandas==True:

    # If a pandas object is requested, make a data frame

    # indexed on row number and return it

    dfo = pd.DataFrame(data,columns=col_headings)

    # Binary didn't give us a row number, so we just let

    # pandas do that and name the index column

    dfo.index.name = 'row_num'

    return dfo


else:

    # Otherwise return the default (Numpy Recarray)

    data_rec = np.rec.array(data,dtype=dtype)

    return data_rec
```

Bibliography

- Aharonov, E. and Sparks, D. (1999). Rigidity phase transition in granular packings. *Physical Review E*, 60(6):6890.
- Albert, I., Sample, J., Morss, A., Rajagopalan, S., Barabási, A.-L., and Schiffer, P. (2001). Granular drag on a discrete object: Shape effects on jamming. *Physical Review E*, 64(6):061303.
- Anthony, J. L. and Marone, C. (2005). Influence of particle characteristics on granular friction. *Journal of Geophysical Research*, 110(B8):B08409.
- Balk, M., Bose, M., Ertem, G., Rogoff, D. A., Rothschild, L. J., and Freund, F. T. (2009). Oxidation of water to hydrogen peroxide at the rock–water interface due to stress-activated electric currents in rocks. *Earth and Planetary Science Letters*, 283(1):87–92.
- Baumberger, T. and Berthoud, P. (1999). Physical analysis of the state- and rate-dependent friction law. II. Dynamic friction. *Phys. Rev. B*, 60(6):3928–3939.
- Bayart, E., Rubin, A., and Marone, C. (2006). Evolution of fault friction following large velocity jumps. In *AGU Fall Meeting Abstracts*, volume 1, page 0180.
- Beeler, N., Tullis, T., and Weeks, J. (1994). The roles of time and displacement in the evolution effect in rock friction. *Geophysical Research Letters*, 21(18):1987–1990.

- Beeler, N. M., Hickman, S. H., and Wong, T.-f. (2001). Earthquake stress drop and laboratory-inferred interseismic strength recovery. *Journal of Geophysical Research: Solid Earth (1978–2012)*, 106(B12):30701–30713.
- Beroza, G. C. and Ide, S. (2011). Slow Earthquakes and Nonvolcanic Tremor. *Annual Review of Earth and Planetary Sciences*, 39(1):271–296.
- Bianchi, R., Capaccioni, F., Cerroni, P., Coradini, M., Flamini, E., Hurren, P., Martelli, G., and Smith, P. N. (1984). Radiofrequency emissions observed during macroscopic hypervelocity impact experiments. *Nature*, 308(5962):830–832.
- Boettcher, M. S. (1999). Numerical simulations of granular shear zones using the distinct element method 1. Shear zone kinematics and the micromechanics of localization. *Journal of Geophysical Research*, 104(B2):2703–2719.
- Brace, W. F. and Byerlee, J. D. (1966). Stick-Slip as a Mechanism for Earthquakes. *Science*, 153(3739):990–992.
- Brace, W. F. and Byerlee, J. D. (1969). Mechanical instabilities observed in laboratory experiments on rocks. *Eos Trans. AGU*, 50(5):400.
- Buishand, T. A. (1982). Some methods for testing the homogeneity of rainfall records. *Journal of Hydrology*, 58(1):11–27.
- Camara, C. G., Escobar, J. V., Hird, J. R., and Putterman, S. J. (2008). Correlation between nanosecond X-ray flashes and stick-slip friction in peeling tape. *Nature*, 455(7216):1089–1092.

Cates, M., Wittmer, J., Bouchaud, J.-P., and Claudin, P. (1998). Jamming, force chains, and fragile matter. *Physical review letters*, 81(9):1841.

Cress, G. O., Brady, B. T., and Rowell, G. A. (1987). Sources of electromagnetic radiation from fracture of rock samples in the laboratory. *Geophysical Research Letters*, 14(4):331–334.

Derr, J. S. (1973). Earthquake lights: a review of observations and present theories. *Bulletin of the Seismological Society of America*, 63(6):2177–2187.

Dickinson, J. T. (1982). Fracto-emission accompanying adhesive failure. *Journal of Vacuum Science and Technology*, 20(3):436.

Dickinson, J. T. (1984). Fracto-emission: The role of charge separation. *Journal of Vacuum Science & Technology A: Vacuum, Surfaces, and Films*, 2(2):1112.

Dickinson, J. T., Jenson, L. C., and Park, M. K. (1982). Time-of-flight measurements of the mass-to-charge ratio of positive ion emission accompanying fracture. *Journal of Materials Science*, 17(11):3173–3178.

Dieterich, J. H. (1972). Time-dependent friction in rocks. *Journal of Geophysical Research*, 77(20):3690–3697.

Dieterich, J. H. (1978). Time-dependent friction and the mechanics of stick-slip. *Pure and applied geophysics*, 116(4-5):790–806.

Enomoto, Y. and Zheng, Z. (1998). Possible evidences of earthquake lightning accompanying the 1995 Kobe earthquake inferred from the Nojima fault gouge. *Geophysical Research Letters*, 25(14):2721–2724.

- Ferré, E. C., Zechmeister, M. S., Geissman, J. W., MathanaSekaran, N., and Kocak, K. (2005). The origin of high magnetic remanence in fault pseudotachylites: Theoretical considerations and implication for coseismic electrical currents. *Tectonophysics*, 402(1-4):125–139.
- Fidani, C. (2010). The earthquake lights (EQL) of the 6 April 2009 Aquila earthquake, in Central Italy. *Nat. Hazards Earth Syst. Sci.*, 10:967–978.
- Finkelstein, D., Hill, R. D., and Powell, J. R. (1973). The piezoelectric theory of earthquake lightning. *Journal of Geophysical Research*, 78(6):992–993.
- Freund, F. (2000). Time-resolved study of charge generation and propagation in igneous rocks. *Journal of Geophysical Research*, 105(B5):11001–11–019.
- Freund, F. (2010). Toward a unified solid state theory for pre-earthquake signals. *Acta Geophysica*, 58(5):719–766.
- Freund, F. T., Takeuchi, A., and Lau, B. W. S. (2006). Electric currents streaming out of stressed igneous rocks – A step towards understanding pre-earthquake low frequency EM emissions. *Physics and Chemistry of the Earth, Parts A/B/C*, 31(4-9):389–396.
- Frid, V., Bahat, D., Goldbaum, J., and Rabinovitch, A. (2000). Experimental and theoretical investigations of electromagnetic radiation induced by rock fracture. *Israel Journal of Earth Sciences*, 49:9–19.
- Frye, K. M. and Marone, C. (2002). Effect of humidity on granular friction at room temperature. *Journal of geophysical research*, 107(B11):2309.

Gu, J.-C., Rice, J. R., Ruina, A. L., and Tse, S. T. (1984). Slip motion and stability of a single degree of freedom elastic system with rate and state dependent friction. *Journal of the Mechanics and Physics of Solids*, 32(3):167–196.

Hanson, D. R. and Rowell, G. A. (1982). Electromagnetic radiation from rock failure. *Bureau of Mines Report of Investigations*.

Heslot, F., Baumberger, T., Perrin, B., Caroli, B., and Caroli, C. (1994). Creep, stick-slip, and dry-friction dynamics: Experiments and a heuristic model. *Physical Review E*, 49(6):4973.

Hong, T. and Marone, C. (2005). Effects of normal stress perturbations on the frictional properties of simulated faults. *Geochemistry Geophysics Geosystems*, 6(3).

Ide, S., Shelly, D. R., and Beroza, G. C. (2007). Mechanism of deep low frequency earthquakes: Further evidence that deep non-volcanic tremor is generated by shear slip on the plate interface. *Geophysical Research Letters*, 34(3):L03308.

Ikari, M. J., Marone, C., and Saffer, D. M. (2011). On the relation between fault strength and frictional stability. *Geology*, 39(1):83–86.

Ikari, M. J., Marone, C., Saffer, D. M., and Kopf, A. J. (2013). Slip weakening as a mechanism for slow earthquakes. *Nature Geoscience*, 6(6):468–472.

Jaeger, J. C. (1971). Friction of Rocks and Stability of Rock Slopes. *Géotechnique*, 21(2):97–134.

Johnson, P. A., Ferdowsi, B., Kaproth, B. M., Scuderi, M., Griffa, M., Carmeliet, J., Guyer, R. A., Le Bas, P.-Y., Trugman, D. T., and Marone, C. (2013). Acoustic

emission and microslip precursors to stick-slip failure in sheared granular material.

Geophys. Res. Lett., 40(21):5627–5631.

Jouniaux, L. and Ishido, T. (2013). Electrokinetics in Earth Sciences. *International Journal of Geophysics*, 2013:1–1.

Kaproth, B. M. and Marone, C. (2013). Slow Earthquakes, Preseismic Velocity Changes, and the Origin of Slow Frictional Stick-Slip. *Science*, 341(6151):1229–1232.

Karner, S. L. and Marone, C. (2000). Effects of loading rate and normal stress on stress drop and stick-slip recurrence interval. *Geophysical Monograph Series*, 120:187–198.

Karner, S. L., Marone, C., and Evans, B. (1997). Laboratory study of fault healing and lithification in simulated fault gouge under hydrothermal conditions. *Tectonophysics*, 277(1):41–55.

Kirschvink, J. L. (2000). Earthquake prediction by animals: evolution and sensory perception. *Bulletin of the Seismological Society of America*, 90(2):312–323.

Knuth, M. and Marone, C. (2007). Friction of sheared granular layers: Role of particle dimensionality, surface roughness, and material properties. *Geochemistry Geophysics Geosystems*, 8(3).

Leeman, J. R., Scuderi, M. M., Marone, C., Saffer, D. M., and Shinbrot, T. (2014). On the origin and evolution of electrical signals during frictional stick slip in sheared granular material. *Journal of Geophysical Research: Solid Earth*, page n/a–n/a.

Liu, A. J. and Nagel, S. R. (1998). Nonlinear dynamics: Jamming is not just cool anymore. *Nature*, 396(6706):21–22.

- Liu, C. h., Nagel, S. R., Schecter, D. A., Coppersmith, S. N., Majumdar, S., Narayan, O., and Witten, T. A. (1995). A Model for Force Fluctuations in Bead Packs. *Science*, 269:513–515.
- Lockner, D. A., Johnston, M., and Byerlee, J. D. (1983). A mechanism to explain the generation of earthquake lights. *Nature*, 302:28–33.
- Logan, J., Dengoz, C., Higgs, N., and Wang, Z. (1992). Fabrics of Experimental Fault Zones: Their Development and Relationship to Mechanical Behavior. *Fault Mechanics and Transport Properties of Rocks*, 51:33.
- Mair, K. and Abe, S. (2011). Breaking Up: Comminution Mechanisms in Sheared Simulated Fault Gouge. *Pure and Applied Geophysics*, 168(12):2277–2288.
- Mair, K., Frye, K. M., and Marone, C. (2002). Influence of grain characteristics on the friction of granular shear zones. *Journal of Geophysical Research: Solid Earth (1978–2012)*, 107(B10):ECV 4–1–ECV 4–9.
- Majmudar, T. S. and Behringer, R. P. (2005). Contact force measurements and stress-induced anisotropy in granular materials. *Nature*, 435(1079):1079–1082.
- Marone, C. (1998). LABORATORY-DERIVED FRICTION LAWS AND THEIR APPLICATION TO SEISMIC FAULTING. *Annual Review of Earth and Planetary Sciences*, 26(1):643–696.
- Marone, C. and Kilgore, B. (1993). Scaling of the critical slip distance for seismic faulting with shear strain in fault zones. *Nature*, 362(6421):618–621.

Marone, C. and Saffer, D. (In Press). The mechanics of frictional healing and slip instability during the seismic cycle. *Treatise on Geophysics 2nd Ed.*

Martelli, G. and Cerroni, P. (1985). On the theory of radio frequency emission from macroscopic hypervelocity impacts and rock fracturing. *Physics of the Earth and Planetary Interiors*, 40(4):316–319.

Mizutani, H., Ishido, T., Yokokura, T., and Ohnishi, S. (1976). Electrokinetic phenomena associated with earthquakes. *Geophysical Research Letters*, 3(7):365–368.

Nitsan, U. (1977). Electromagnetic emission accompanying fracture of quartzbearing rocks. *Geophysical Research Letters*, 4(8):333–336.

Obara, K. (2002). Nonvolcanic Deep Tremor Associated with Subduction in Southwest Japan. *Science*, 296(5573):1679–1681.

Onuma, K., Muto, J., Nagahama, H., and Otsuki, K. (2011). Electric potential changes associated with nucleation of stick-slip of simulated gouges. *Tectonophysics*, 502(3–4):308–314.

Page, E. (1954). Continuous inspection schemes. *Biometrika*, 41(1/2):100–115.

Pähzt, T., Herrmann, H. J., and Shinbrot, T. (2010). Why do particle clouds generate electric charges? *Nature Physics*, 6(5):364–368.

Park, S. K., Johnston, M. J. S., Madden, T. R., and Dale Morgan, F. (1993). Electromagnetic precursors to earthquakes in the ULF band: A review of observations and mechanisms. *Reviews of Geophysics*, 31(2):117–132.

- Peng, Z. and Gomberg, J. (2010). An integrated perspective of the continuum between earthquakes and slow-slip phenomena. *Nature Geoscience*, 3(9):599–607.
- Pingali, K. C., Shinbrot, T., Hammond, S. V., and Muzzio, F. J. (2009). An observed correlation between flow and electrical properties of pharmaceutical blends. *Powder Technology*, 192(2):157–165.
- Raimondo, M. and Tajvidi, N. (2004). A peaks over threshold model for change-point detection by wavelets. *Statistica Sinica*, 14(2):395–412.
- Rathbun, A. P., Marone, C., Alley, R. B., and Anandakrishnan, S. (2008). Laboratory study of the frictional rheology of sheared till. *Journal of Geophysical Research*, 113(F2):F02020.
- Rice, J. R. (1983). Constitutive relations for fault slip and earthquake instabilities. *Pure and applied geophysics*, 121(3):443–475.
- Rice, J. R. and Gu, J.-c. (1983). Earthquake aftereffects and triggered seismic phenomena. *PAGEOPH*, 121(2):187–219.
- Richardson, E. and Marone, C. (1999). Effects of normal stress vibrations on frictional healing. *Journal of Geophysical Research*, 104(B12):28859.
- Rowell, G. A., Brady, B. T., Yoder, L. P., and Hanson, D. R. (1981). Precursors of laboratory rock failure. *Fracture Mechanics for Ceramics, Rocks, and Concrete*, edited by: Freiman, S.W. and Fuller, E.R., pages 196–220.
- Sammis, C., King, G., and Biegel, R. (1987). The kinematics of gouge deformation. *Pure and Applied Geophysics*, 125(5):777–812.

Savitzky, A. and Golay, M. J. E. (1964). Smoothing and differentiation of data by simplified least squares procedures. *Analytical Chemistry*, 36(8):1627–1639.

Scholz, C. H. (2002). *The mechanics of earthquakes and faulting*. Cambridge university press.

Scott, D. R., Marone, C. J., and Sammis, C. G. (1994). The apparent friction of granular fault gouge in sheared layers. *Journal of Geophysical Research: Solid Earth (1978–2012)*, 99(B4):7231–7246.

Scuderi, M., Carpenter, B., and C., M. (2013). Physicochemical processes of frictional healing: effects of water on stick-slip stress drop and friction of granular fault gouge. *Journal of Geophysical Research*.

Shinbrot, T., Kim, N. H., and Thyagu, N. N. (2012). Electrostatic precursors to granular slip events. *Proceedings of the National Academy of Sciences*, 109(27):10806–10810.

St-Laurent, F., Derr, J. S., and Freund, F. T. (2006). Earthquake lights and the stress-activation of positive hole charge carriers in rocks. *Physics and Chemistry of the Earth, Parts A/B/C*, 31(4-9):305–312.

Takeuchi, A., Futada, Y., Okubo, K., and Takeuchi, N. (2010). Positive electrification on the floor of an underground mine gallery at the arrival of seismic waves and similar electrification on the surface of partially stressed rocks in laboratory. *Terra Nova*, 22(3):203–207.

Takeuchi, A. and Nagao, T. (2013). Activation of hole charge carriers and generation of electromotive force in gabbro blocks subjected to nonuniform loading. *Journal of Geophysical Research: Solid Earth*, 118(3):915–925.

Triantis, D., Anastasiadis, C., and Stavrakas, I. (2008). The correlation of electrical charge with strain on stressed rock samples. *Nat. Hazards Earth Syst. Sci.*, 8:1243–1248.

Uyeda, S., Nagao, T., and Kamogawa, M. (2009). Short-term earthquake prediction: Current status of seismo-electromagnetics. *Tectonophysics*, 470(3):205–213.

Yasuhara, H. (2005). Fault zone restrengthening and frictional healing: The role of pressure solution. *Journal of Geophysical Research*, 110(B6):B06310.

DRAFT: OCTOBER 21, 2016 AT 3:49 PM

Vita

John R. Leeman

Education

<i>The Pennsylvania State University</i>	State College, Pennsylvania	2012-2017
Ph.D in Geosciences, May 2017		
Advisors: Dr. Chris Marone and Dr. Demian Saffer		
<i>University of Oklahoma</i>	Norman, Oklahoma	2007-2012

B.S. in Meteorology, B.S. in Geophysics, minor in Mathematics

Core Competencies

Experimental Design	Biaxial & Triaxial Deformation experiments	Python Programming
Electronics Design	3D CAD Design	3D Printing
Public Speaking	Microcontroller Programming	Data Processing
Scientific Visualization	System Administration	Mathematical Modeling

Selected Grants & Awards

Peter Deines Lectureship	2016
AGU Outstanding Student Paper	2011, 2015
National Science Foundation Graduate Fellow	2013–2017
Shell Geosciences Energy Research Facilities Award	2013–2016
Hess Corporation Exploration & Production Technology Scholarship	2014, 2015

Selected Publications

- JR Leeman, RD Valdez, RB Alley, S Anandakrishnan, and DM Saffer. Mechanical and hydrologic properties of whillans ice stream till: Implications for basal strength and stick-slip failure. *Journal of Geophysical Research: Earth Surface*, 121(7):1295–1309, 2016.
- JR Leeman, DM Saffer, MM Scuderi, and C Marone. Laboratory observations of slow earthquakes and the spectrum of tectonic fault slip modes. *Nature Communications*, 7, 2016.
- John Leeman, Marco Maria Scuderi, Chris Marone, and Demian Saffer. Stiffness evolution of granular layers and the origin of repetitive, slow, stick-slip frictional sliding. *Granular Matter*, pages 1–11, May 2015.
- J. R. Leeman, M. M. Scuderi, C. Marone, D. M. Saffer, and T. Shinbrot. On the origin and evolution of electrical signals during frictional stick slip in sheared granular material. *J. Geophys. Res. Solid Earth*, 119(5):4253–4268, May 2014.

Professional & Service Activities

<i>Academic Integrity Committee</i>	The Pennsylvania State University	2014–2017
Graduate representative for academic integrity investigations and hearings.		
<i>Session Co-Chair</i>	American Geophysical Union	2014–2016
Co-chair a session on education and data visualization at the AGU Fall Meeting.		
<i>Instructor</i>	The Pennsylvania State University	2015–2016
Assist teaching seimology laboratory and develop and teach a 3 hour course on techniques in experimental geoscience.		